UNIVERSITY OF BIRMINGHAM

GNSS-BASED MULTISTATIC SAR

by

USSANAI NITHIROCHANANONT

A thesis submitted to the University of Birmingham for the degree of

DOCTOR OF PHILOSOPHY

Department of Electronic, Electrical and Systems Engineering
School of Engineering
College of Engineering and Physical Sciences
University of Birmingham
September 2019

Abstract

Synthetic aperture radar (SAR) is an efficient tool in remote sensing for imaging the Earth's surface to detect, monitor, and assess its changes. Despite SAR is widely used worldwide, its operation mainly uses monostatic and bistatic configuration. In contrast, multistatic configuration is confined to simulation level, at least in open literature. This thesis experimentally explored the potential of passive multistatic SAR imaging using Global Navigation Satellite Systems (GNSS) as transmitters of opportunity and a single stationary receiver on the ground, and established a practical framework for GNSS-based multistatic SAR.

During the experiment, a passive SAR system recorded satellite signal reflections off a target area from four GNSS satellites and processed these signals into bistatic images. Those images were combined using both coherent and non-coherent combination techniques to form multistatic imagery. The obtained results showed that the non-coherent multistatic method enhanced information space and revealed object geometric features such as edges, shapes, and dimensions. In addition, variations of bistatic scattering obtained from individual images can be used to coarsely classify different object types. The results also confirmed that a coherent combination of SAR images with such a system was possible and improved spatial resolution as well as power budget.

Acknowledgements

Work in this thesis could not be achieved without the assistance of the others. Firstly, I would like to thank my supervisors, Dr Michail Antoniou and Professor Mikhail Cherniakov for their help, advice, and guidance over the past four years. I have learned and developed research skills from their experience.

For the financial support, I would like to thank the Royal Thai Government for fully funding my PhD research, as well as the Geo-informatics and Space Development Agency (Public Organisation) for supporting my career development by allowing study leave to pursue a PhD degree.

I would also like to thank all the members of Microwave Integrated System Laboratory for their assistance with the experimental campaign, and discussion on the work as well as making joyful environment on and off the office, in particular Dr Hui Ma and Dr Dimitrios Tzagkas.

Finally, and most especially, I would like to thank my family for their enduring support and encouragement, without which I would not have completed this work.

Table of Contents

List of Figures

List of Tables

List of Abbreviations and Acronyms

AF	Ambiguity Function
BPA	Backprojection Algorithm
BPSF	Bistatic Point-Spread Functions
BW	Bandwidth
COTS	Commercial Off-The-Shelf
dBsm	Decibel Square Metre
EIRP	Equivalent Isotropically Radiated Power
FFT	Fast Fourier Transform
GAF	Generalised Ambiguity Function
GNSS	Global Navigation Satellites System
HC	Heterodyne Channel
IFFT	Inverse Fast Fourier Transform
LEO	Low Earth Orbit
LFM	Linear Frequency Modulation
MF	Matched Filter
MPSF	Multistatic Point-Spread Functions
POSP	Principle of Stationary Phase
PRF	Pulse Repetition Frequency
PSF	Point Spread Function
RADAR	Radio Detection And Ranging
RC	Range Compression
RC	Radar Channel
RCS	Radar Cross Section

RX	Receiver
SAR	Synthetic Aperture Radar
SNR	Signal-to-Noise Ratio
TBP	Time Bandwidth Product
TX	Transmitter

List of Principals Symbols

Nomenclature for all equations is defined in the main body of the thesis, however a list of the more commonly used symbols is given here.

P_t	Received Power
P_r	Tranmitted Power
G_t	Gain of Transmitting Antenna
G_r	Gain of The Receiving Antenna
R_t	Transmitter to The Target Range
R_r	Receiver to The Target Range
λ	Wavelength
σ	Radar Cross Section
σ^0	Normalised RCS
E_x	Total Power of Signal
χ	Ambiguity Function
c	Speed of Light
f_d	Doppler Frequency
δ_r	Range Resolution
δ_a	Azimuth Resolution
δ_{rg}	Ground Range Resolution
δ_{ag}	Ground Azimuth Resolution

Chapter 1

Introduction

1.1 Motivation and Problem Statement

The Earth's surface is dynamic and always changing through both natural and human activities. For example, environmental changes on the land and ocean, natural disasters, e.g. flood or landslide, or human-made deforestation. For the past few decades, satellite remote sensing has become a powerful tool to monitor, understand, predict, and manage those changes at a global scale. Synthetic aperture radar (SAR) is one of the promising instruments for remote sensing. It is a radar imaging technique that uses the microwave frequency band and can operate in a wide range of weather conditions independently of light sources [1].

Since the launch of SEASAT [2, 3], the first SAR satellite, in 1978, many SAR instruments have been developed and efficiently operated onboard earth observation satellites in various missions to monitor the Earth's surface. For example, the C-band SAR instrument on the first European Remote Sensing (ERS-1) satellites (1991-2000) for sea-state forecasting and monitoring sea ice distribution [4], the C-band SAR phased array antenna on Canada's RADARSAT-2 satellite (since 2007) for resource management and environmental monitoring [5], and the S-band active phased array antenna on UK's NovaSAR satellite (since 2018) for wide applications including flood monitoring, agricultural crop assessment and disaster monitoring [6].

For the passive spaceborne SAR, TanDEM-X, [7], is a first SAR satellite to operate in bistatic mode with TerraSAR-X. It provides a global and unprecedentedly accurate digital elevation model of the Earth surface. MirrorSAR, [8], comprises a set of spatially separated transmit and receive satellites. They are designed to operate in bistatic and multistatic mode as well as high-resolution wide-swath SAR imaging. PASSAT, [9, 10], is a passive imaging radar constellation for persistent monitoring of large areas. The constellation employs microsatellites to operate at 400 km low Earth orbit (LEO).

Despite providing high resolution and covering large areas from an order of several square kilometres in Spotlight mode to hundreds of kilometres in ScanSAR mode, restriction of orbits takes days for a satellite to revisit the same area with the same sensor's incident angle. Looking at the same area with different angles is possible to reduce the need for revisiting, but this depends on the location. Practically, changing looking direction has to be considered to avoid conflict with the subsequent imaging plane.

A passive SAR system using transmitters of opportunity has emerged in the past decade. The passive system can be developed with a low budget since it comprises commercial-off-the-shelf components, e.g. a generic Global Navigation Satellite System (GNSS) receiver and a multi-purposes antenna. Also, it has no transmitting component; thus, no authorisation or licence is required to operate the system. Among a variety of illuminating sources, a system using a single satellite from the GNSS constellations has been demonstrated theoretically and experimentally [11-19]. This system, the GNSS-based passive SAR, has been pioneered at the Microwave Integrated Systems Laboratory (MISL) at the University of Birmingham, which is still world-leading in this area. In this system, at least 6-8 satellites from a single GNSS constellation are available at any time and any point on the Earth's surface. This

system can frequently provide SAR images to monitor an area at a local scale [20] and also be used for coherent change detection [21]. These capabilities with a multitude of GNSS satellites enable the potential of the system to complement active systems for persistence monitoring the Earth's surface.

However, using non-dedicated signals for SAR, which are low bandwidth and low flux density near the Earth's surface, produces coarse spatial resolution images with elliptically shaped responses defined by the ambiguity function. This resolution could be further degraded as the bistatic angle increases since bistatic is the basic configuration of the passive system. Moreover, a single aspect angle limits the capability to reveal more diverse information of the observed area. Many efforts have been made to improve the spatial resolution under bistatic topology, including using the adjacent frequency band combination technique [22, 23].

Alternatively, multistatic techniques are fascinating to challenge those limitations because, fundamentally, multistatic systems can improve target localisation due to the diversity of viewing angles. Observing the target area from multiple angles could enhance the information space of an area of interest in a multistatic image compared to a single bistatic image. Moreover, since the bandwidth and aperture length for a single satellite have limits, coherent multistatic SAR method can be used to improve spatial resolution. These multistatic techniques can be applied to the GNSS-based SAR seamlessly since the GNSS constellations are inherent multistatic systems. Since a multistatic configuration is based on the same system as its bistatic counterpart, their performances can also be directly compared. Improved spatial resolution and enhanced information space could lead passive SAR systems to new applications, e.g. automatic terrain classification. However, improvement

using multistatic techniques is not only beneficial for the passive GNSS-based SAR system but also applicable to multistatic SAR systems in general, regardless of active or passive operation. The experimental results from extended target areas and point-like targets in this thesis can be used to assess the potential of these techniques in real conditions.

1.2 Research Question and Hypotheses

The research question of this thesis was what are the benefits of GNSS-based multistatic SAR over its bistatic counterpart. The hypotheses for the question were that using multiple transmitters with spatial diversity of their positions can improve spatial resolution and enhance information space contained within SAR imagery.

1.3 Objectives

1. To experimentally explore the potential of non-coherent and coherent multistatic GNSS-based SAR compared to their bistatic SAR counterpart.
2. To establish a practical framework for non-coherent and coherent GNSS-based multistatic SAR image formation.

1.4 Methodology

The GNSS-based SAR was used as an experimental system to obtain the bistatic SAR imagery. These bistatic images were then combined using non-coherent and coherent combination techniques to form the experimental multistatic SAR imagery. The comparison was made between the multistatic and bistatic imageries, qualitatively and quantitatively, in terms of information contained within the images in the case of non-coherent combination and in terms of spatial resolution in the case of coherent combination.

1.5 Contributions

To the best of the author's knowledge, this thesis was the first experimentally verified research on GNSS-based multistatic SAR. The contributions of this thesis were following.

1. Experimentally explored the potential of non-coherent and coherent GNSS-based multistatic SAR over its bistatic SAR counterpart.
2. Established a practical framework for non-coherent and coherent GNSS-based multistatic SAR image formation.

1.6 Structure

This thesis has seven chapters which are as following:

Chapter 1 gives a brief overview of the thesis, including motivation, methodology, and outcomes.

Chapter 2 provides a fundamental theory of the imaging method used in the thesis. It covers the fundamentals of radar and synthetic aperture radar (SAR). For SAR, all imaging geometries, monostatic, bistatic, and multistatic, were described.

Chapter 3 describes the GNSS-based SAR theory. It covers all aspects of the theory, including GNSS signals and structures, power budget, spatial resolution and processing algorithms. This theory is essential since the experimental system was developed based on this theory.

Chapter 4 describes the methodology used in the experimental campaign. The methodology covers components in the experimental system, choosing candidate signals for both non-

coherent and coherent SAR experiments, collecting and pre-processing data, and designing the experiments.

Chapter 5 presents experimental non-coherent multistatic SAR results, which have been published in [24, 25] by the author of this thesis. The forty-six experimental bistatic images were coherently combined to form the multistatic images. The bistatic and multistatic imagery were compared in terms of information contained with the images. Two approaches were used to derive information, one was extracting information from the individual bistatic images and then combining it into the multistatic image, and another one was to form the multistatic image and then extract the information from it.

Chapter 6 presents experimental coherent multistatic SAR results, which have been published in [26, 27] by the author of this thesis. K-space was used to choose appropriate signals for coherent combination. The bistatic point-spread function (PSF) and SAR images of the candidate signals were coherently combined to form their corresponding multistatic counterparts. The theoretical PSF of the multistatic PSF was also obtained and compared to the experimental PSF. Power budget was discussed, and spatial resolution derived from k-space support was also initially analysed.

Chapter 7 concludes the thesis and suggests future work directions.

1.7 List of Publications

Publications arising from this thesis are the following.

1) U. Nithirochananont, M. Antoniou, and M. Cherniakov, "Passive GNSS-based multistatic SAR: first experimental results," in *2018 19th International Radar Symposium (IRS)*, 2018, pp. 1-9.
2) U. Nithirochananont, M. Antoniou, and M. Cherniakov, "Passive multi-static SAR – experimental results," *IET Radar, Sonar & Navigation*, vol. 13, no. 2, pp. 222-228, 2019.
3) U. Nithirochananont, M. Antoniou, and M. Cherniakov, "Passive coherent multistatic SAR: experimental results with a point-like target," in *2019 20th International Radar Symposium (IRS)*, 2019, pp. 1-6.
4) U. Nithirochananont, M. Antoniou, and M. Cherniakov, "Passive coherent multistatic SAR using spaceborne illuminators," *IET Radar, Sonar & Navigation*, vol. 14, no. 4, pp. 628-636, 2020.

1.8 Major Publication Review on Multistatic SAR

Multistatic SAR has received attention in recent decades. Many efforts were contributed to image formation algorithms [28-32]. Most of these works using a statistical approach to model a multistatic system. For a physical model approach, the concept of spaceborne multistatic SAR using multiple phase centres, to achieve high resolution and wide swath area, has been simulated and experimentally demonstrated in [33]. Furthermore, a new spaceborne multistatic SAR imaging configuration was proposed by [8]. In this configuration, multiple receive-only satellites are used to record a reflected signal that transmitted from dedicated satellite illuminators.

From the system point of view, a multistatic generalised ambiguity function (GAF) based on a bistatic GAF, which was presented in [15, 34], was considered. There are two approaches to find a solution of this multistatic GAF, either numerically [35] or analytically [36], for evaluating its spatial resolution. Both approaches express the multistatic GAF as a summation of the individual bistatic GAFs. There are two approaches to determine this combination. One is a coherent combination, and another one is a non-coherent combination.

The non-coherent multistatic SAR was theoretically and experimentally demonstrated using two satellites with a point-like target [36]. The results showed substantial spatial resolution improvement of this technique over bistatic. Further demonstration using a real target area was also presented in [37]. It showed that more objects could be identified in the experimental multistatic images, but artefacts arose from using non-coherent techniques. This work also applied a complex signal processing technique called CLEAN, to the experimental multistatic images to extract scattering centres of the objects on the target area, as well as to suppress the artefacts. CLEAN, [38], iteratively find the highest value in the image and subtract it with the dirty until the highest value is smaller than some threshold.

The extracted scattering centres can reveal edge and shape of the objects by merging location of those scattering centres identified in multiple perspective images. In [39], a feature-based non-coherent technique was proposed using a single GNSS constellation (BeiDou) with similar satellites' azimuth span. It obtained bistatic imagery with temporal separations of up to a month. The results showed that edge and shape could also be revealed. Alternatively, from multi-perspective analysis, in [40] showed that when observed the same objects at different viewing angles, different bistatic scattering effect can be noticed.

For coherent multistatic SAR, many works have been contributed on simulation level and – experiment with controlled-condition. All works showed similarly promising results with substantial spatial resolution improvement. In [41], the phase calibration technique for monostatic and bistatic images was proposed so that coherent multistatic images can be successfully formed. This calibration technique was used in the laboratory-conditioned experiment, [42]. In [43], simulations and experiments under laboratory conditions, with a point-like target, have been presented. In [44-49], simulations with various combination of transmitters and receivers were presented. In [49], k-space support (Chapter 6) which is a technique to represent the signal in the spatial-frequency domain was used to choose appropriate signals.

According to reviewing the literature on multistatic SAR, the aspects of conceptual development, simulating to prove the concept, and experiment to verify the results of the simulation, are well established. However, the experiment to explore the benefits of multistatic SAR with a simple technique such as non-coherent combination has not been performed. It may be useful to complement the active SAR system in terms of frequent local monitoring. Therefore, this thesis was designed to explore this particular benefit. Also, currently, the concept of multistatic coherent combination is limited to only the laboratory setting, leading to another experimental study in this thesis.

Chapter 2

Radar and SAR

2.1 Introduction

Radar is a system that detects reflected electromagnetic energy from a target and derives useful information about that target from the radar return. Generally, the detection performance of the radar can be determined using the radar range equation (also referred to as radar equation). In this chapter, this equation is derived based on a basic level of a radar system comprising a transmitter, a receiver, and a target to show the relationship between the power of the signal during transmission, propagation, and reflection. Performance of a radar system at later stages can also be determined by introducing additional suitable parameters to the equation.

Useful information about the target can be derived from radar return, e.g. range, trajectory or shape. As a result, radar can be used in many applications. For imaging purposes, one of the radar systems in this class is synthetic aperture radar (SAR). SAR is used to image the Earth's surface. One merit of its performance is expressed in terms of spatial resolution. Spatial resolution performance for each topology is shown to describe the performance of those SAR configurations.

In this chapter, fundamentals of radar and SAR are explained since they are essential for the understanding operation and analysing performance (e.g. power budget and spatial resolution) of GNSS-based SAR system which is later described in Chapter 3.

2.2 Radar

Radar was originally an abbreviation of Radio Detection and Ranging, but nowadays, it has become a common term ("radar") and been familiar to a wide audience rather than the acronym ("RADAR"). Radar is a system that used for detecting objects (targets) and extracting information about detected targets, e.g. range, angle or trajectory, [50]. The useful information extracted from the target could be, e.g. range or angle, in case of fixed target or trajectory, in case of moving target. Range is a distance between the target and the radar system. Angle is an angular position of the target used for determining angle of arrival of the target. Trajectory of the target can be derived to predict its future location. Radar with sufficiently high resolution in one or two coordinates can further reveal more information about the target, e.g. shape or size of the target.

Topology of the radar system (Figure 2.1) can be categorised, based on location as well as a number of transmitters and receivers, into three groups: monostatic, bistatic, and multistatic configurations. In monostatic configuration (Figure 2.1 (a)), a single transmitter and a single receiver are used and placed at the same location. In the case of bistatic configuration (Figure 2.1 (b)) a transmitter and a receiver are spatially separate by the bistatic angle (β). For multistatic configuration (Figure 2.1 (c)), two or more transmitters as well as two or more receivers are used. This configuration can be formed using multiple of either one topology or both monostatic and bistatic configurations. There is also a special case where a

transmitter and a receiver are separated by a small bistatic angle close to zero degrees. This configuration is referred to as quasi-monostatic configuration.

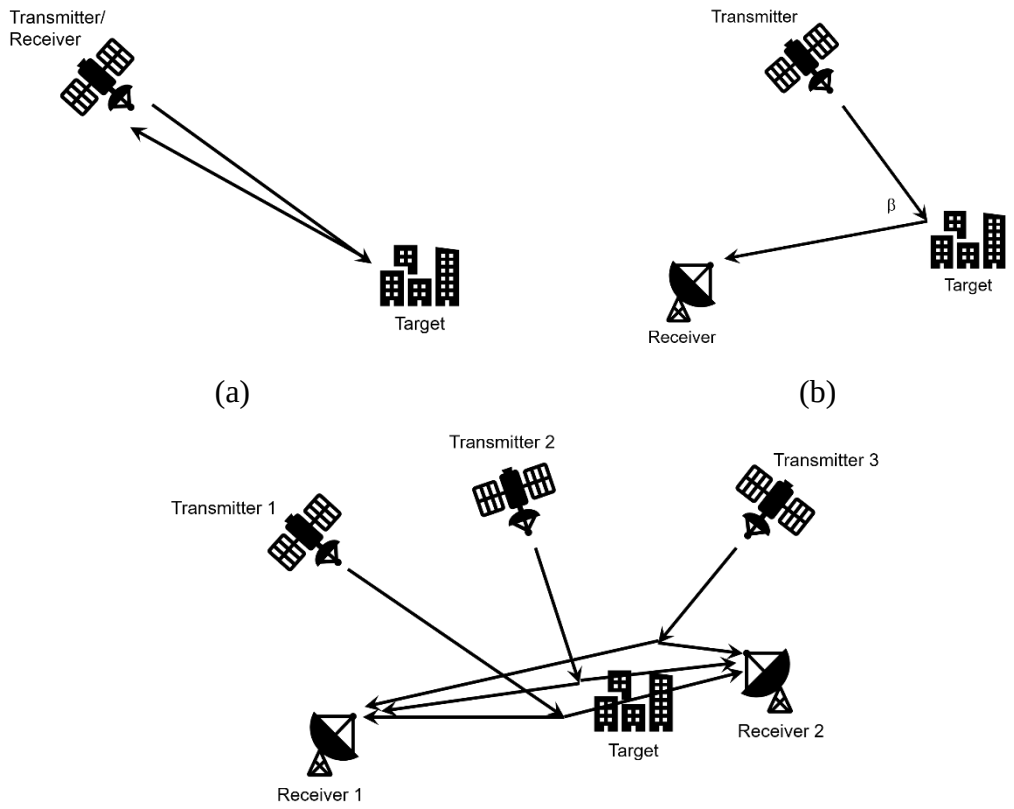

Figure 2.1 General radar topologies: (a) monostatic, (b) bistatic, and (c) multistatic, (adapted from [51])

The basic operation of the radar system, regardless of topology, comprises three parts: a transmitter, a receiver, and a target. The transmitter emits electromagnetic wave towards targets. Targets absorb some parts of signal while some other are reflected towards a receiver. A receiver measures these return signals. Relationship between the power of the signal during transmission, propagation, and reflection can be described using radar range equation (or commonly recognised as radar equation).

2.3 Radar Equation

The radar equation is the most fundamental equation for computing performance of a radar system at a given range. This performance includes minimum detectable power, maximum detectable range, and signal-to-noise ratio. The radar equation can be formulated in many forms depends on the complexity required. However, the underlying physics is the same for all forms [52]. This section firstly shows the radar equation in the form of the power received by the radar receiver and the other three performance parameters mentioned above then are derived.

One common form of the radar equation is used for predicting the power received by the radar receiver, [50]. Assuming a lossless propagation medium, it is defined as

$$P_r = \frac{P_t G_t}{4\pi R_t^2} \times \frac{\sigma}{4\pi R_r^2} \times \frac{G_r \lambda^2}{4\pi}. \tag{2.1}$$

where P_r is the power received by the radar receiver,

P_t is the power emitted by the radar transmitter,

G_t is the gain of transmitting antenna,

G_r is the gain of the receiving antenna,

R_t is a distance from the radar transmitter to the target,

R_r is a distance from the radar receiver to the target,

λ is the wavelength of the transmitted signal,

σ is the radar cross-section of the target.

For understanding the radar equation, Eq. 2.1 is divided into three groups of the variables. It is arranged in the form that reflects the physical process of signal propagation from the transmitter to the target and then the receiver. The first group ($P_t G_t / 4\pi R_t^2$) on the left-hand side is used for computing power flux density (power per unit area) at the target. It shows that the power P_t emitted from the radar transmitter of gain G_t is attenuated inverse proportionally to the squared distance between the radar transmitter and the target, R_t. This group of variables describes the total power flux density at the target, not the total power intercepted by the target. In the middle group ($\sigma / 4\pi R_r^2$), σ is target radar cross-section (RCS), expressed in dimensions of the area. It governs the total amount of power that the target can intercept. This intercepted power is computed by multiplying the RCS by the power flux density at the target. The term $4\pi R_r^2$ is applied to the intercepted power for determining the power flux density at the receiver in the target-to-receiver path, R_r. The product of the first and second group shows that the power flux density at the receiver is attenuated inverse proportionally to a squared distance between a target and a radar receiver. The last group, on the right-hand side, is the amount of the power that the radar receiver can intercept. It is controlled by the effective area of the antenna, A_e, where $A_e = \frac{G_r \lambda^2}{4\pi}$.

The radar equation in Eq. 2.1 is expressed based on a bistatic configuration where a transmitter and a receiver are in different locations. For monostatic configuration where a transmitter and a receiver are in co-location, the radar equation in Eq. 2.1 can be transformed by defining $R_t = R_r = R$ and $G_t = G_r = G$. As a result, Eq. 2.1 becomes

$$P_r = \frac{P_t G^2 \lambda^2 \sigma}{(4\pi)^3 R^4}. \tag{2.2}$$

The radar equation so far (Eq. 2.2) can be used for predicting received power at the receiver. For further investigating radar performance, maximum detectable range then is derived from Eq. 2.2. The maximum detectable range, R_{max}, is defined as the distance where the received power is equal to minimum detectable power, S_{min}. Therefore, Eq. 2.2 is modified to

$$R_{max} = \left(\frac{P_t G^2 \lambda^2 \sigma}{(4\pi)^3 S_{min}} \right)^{1/4}, \tag{2.3}$$

where S_{min} is minimum power that radar can detect. From Eq. 2.3, it suggests that doubling the radar maximum range requires increasing transmitted power sixteen times or increasing effective antenna area by a factor of four.

Please note that Eq. 2.2 is for a simplified case where only the significant parameters that affect the received power are considered. In real-world, performance at the later stages of the radar receiver is affected by more additional parameters than those in Eq. 2.2.

In a practical situation, the received signal is corrupted by receiver input noise. The receiver input noise power, N_i, is defined as

$$N_i = kT_sB, \tag{2.4}$$

where k is Boltzmann's constant (1.38×10^{-23} JK^{-1}) and B is a receiver operating bandwidth. T_s is the total effective system noise temperature which is defined as

$$T_s = T_e + T_a, \tag{2.5}$$

where T_e is the receiver effective noise temperature and $T_e = T_0(F_n - 1)$ while T_a is the antenna temperature. T_0 is the absolute temperature of the receiver and defined as 290 K (approximately room temperature). Substituting $T_e = T_0(F_n - 1)$ in Eq. 2.5 gives

$$T_s = T_0(F_n - 1) + T_a = T_0F_n - T_0 + T_a. \tag{2.6}$$

In many radar applications, it is desirable to set the antenna temperature equal to the absolute temperature of the receiver [53], and Eq. 2.6 is reduced to

$$T_s = T_0F_n, \tag{2.7}$$

where F_n is receiver noise figure. It is a ratio of signal-to-noise ratio (SNR) at the input and the output of the receiver and defined as

$$F_n = \frac{(SNR)_i}{(SNR)_o} = \frac{S_i/N_i}{S_o/N_o}, \tag{2.8}$$

where S_i and N_i are, respectively, the input signal and noise power while S_o and N_o are, respectively, the input signal and noise power. Using Eq. 2.7 in Eq. 2.4 and substituting the result into Eq. 2.8 yields

$$S_i = kT_0BF_n(SNR)_o. \tag{2.9}$$

Thus, S_{min} can be written as

$$S_{min} = kT_0BF_n(SNR)_{o_{min}}. \tag{2.10}$$

Substituting Eq. 2.10 in Eq. 2.3 yields

$$R_{max} = \left(\frac{P_tG^2\lambda^2\sigma}{(4\pi)^3kT_0BF_n(SNR)_{o_{min}}}\right)^{1/4} \tag{2.11}$$

or equivalently,

$$(SNR)_{o_{min}} = \frac{P_t G^2 \lambda^2 \sigma}{(4\pi)^3 k T_0 B F_n R_{max}^4}. \tag{2.12}$$

For more accurate and realistic analysis, radar loss factors (L), e.g., atmospheric loss, antenna pattern loss, and transmit and receive losses, are added to the radar equation. In this case $L < 1$ and Eq. 2.12 becomes

$$SNR_o = \frac{P_t G^2 \lambda^2 \sigma L}{(4\pi)^3 k T_0 B F_n R^4}. \tag{2.13}$$

The restriction of Eq. 2.13 is that the antenna temperature must be 290K. In real-world situations, the antenna temperature may vary from a few degrees Kelvin to several thousand degrees. Thus, for more general case that accounts for the antenna temperature, the radar equation is expressed as

$$SNR_o = \frac{P_t G^2 \lambda^2 \sigma L}{(4\pi)^3 k T_s B R^4}. \tag{2.14}$$

Please note that additional parameters can be further added to the radar equation (Eq. 2.14) depends on which stage of the analysis chain is required.

2.4 Radar Cross Section (RCS)

Radar cross-section (σ in Eq. 2.14) is an area of the target that can scatter power to the radar receiver. RCS can be calculated using the ratio of the power intercepted by the target to the power scattered to the radar receiver as

$$\sigma = \lim_{R \to \infty} 4\pi R^2 \left| \frac{P_{sca}}{P_{inc}} \right|^2 \tag{2.15}$$

where P_{sca} is the power of the scattered wave received by the radar receiver,

P_{inc} is the power of the incident on the target,

R is the distance from the target to the radar.

The term $\lim_{R\to\infty}$ is to ensure that the radar receiver is in the far-field so that scattered wave received by the receiving antenna is planar. Define the angles $(\theta_{inc}, \varphi_{inc})$ as the direction of propagation of the incident wave in the spherical coordinate system. Also, define the angles $(\theta_{sca}, \varphi_{sca})$ as the direction of propagation of the scattered wave. The RCS measured at angles $\theta_{sca} = \theta_{inc}$ and $\varphi_{sca} = \varphi_{inc}$ is defined as the monostatic RCS, otherwise is called the bistatic RCS.

RCS has dimensions of the area, usually in square metre (m^2), but they can also be presented in logarithmic units of dBsm, which is dB relative to a 1 m^2 reference area. RCS does not equal to the geometrical area. For example, RCS of a large sphere ($\lambda \ll r$) is πr^2, where r is the radius of the sphere. Some examples of maximum RCS of simple shapes whose size is much greater than λ are shown in Table 2.1, [54].

Table 2.1 examples of maximum RCS of simple shapes

Simple Shape	RCS
Sphere, radius $\boldsymbol{r}$	πr^2
Flat plate, edge lengths $\boldsymbol{a}$ and $\boldsymbol{b}$	$4\pi(ab)^2/\lambda^2$
Dihedral, edge lengths $\boldsymbol{a}$ and $\boldsymbol{b}$	$8\pi(ab)^2/\lambda^2$
Trihedral, square sides, edge lengths $\boldsymbol{a}$	$12\pi a^4/\lambda^2$
Trihedral, triangular sides, edge lengths $\boldsymbol{a}$	$4\pi a^4/3\lambda^2$

2.5 Matched Filter

Maximising the SNR is key in all radar applications. The matched filter (MF) is the optimum linear filter for this purpose because it can produce the maximum achievable SNR at its output when the transmitted signal plus noise are received at its input. This section shows the derivation of the MF in the case that received signal corrupted by white noise which is a common assumption in the microwave radar receiver. The general form of the instantaneous SNR is firstly derived, and it then is used for obtaining impulse response of the optimum filter that can maximise the SNR. The band-limited white noise then is added to the optimum filter, and consequently, the MF for this case can be obtained. The SNR for this specific case is also derived and shows the more straightforward form than its general version. The output signal of the MF is obtained lastly. Please note that the detailed derivation of those shown in this section can be found in Chapter 4 of [53]

Let defined x_o as the output signal, n_i as the input noise signal, n_o as the output noise signal, and h as the optimum filter impulse response. The signal at the output of the optimum filer is defined as

$$y(t) = x_o(t - t_0) + n_o(t), \tag{2.16}$$

where

$$n_o(t) = n_i(t) \otimes h(t), \tag{2.17}$$

$$x_o(t) = x(t - t_0) \otimes h(t), \tag{2.18}$$

and the operator $\otimes$ denotes convolution.

Using Fourier transform and Parseval's theorem to Eq. 2.17 and Eq. 2.18 yields, respectively, the total power of signal and noise as

$$E_x = \left| \int_{-\infty}^{\infty} X(f)H(f)e^{j2\pi f t_0} df \right|^2, \tag{2.19}$$

$$N_o = \int_{-\infty}^{\infty} N_i(f)|H(f)|^2 df. \tag{2.20}$$

As a result, the general form of the instantaneous SNR at the output of the MF at time t_0, can be calculated by

$$SNR(t_0) = \frac{\left|\int_{-\infty}^{\infty} X(f)H(f)e^{j2\pi f t_0} df\right|^2}{\int_{-\infty}^{\infty} N_i(f)|H(f)|^2 df} = \frac{E_x}{\int_{-\infty}^{\infty} N_i(f)|H(f)|^2 df}. \tag{2.21}$$

Applying Schawrz's inequality, which is defined as

$$\frac{\left|\int_{-\infty}^{\infty} X_1(f)X_2(f)df\right|^2}{\int_{-\infty}^{\infty}|X_1(f)|^2 df} \leq \int_{-\infty}^{\infty}|X_2(f)|^2 df, \tag{2.22}$$

to Eq. 2.21 with assumptions that

$$X_1(f) = H(f)\sqrt{N_i(f)}, \tag{2.23}$$

$$X_2(f) = \frac{H(f)e^{j2\pi f t_0}}{\sqrt{N_i(f)}}, \tag{2.24}$$

and $X_1(f) = CX_2^*(f)$ for some arbitrary constant C to change from less-than-or-equal-to sign to equal sign, results in the transfer function for the optimum filter that maximises SNR as

$$H(f) = C\frac{X^*(f)e^{-j2\pi f t_0}}{N_i(f)}. \tag{2.25}$$

The asterisk $(*)$ superscripted to X_2 denotes the complex conjugate.

Re-arranging Eq. 2.25 gives

$$X(f)H(f)e^{-j2\pi f t_0} = \frac{C|X(f)|^2}{N_i(f)}. \tag{2.26}$$

By taking inverse Fourier Transform integral, the impulse response of the optimum filter (to maximise the SNR) then is

$$h(t) = \int_{-\infty}^{\infty} C\frac{X^*(f)e^{-j2\pi f t_0}}{N_i(f)} e^{j2\pi f t} df. \tag{2.27}$$

In the case that white noise, where $N_i(f) = \eta_0/2$, is presented at the input of the receiver, Eq 2.27 becomes

$$h(t) = x^*(t_0 - t). \tag{2.28}$$

The impulse response in Eq. 2.28 is matched to the input signal. Hence the term matched filter is used for this case (white noise). In such a case, the peak instantaneous SNR at the output of the MF is

$$SNR(t_0) = \frac{2E_x}{\eta_0}. \tag{2.29}$$

The SNR in Eq. 2.29 has a more straightforward form than that the general form (Eq. 2.21) when the white noise is presented at the input of the receiver. Equation 2.29 indicates that the SNR depends only on the total energy of the received signal and input noise power.

Furthermore, it also indicates that the maximum SNR is independent of the shape of the radar waveform used.

2.6 Waveform Resolution and Ambiguity

Characteristics of range and Doppler resolution can be determined using the output of the MF.

This section derives range and Doppler resolution using their ambiguity function.

2.6.1 Range Resolution

Assume the transmitted signal is defined as

$$x(t) = r(t)\cos\big(2\pi f_0 t + \phi(t)\big), \tag{2.30}$$

where $r(t)$ is the amplitude modulation, f_0 is the carrier frequency, and $\phi(t)$ is the phase modulation. The return signal from two targets in proximity to each other is given by

$$x_1(t) = \tilde{x}(t), \tag{2.31}$$

$$x_2(t) = \tilde{x}(t-\tau), \tag{2.32}$$

where τ is the difference in delay between the two target returns. This difference (squared error) is denoted as ε_R^2 and expressed as

$$\varepsilon_R^2 = \int_{-\infty}^{\infty} |\tilde{x}(t) - \tilde{x}(t-\tau)|^2 dt = \tag{2.33}$$

$$2\int_{-\infty}^{\infty} |\tilde{x}(t)|^2 dt - 2Re\left\{e^{-j\omega_0\tau}\int_{-\infty}^{\infty} \tilde{x}^*(t)\tilde{x}(t-\tau)dt\right\}.$$

The range correlation function is defined as the integral term on the rightmost,

$$\chi_R(\tau) = \int_{-\infty}^{\infty} \tilde{x}^*(t)\tilde{x}(t-\tau)dt. \tag{2.34}$$

Equation 2.34 indicates that the range ambiguity function is an autocorrelation function and equivalent to the output of the MF with no round trip delay. This equation can be interpreted that the MF does maximise not only the SNR but also maintain range resolution performance. The term on the right-hand side of Eq. 2.34 is computed and yields the squared magnitude of the range ambiguity function, $|\chi_R(\tau)|^2$. This squared magnitude has the maximum value when $\tau = 0$, i.e., $\chi_R(0)$. Resolvability of the two targets in the range can be measured by following that the two targets are

$$\text{not resolvable if } |\chi_R(\tau)| = \chi_R(0), \text{ for some nonzero value of } \tau, \tag{2.35}$$

$$\text{resolvable if } |\chi_R(\tau)| \neq \chi_R(0), \text{ for some nonzero value of } \tau.$$

Equation 2.35consequently yields the desired shape for the $\chi_R(\tau)$ that it should have a sharp peak centred at $\tau = 0$ and falling steeply otherwise.

Range resolution (ΔR) is the ability to separate two targets near to each other as two distinct objects in range direction. The minimum range resolution corresponds to the effective time duration (τ_e) and $\tau_e = \tau_1 - \tau_2$ or the effective bandwidth B_e of the waveform, is defined as

$$\Delta R = \frac{c\tau_e}{2} = \frac{c}{2B_e}. \tag{2.36}$$

where the conversion between τ_e and B_e is referred to as the time bandwidth product ($\tau_e B_e$) and Eq. 2.36 assumes that $\tau_e B_e = 1$.

2.6.2 Doppler Resolution

The Doppler frequency corresponds to the target radial velocity is defined as

$$f_d = \frac{2v}{\lambda} = \frac{2vf_0}{c}, \tag{2.37}$$

where v is the target radial velocity. The Doppler shift will cause the received signal spectrum shifted by f_d. Using the analysis similar to the range ambiguity function, the Fourier transform of the return signal from the two targets at the same range but having different velocities are

$$X_1(f) = \tilde{X}(f), \tag{2.38}$$

$$X_2(f) = \tilde{X}(f - f_d), \tag{2.39}$$

then

$$\varepsilon_f^2 = \int_{-\infty}^{\infty} \left|\tilde{X}(f) - \tilde{X}(f - f_d)\right|^2 df. \tag{2.40}$$

Using the manner similar to obtain Eq. 2.33 results in the frequency correlation function as

$$\chi_f(f_d) = \int_{-\infty}^{\infty} \tilde{X}^*(2\pi f)\tilde{X}(2\pi f - 2\pi f_d)df = \int_{-\infty}^{\infty} |\tilde{x}(t)|^2 e^{j2\pi f_d t} dt. \tag{2.41}$$

Doppler resolution (Δf_d) is the ability to resolve the difference between two Doppler frequencies corresponds to the two targets with different velocities. It is defined as the inverse of the effective duration of the waveform,

$$\Delta f_d = \frac{1}{\tau_e} \tag{2.42}$$

In can be used for determining the velocity resolution as follow

$$\Delta v = \frac{c\Delta f_d}{2f_0}. \tag{2.43}$$

2.6.3 Ambiguity Function

Different between transmitting a signal as a two-dimensional function, $\tilde{x}(t)e^{j2\pi f_0 t}$, and its delayed and Doppler-shifted version, $\tilde{x}(t-\tau)e^{j2\pi(f_0-f_d)(t-\tau)}$ can be expressed in squared error form as

$$\varepsilon^2 = 2\int_{-\infty}^{\infty}|\tilde{x}(t)|^2 dt - 2Re\left\{e^{j2\pi(f_0-f_d)\tau}\int_{-\infty}^{\infty}\tilde{x}(t)\tilde{x}^*(t-\tau)e^{j2\pi f_d t}dt\right\}. \tag{2.44}$$

Using similar analysis for the correlation functions in range (Eq. 2.33) and frequency (Eq. 2.41), the range-Doppler correlation function is defined as

$$\chi(\tau, f_d) = \int_{-\infty}^{\infty}\tilde{x}(t)\tilde{x}^*(t-\tau)e^{j2\pi f_d t}dt. \tag{2.45}$$

Equation 2.45, is often referred to as the ambiguity function. The ambiguity function is used for determining the spatial resolution performance of the given radar waveform by measuring its most achievable range and Doppler resolutions. These resolutions can be determined using the squared modulus of the ambiguity function.

2.7 Coherence

Coherence is the ability to maintain the phase relationship of any two transmitted signals. It also the ability to accurately measure the phase of the received signal which can use coherent-on-receive.

2.8 Synthetic Aperture Radar (SAR)

As aforementioned that useful information can be derived from detected radar echo. The information enables numbers of radar applications, e.g. tracking radar, weather radar, or ground-penetrating radar. One of the most essential radar applications is synthetic aperture radar (SAR), [55], which is an imaging system widely used for remote sensing. SAR also fundamentals of this thesis. SAR can be categorised by the topology as same as a general radar system, that is monostatic, bistatic, and multistatic SAR.

Synthetic aperture radar (SAR) is an imaging radar that can obtain high spatial resolution images of the Earth's surface by using signal processing technique. SAR was theoretically developed in 1951 by Carl Wiley of the Goodyear Aircraft Corporation. Between 1952 and 1953, a group of researchers from University of Illinois experimentally demonstrated similar concept using X-band radar system mounted on-board C-46 aircraft, [56], hence SAR was first introduced using a monostatic configuration.

SAR concept, theory, and signal processing are derived in [57]. The following sections reiterate that works.

2.9 Linear Frequency Modulation (LFM) Signal

The ideal LFM signal has a duration T with a constant amplitude and a frequency centre f_c. In the time domain, the LFM signal is defined as

$$s(t) = \text{rect}\left(\frac{t}{T}\right) e^{j\pi K t^2}, \tag{2.46}$$

where t is time in seconds and K is the linear FM rate. The signal is called linear because the frequency is a linear function of time t with the slope K. The signal is often referred to as chirp signal which is analogous to bird's chirp. When the frequency slope is positive, the signal is called up chirp. Otherwise, when the slope is negative, the signal is called down chirp.

In the frequency domain, the spectrum of Eq. 2.46 can be derived using the Principle of Stationary Phase (POSP). As a result, the spectrum is presented as

$$G(f) = \text{rect}\left(\frac{f}{KT}\right) e^{-j\pi\frac{f^2}{K}}. \tag{2.47}$$

The bandwidth of the signal is defined as the product of the slope and the signal duration

$$BW = |K|T. \tag{2.48}$$

This bandwidth defines the achievable resolution. The time bandwidth product (TBP), which is defined as the product of 3-dB width in time and 3-dB bandwidth of the signal, is given by

$$TBP = |K|T^2. \tag{2.49}$$

2.10 Pulse Compression

Pulse compression is a method to minimise peak power while maximising the SNR and obtain a fine resolution of the sensed object. One way to increase SNR without increasing transmitting power is transmitting an expanded pulse duration and later, after receiving, compress the received pulse to the desire resolution. Good pulse compression requires the magnitude spectrum of the received signal to be reasonably flat, and phase has only constant and linear terms. This can be achieved using LFM signal due to the properties of the LFM that it has near-flat spectrum. However, this flat spectrum is obtained by the quadratic term in-phase component of the time domain LFM. The quadratic phase also presented in the spectrum of the LFM. By multiplying the spectrum of the LFM by similar spectrum with the conjugate quadratic phase component can yield the linear phase. The desired sinc function is then obtained by taking inverse Fourier transform to the spectrum. This process terms the pulse compression as a matched filter because the filter is matched to the expected phase of the received signal.

The compressed signal has the resolution, measured at 3-dB below the peak, is defined as

$$\delta = \frac{0.886}{|K|T} \approx \frac{1}{|K|T} = \frac{1}{BW'}, \tag{2.50}$$

where δ is pulse resolution expressed in time unit, and the factor of 0.886 is the width of the peak measured at 3-dB. This factor can be ignored in the approximation when a smoothing window is used. The chirp bandwidth $|K|T$ is reciprocal of the resolution and indicates that a wider bandwidth gives a finer resolution. This resolution is also called the impulse response width (IRW) since the output of the matched filter defined is the response to a point target.

2.11 SAR Signal

The most common signal used in SAR has linear FM characteristic

$$s_{pul}(\tau) = \omega_r(\tau)\cos\{2\pi f_0\tau + \pi K_r\tau^2\}, \tag{2.51}$$

where K_r is the FM rate of change of the range pulse,

τ is a fast time, i.e., speed of light,

ω_r is the pulse envelope and $\omega_r = \text{rect}\left(\frac{\tau}{T_r}\right)$,

T_r is pulse duration.

From Eq. 2.50, the range resolution can be expressed in the unit of distance by multiplying with the speed of light and is

$$\delta_r \approx \frac{c}{2}\cdot\frac{1}{|K_r|T_r} = \frac{c}{2BW}, \tag{2.52}$$

where the factor of two accounts for round trip propagation and BW is the bandwidth of the transmitted signal.

The reflected signal from the illumination area has defined the convolution of the pulse waveform and the ground reflectivity g_r, and is

$$s_r(\tau) = g_r(\tau)\otimes s_{pul}(\tau), \tag{2.53}$$

Considering the point target located at a distance R_a gives the received signal as

$$s_r(\tau) = A_0' s_{pul}\left(\tau - \frac{2R_a}{c}\right) = \tag{2.54}$$

$$A_0' \omega_r\left(\tau - \frac{2R_a}{c}\right) \times \cos\left\{2\pi f_0\left(\tau - \frac{2R_a}{c}\right) + \pi K_r\left(\tau - \frac{2R_a}{c}\right)^2 + \psi\right\}$$

where $g_r(\tau) = A_0'\delta(\tau - 2R_a/c)$, A_0' is the magnitude of ground reflectivity, $2R_a/c$ is the delay time for the target, and ψ is phase change caused by the scattering process. After quadrature demodulation, the radar carrier frequency component ($\cos 2\pi f_0\tau$) will be removed. Thus, the resultant signal is then in the order of the transmitted signal bandwidth.

Pules are transmitted every $1/PRF$ as the SAR platform move along its path. The term R_a now changes with slow time (u), i.e. platform velocity, hence R_a is changed to $R(u)$. The received signal in two-dimension can be expressed as

$$s_0(\tau, u) = A_0 \omega_r\left(\tau - \frac{2R(u)}{c}\right)\omega_a(u - u_c) \tag{2.55}$$

$$\times e^{-j4\pi f_0 \frac{2R(u)}{c}} \times e^{j\pi K_r\left(\tau - \frac{2R(u)}{c}\right)^2},$$

where A_0 is a complex form of A_0' and $A_0 = A_0' e^{j\psi}$ and ω_a is received signal strength.

The strength of each pulse varies and depends on the azimuth beam pattern. Maximum strength occurs when the target lies in the centre of the beam. For the Doppler frequency, it is proportional to the target's radial frequency with respect to the platform. Doppler frequency is positive when the target is approaching the radar and is negative when the target is departing the radar. The time that the target stays within the 3-dB width of the beam is called the exposure time which, for a zero squint angle case, is defined as

$$T_a = \frac{\lambda R(u_c)}{L_a V_g}, \tag{2.56}$$

where L_a is the antenna length, λ/L_a is the azimuth beamwidth (θ_{bw}), $R(u_c)$ is the range at the time that Doppler frequency is zero, $\lambda R(u_c)/L_a$ is the projection of the beamwidth onto the ground, V_g is the velocity of the beam footprint along the Earth's surface. This velocity is caused by the platform altitude drift. In the case that the beam has a nonzero squint angle ($\theta_{r,c}$) the projection will be lengthened by a factor of $1/\cos\theta_{r,c}$.

In the case of real aperture radar, the azimuth resolution is defined as the projection of the azimuth beamwidth onto the ground. It is expressed as

$$\delta_{a,real} = R(u_c)\theta_{bw} = \frac{\lambda R(u_c)}{L_a}. \tag{2.57}$$

In the case of synthetic aperture, the azimuth resolution is defined as reciprocal of the bandwidth (Doppler bandwidth), and express in distance unit as

$$\delta_a = \frac{V_g}{\Delta f_d} = \frac{V_g}{2V_s L_a} = \frac{L_a}{2} \cdot \frac{V_g}{V_s}. \tag{2.58}$$

where $V_s$is satellite velocity and $V_g/V_s \approx 1$ in the satellite case.

Therefore,

$$\delta_a = \frac{L_a}{2}. \tag{2.59}$$

Equation 2.59 indicates that the azimuth resolution is approximately one-half of the antenna length.

2.12 Monostatic SAR

For imaging radar, one of the most important characteristics is the spatial resolution that usually is in track (or azimuth) and cross-track (or range) directions, [58]. Considering a real aperture radar case, range and azimuth resolution ($\delta_{r,real}, \delta_{a,real}$) can be determined, respectively, using Eq. 2.52 and 2.57. From Eq. 2.52, range resolution can be improved by using higher bandwidth of transmitting a signal which is feasible. However, from Eq. 2.57, azimuth resolution can be improved by increasing either carrier frequency (to reduce wavelength) or physical length of the antenna. Both cases are impractical, for example, azimuth resolution of 1 km at 1 km range using L-band radar of 1.5 GHz requires an antenna length of 200 m, [55]. Also, frequency is inflexible to be changed due to selecting frequency is based on applications, e.g. L-band frequency is suitable for forest monitoring.

SAR is a feasible technique to improve azimuth resolution using moving radar (usually aircraft or satellites) with signal processing approach instead unrealistic by increasing antenna's physical dimension. It records a sequence of echoes from a target during moving of a platform. The total distance of moving path that a target is illuminated defined a synthetic long antenna beam. As a result, a long antenna beam can be virtually realised using a small antenna (Figure 2.2 (a)). An image of a target is generated by combining all recorded echoes of that target accordingly, hence a focused image of a target Figure 2.2 (b)). It is noted that antenna movement is essential for aperture synthesis. Therefore, at least one moving part is required either a platform or a target.

With SAR technique, azimuth resolution (δ_a) can be determined using Eq. 2.59. In this case, azimuth resolution can be improved by reducing effective length of the physical antenna, which contradict a real aperture case. Equation 2.59 shows that azimuth resolution from SAR

is much improved over the real aperture case. For example, if the antenna size of 200 m is used (as in the previous example), SAR can provide resolution of 100 m, which is ten times finer than the real aperture case.

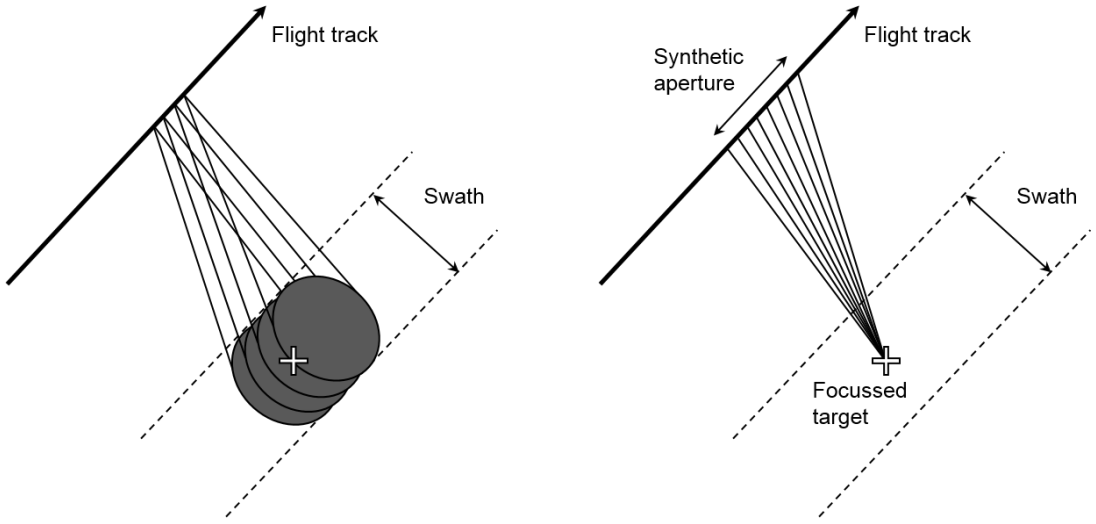

Figure 2.2 Synthetic aperture concept (a) illuminating a target continuously and (b) synthesising a long antenna, (adapted from [58])

During aperture synthesis, SAR system moves, and its antenna illuminates a target. The antenna beam can be perpendicular to a platform's track or offset by some angles. The former is referred to as broadside SAR whereas the latter is squint SAR. Either type of beam orientations, echoes collected during aperture synthesis are assumed to be recorded in two dimensions. The first dimension is along an antenna beam and defined as fast-time (or range-time). It is associated with SAR signal that used to illuminate a target, which travels at a speed of light. The second dimension is along a platform's track and defined as slow-time (or azimuth-time). It is associated with a platform position during creating aperture.

Since SAR signal is much faster than a platform velocity, hence the term fast-time and slow-time. A process of recording echoes, which can be referred to as imaging, is based on stop-and-go assumption, [55]. At each instant in slow-time direction, SAR platform stops, transmits the signal, and then records echoes. Transmitting and receiving are over a specific time interval in fast-time direction. Once time interval is reached, a platform advances to a next slow-time position. Figure 2.3 shows monostatic SAR imaging geometry. In this configuration, SAR platform is denoted as Tx/Rx (both are co-located). The platform moves along the path which its velocity V_T in this direction is considered as slow time (compared to speed of light). The target is located at distance (or range) R_0 away from the origin. Imaging area has a scene centre at R_c. R_1 is at another end of the imaging area and opposite to the target. Direction toward R_1 is forward range. $R(u)$ is an instantaneous range at time u while R_0 is a range from the point where the centre of the antenna beam crosses the target and Doppler frequency is zero.

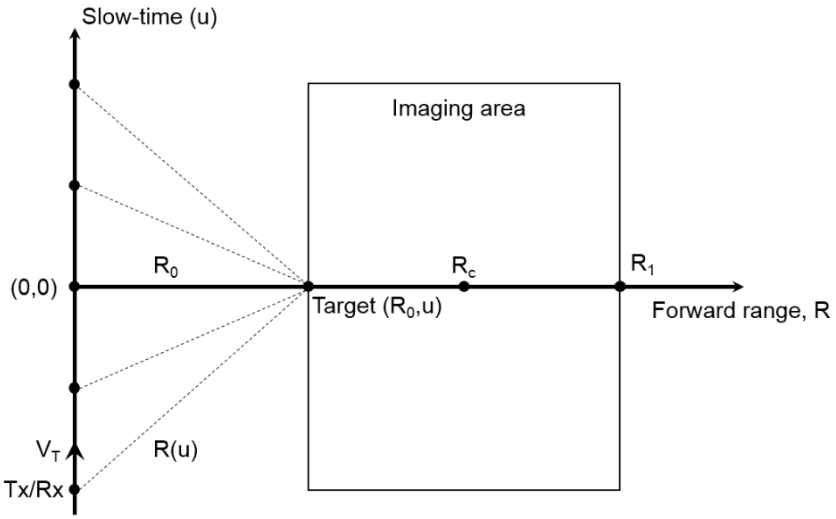

Figure 2.3 Monostatic SAR imaging geometry, (adapted from [55])

SAR operation can be categorised into some different imaging modes, [57]. The main three different modes that are widely used are stripmap, spotlight, and ScanSAR. Figure 2.4 visualises the operation of imaging modes. In stripmap mode, an antenna beam is fixed and sweep an imaging area as a platform moves. Length of the scene being illuminated is equal to the distance that a platform travels and azimuth beamwidth of an antenna. Azimuth resolution is governed by a physical antenna length since the antenna beamwidth is proportional to antenna size. Narrow beamwidth provides a short period of dwell time on a target.

For spotlight mode, an antenna beam is steered forward as a platform approach a target and start to steer backwards as a platform passes a target. This process increases dwell time on target, which is one of the parameters that define Doppler bandwidth. Increasing the Doppler bandwidth consequently improves azimuth resolution. As a result, this mode provides higher azimuth resolution than stripmap, which is limited by the length of an antenna. Target area cannot be continuously observed by this mode due to an antenna have to steer from the backward position at the previous scene to forward position before starting of imaging the next scene. During that change, the spotlight cannot collect echoes; hence no target is imaged.

In ScanSAR, multiple stripmap operations are used with steering antenna in elevation (i.e. different incident angles). Among the three modes, ScanSAR can cover the largest area, which is formed by overlapping individual scenes from each stripmap. Azimuth resolution from this mode is degraded compared to a stripmap mode because the resolution is equal to that of the stripmap multiplied by the number of swaths scanned.

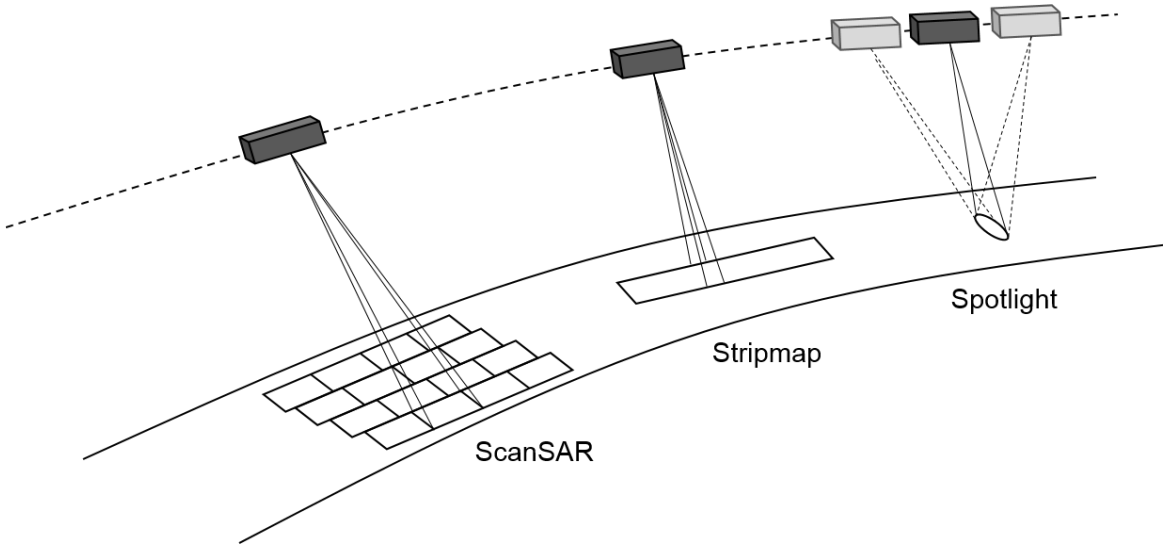

Figure 2.4 Typical SAR imaging modes: ScanSAR, Stripmap, and Spotlight (from left to right), (adapted from [59])

For power consideration, SNR in monostatic SAR system can be determined using the radar equation from Eq. 2.14, which is based on a single-pulse assumption. To determine monostatic SAR SNR, the RCS (σ) in Eq. 2.14 has to be more precisely modelled and coherently integrated pulses is assumed. In monostatic SAR, an RCS is a function of resolution cell and terrain reflectivity, and it can be precisely expressed as

$$\sigma = \sigma^0 \delta_{rg} \delta_{ag}, \tag{2.60}$$

where σ^0 is a normalised RCS, δ_{rg} is a ground range resolution and δ_{ag} is ground azimuth resolution. The normalised RCS is total RCS from a distributed scatterer on the ground per unit area (i.e. normalised by the area), and is

$$\sigma^0 = E\left[\frac{\sigma_i}{A_i}\right], \tag{2.61}$$

where $E[\cdot]$ is the expectation operation which computes average value, σ_i and A_i are respective RCS and area of a single scatterer. The normalised RCS is used for describing the backscatter properties of a pixel area comprising several different backscattered. In general, it has a significant variation with incidence angle (i.e. illuminating geometry), wavelength, and polarisation, as well as with properties of the scattering surface itself (Figure 2.5). For example, in variation with the frequency (wavelength) case, the longer wavelength can penetrate more in-depth than the shorter wavelength. In case the same frequency is used, the penetration depth can also vary according to the different polarisation. Another example, in variation with the terrain properties case, the water content in soil or vegetation yields higher reflectivity of radar waves. Furthermore, the flat surface shows an extremely low backscatter while a rough surface gives a higher reflectance.

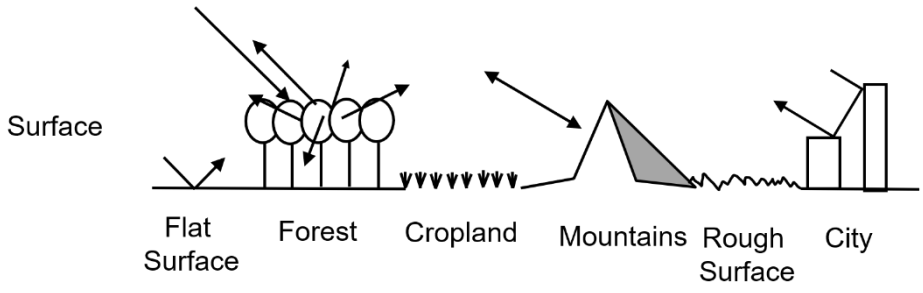

Figure 2.5 Example of radar reflection from different objects (source: http://gis.humboldt.edu/OLM/Courses/GSP_216_Online/lesson7-2)

For an assumption of coherently integrated pulses, number of pulses (n) within dwell time on a target (T_c) can be expressed as

$$n = PRF \cdot T_c = PRF \cdot \frac{L_c}{V_T} = \frac{\lambda R \cdot PRF}{2\delta_{ag} \cdot V_T \cdot sin\psi}, \tag{2.62}$$

where PRF is a pulse repetition frequency, L_c is a length of synthetic aperture, V_T is a velocity of a transmitting platform and ψ is an off-nadir angle of transmitting beam. During

a dwell time on target, power transmitted from the SAR system is considered as an average power, which is written as

$$P_{av} = (P_t/B)PRF. \tag{2.63}$$

As a result, Monostatic SAR SNR can be determined by SNR of a single pulse from Eq. 2.14 times number of pulses within a dwell time on target. Substituting Eq. 2.60 and Eq. 2.62-2.63 into Eq. 2.14, thus SAR SNR can be written as

$$SNR = \frac{P_{av}G^2\lambda^3\sigma^0 L_s \delta_{rg}}{(4\pi)^3 kT_0 F_n R^3 2V_T sin\psi}. \tag{2.64}$$

Comparing Eq. 2.14 and Eq. 2.64, they are both proportional to a wavelength of transmitting signal and inversely proportional to range but different powers (2 vs 3). In contrast to Eq. 2.14, the monostatic SAR SNR (Eq. 2.64) also is a function of ground range resolution and velocity of transmitting platform whereas Eq. 2.14 is not. It is noted that SAR SNR is independent from a ground azimuth resolution. The detailed derivation of SAR radar equation can be found in [53].

2.13 Bistatic SAR

In bistatic SAR, a transmitter and a receiver are placed at a different location. An advantage of platform separation over the monostatic case is that bistatic SAR can increase information space of a target area. Figure 2.6 shows a general bistatic imaging geometry. Some notations shown in Figure 2.6 are the same as defined in Figure 2.3. In the bistatic configuration, the transmitter and the receiver are located at a different place and move along their own path with a respective velocity V_T and V_R. Instantaneous range $R_R(u)$ and $R_T(u)$ as well as range

R_{R0} and R_{T0} has similar definition as $R(u)$ and R_0 in monostatic SAR. The path along the transmitter-target-receiver spans the bistatic plane.

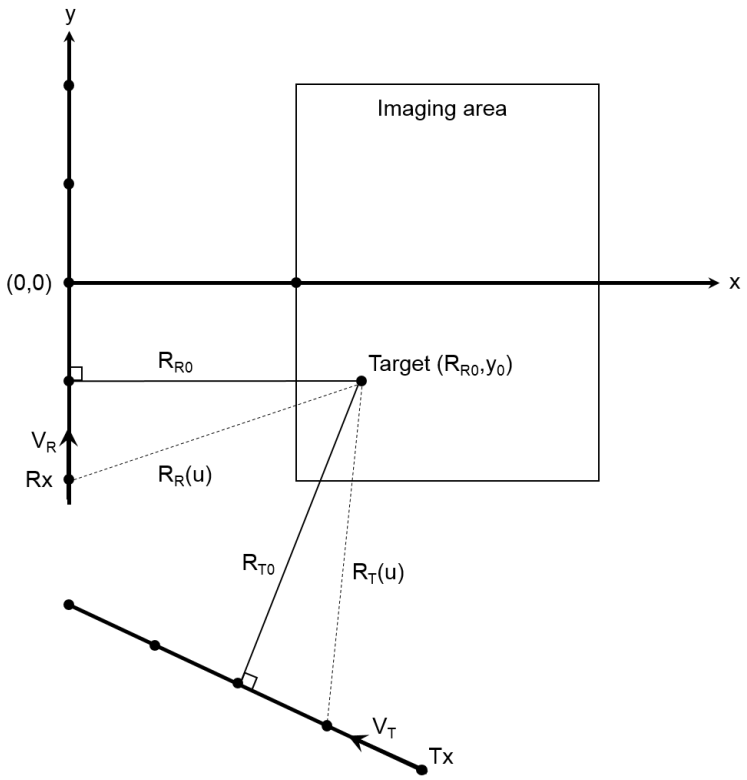

Figure 2.6 General bistatic SAR imaging geometry, (adapted from [55])

The spatial separation of platforms in the bistatic case enables its sub-class based on the types of platform used as the transmitter and the receiver (Figure 2.7). For both moving platforms case, bistatic SAR topology can be categorised as airborne, spaceborne, and hybrid (Figure 2.7 (a)-(c)). In spaceborne bistatic SAR, both the transmitter and the receiver are a satellite whereas they are an aircraft in case airborne bistatic SAR case. For hybrid case, this topology provides various combinations of a transmitter and a receiver. For example, it can be a combination between different kind of platforms, e.g. a satellite and an aircraft or an aircraft and a ground vehicle. Alternatively, either a transmitter or a receiver can be a

stationary platform (Figure 2.7 (d)), e.g. a DVBT station. The only condition is that at least one moving platform must be used for synthesising aperture.

Space-surface bistatic SAR (SS-BSAR) is a particular case of the hybrid bistatic SAR. In this topology, a transmitter is a satellite, and a receiver is a low-altitude platform, e.g. an aircraft, a ground moving vehicle or a stationary receiver. Global navigation satellites systems (GNSS) are one of the transmitter candidates. A configuration using a GNSS satellite and a single receiver has been considered on theoretical and experimental level for several years. Its potential has been demonstrated with both moving and fixed receiver.

As a transmitter and a receiver are not co-located, angular separation (bistatic angle, β) between them is a factor that governs range resolution of bistatic SAR. The bistatic range resolution ($\delta_{rg,bistatic}$), [9], are not only a function of the bandwidth of transmitting signal but also a bistatic angle. It can be written as

$$\delta_{rg,bistatic} = \frac{c}{2Bcos(\beta/2)}. \tag{2.65}$$

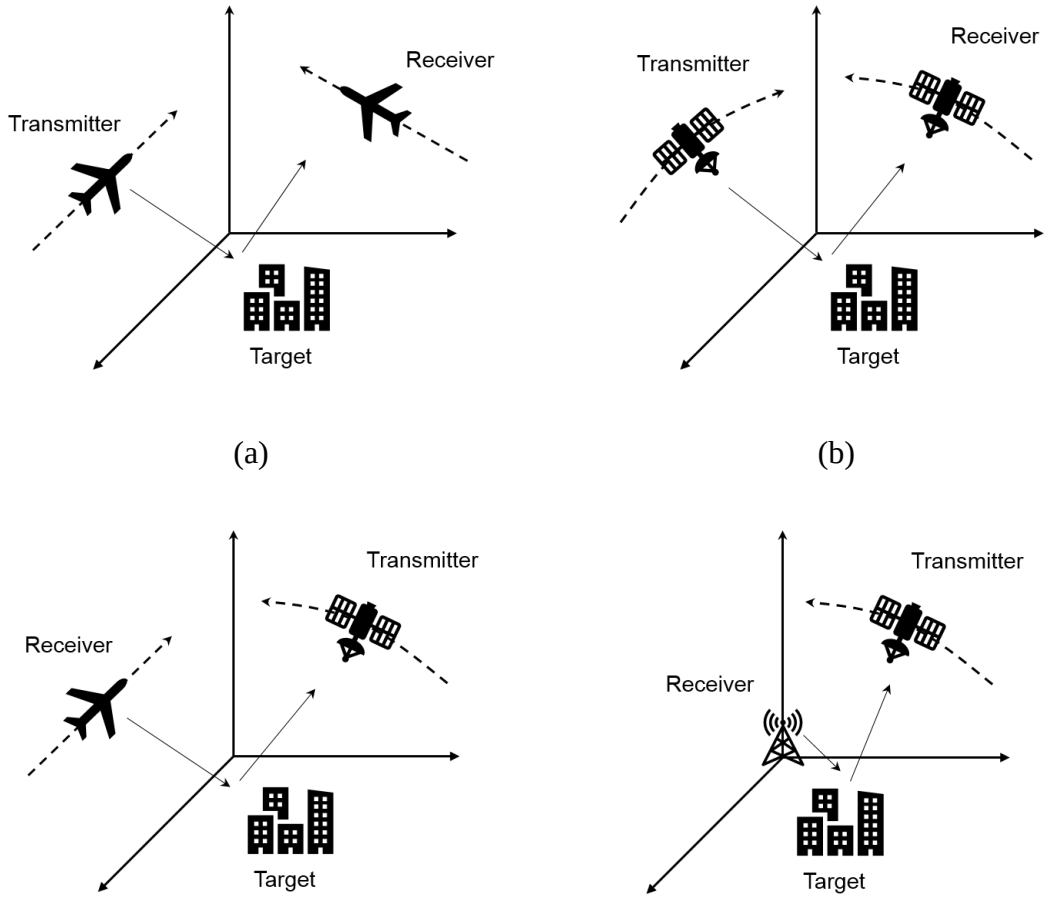

Figure 2.7 Example bistatic SAR configurations (a) airborne TX - airborne RX (b) spaceborne TX - spaceborne RX (c) spaceborne TX - airborne RX and (d) spaceborne TX - ground-based RX, (adapted from [51])

From Eq. 2.65, when a bistatic angle is nearly 0˚, the range resolution is optimum value. A configuration that yields the optimum range resolution is referred to as quasi-monostatic configuration.

For azimuth resolution, it can be determined by

$$\delta_a = \frac{\lambda R}{L_c}, \tag{2.66}$$

where R is the distance from the dominating platform to a target, L_c is a length of synthetic aperture and L_c is a product of a velocity-dominated platform and dwell time on a target (T_c). For example, if a stationary satellite is used with an aircraft carrying a receiver, azimuth resolution is dominated by an aircraft velocity (V_R), thus, $L_c = V_R T_c$.

2.14 Multistatic SAR

Multistatic SAR uses multiple transmitters and receivers. It can be considered as a combination of multiple bistatic SAR systems. Individual bistatic geometry is referred to as a bistatic pair. Figure 2.8 shows multistatic imaging geometry, which is extended from a bistatic geometry in Figure 2.6. In this case, three bistatic pairs (Tx1-Rx, Tx2-Rx, and Txn-Rx) are used to form a multistatic geometry. The notations for range and velocity are defined in the manner similar to its bistatic counterpart.

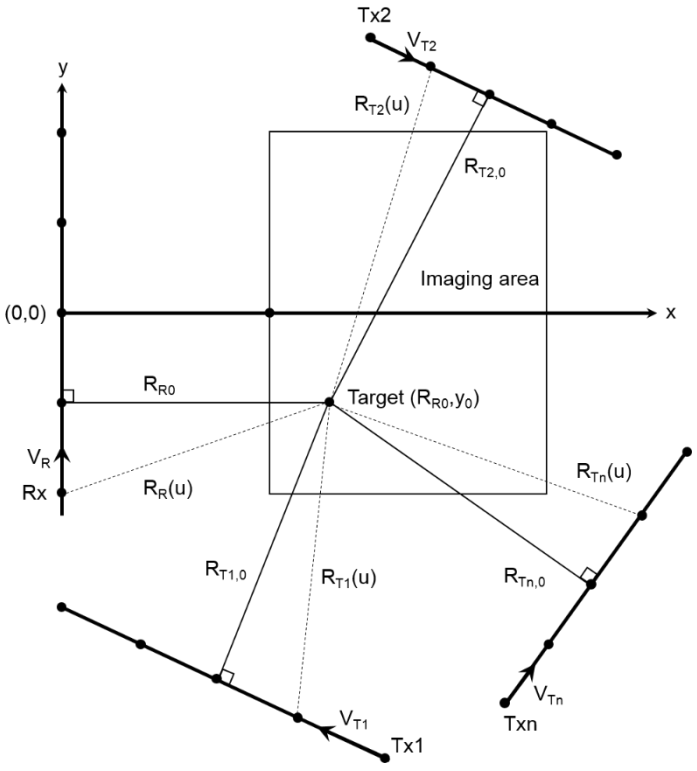

Figure 2.8 General multistatic SAR imaging geometry

Several publications were contributed to investigate multistatic SAR spatial resolution using generalised ambiguity function (GAF). The multistatic GAF (MGAF) can be derived either analytically [36] and numerically [35]. So far, the multistatic GAF is evaluated non-coherently using

$$MGAF(A,B) = \frac{1}{N}\sum_{n=1}^{N} p\left(\frac{2cos(\beta_n/2)\Theta_n^T(r)}{c}\right) \cdot m_A\left(\frac{2\omega_{E_n}\Xi_n^T(r)}{\lambda}\right), \tag{2.67}$$

where $p(\cdot)$ is a matched filter output of a ranging signal and $m_A(\cdot)$ is an inverse transform of the output of normalised received signal magnitude pattern. Subscript n denotes n^{th} bistatic pair and N is the total number of bistatic pairs. A and B are vector positions of the desired point to be evaluated and arbitrary point in the vicinity of A, respectively, and $r = B - A$, β is a bistatic angle, and Θ is a unit vector in the direction of its bisector ($\mathrm{U}_T + \mathrm{U}_R$), $\omega_E = \frac{|\omega_T + \omega_R|}{2}$ and Ξ are monostatic SAR equivalent angular speed and motion direction (or unit vector in the direction of $\omega_T + \omega_R$), c is a speed of light, λ is a wavelength. A superscript, T, denotes the transpose of the matrix. However, a coherent approach to theoretically evaluate MGAF has not been published yet.

2.15 Range Compression

Range compression is used for correlating received radar signal with a range reference signal at each azimuth point. Define $S_0(f_\tau, u)$ as the Fourier transform of the received signal $s_0(\tau, u)$, and frequency domain matched filter as $G(f_\tau)$. Thus, the output of the range matched filter can be expressed as

$$s_{rc}(\tau, u) = \mathrm{IFFT}\{S_0(f_\tau, u)G(f_\tau)\} = \tag{2.68}$$

$$A_0 p_r\left(\tau - \frac{2R(u)}{c}\right)\omega_a(u-u_c)e0^{-\frac{j4\pi f_0 R(u)}{c}},$$

where p_r is compress pulse envelope, A_0 is the overall gain.

2.16 Backprojection Algorithm

BPA was used initially in Computer-aided Tomography (CAT) for medical imaging, [60]. For using BPA in SAR, it was used in monostatic spotlight SAR, [61] and later in the bistatic spotlight and stripmap configuration, [62].

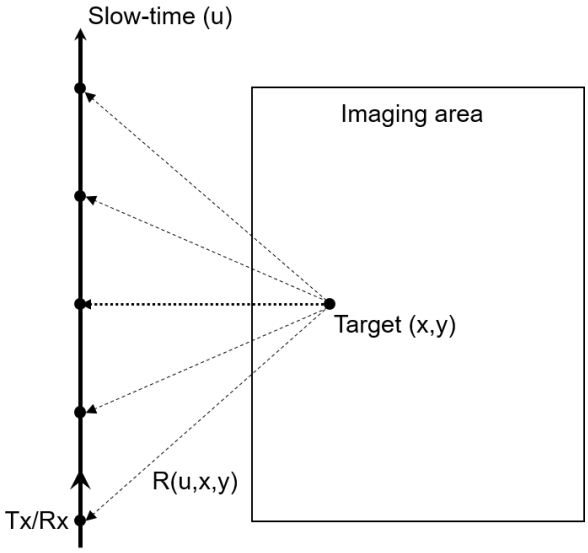

Figure 2.9 Image formation using BPA

From Figure 2.9, let the transmitted signal defined as $s(t,u)$ where t is fast time and u is slow time. The received signal from an arbitrary point can be expressed as $p[t - R(u,x,y)/c]$ where $R(u,x,y)/c$ is a round trip distance between the radar (Tx/Rx) and the target.

Let the $f(x,y)$ is an output image pixel at (x,y) and is defined as

$$f(x,y) = \int_u \int_t s(t,u)\, p^* \left[t - \frac{R(u,x,y)}{c} \right] dtdu. \tag{2.69}$$

If range compression is defined as $s_{rc}(t,u) = s(t,u) \otimes p^*(-t)$ and substituting it to Eq. 2.69 gives

$$f(x,y) = \int_u s_{rc} \left[\frac{R(u,x,y)}{c}, u \right] du = \int_u s_{rc}[t_n(u), u] du, \tag{2.70}$$

where $t_n(u)$ is a round trip delay of the radar return from the target at (x, y).

2.17 Summary

This chapter has briefly explained the fundamentals of radar and SAR. The radar range equation is a relationship between the power of signal transferred within the radar components. This is a fundamental equation to analyse the performance of the radar system at a given stage. At a basic level, the radar system comprises a transmitter, a receiver, and a target. The radar equation is a tool to determine performance, e.g. received power or detectable range, in the radar system.

SAR is a sub-class of radar systems used for imaging the Earth's surface. It simulates a long antenna to enable high azimuth resolution although small physical antenna is used. Its imaging geometry can be categorised as monostatic, bistatic, and multistatic SAR based on location as well as numbers of transmitter and receiver. Spatial resolution is a parameter to characterise SAR performance. For range resolution, it depends on the bandwidth of a transmitted signal in monostatic case, but a bistatic angle is also included in the bistatic case. For azimuth resolution, the key factor is a length of synthetic aperture, which can be decomposed into a product of a platform velocity and dwell time on target.

Since the GNSS-based SAR system is based on a bistatic SAR system, understanding radar and SAR fundamentals are essential for analysing the performance of the system (e.g. power budget and spatial resolution).

Chapter 3

GNSS-based SAR

3.1 Introduction

Space-surface (SS) bistatic SAR (BSAR) is a sub-class of BSAR that use a spaceborne transmitter and a receiver on or near the Earth's surface. This concept with non-cooperative spaceborne illuminators (e.g. communications, broadcasters or navigation) has been proposed and investigated for nearly two decades [63-65]. The SS-BSAR that use signals emitted from Global Navigation Satellites System (GNSS) is referred to as GNSS-based SAR. In the GNSS-based SAR system, a receiver can be mounted stationary on the ground, onboard an aircraft, or on the ground moving vehicle. The GNSS-based SAR with a single transmitter and a single receiver has been developed at both theoretical and experimental levels at the Microwave Integrated Systems Laboratory (MISL), the University of Birmingham for many years [11-19] and the study covers both fixed and moving receiver configurations, (e.g. [13, 16]).

Due to a multitude of GNSS satellites, the GNSS-based SAR system can be extended to the natural of GNSS constellations that are operating in multistatic configuration. The system can be extended to a multistatic operation without any changes to its a bistatic operation since a multistatic operation is considered as a combination of bistatic operations. In this manner, a multistatic imagery can be formed by combining bistatic imageries obtained from

individual bistatic pairs (a single satellite and a single receiver case). As a result, understanding the operation of GNSS-based SAR with a single satellite and a single receiver is essential for the main study in this thesis.

In this chapter, the scientific and engineering aspects of the GNSS-based SAR are reviewed. The chapter covers all aspects of the system ranging from the transmitter to the imagery. For the transmitter part, GNSS constellations are described as their characteristics. Their transmitted signals are then analysed in term of power budget from transmitting off the satellites until it has been processed into bistatic imagery. The system is analysed its performance, in term of spatial resolution. Two signal processing algorithms that threat received signals from maintaining coherence until generating bistatic imagery are also detailed. The former algorithm is a synchronisation algorithm, whilst the latter is an image formation algorithm.

3.2 GNSS Satellites and Signals

Currently, GNSS comprises four major constellations, which are Global Positioning System (GPS), GLONASS, Galileo and BeiDou. All GNSS constellations orbit in Medium Earth Orbit (MEO). Also, BeiDou has another five satellites in Geosynchronous Equatorial Orbit (GEO). GPS, [66], is a space-based radio navigation system owned by the United States Government (USG) and operated by the United States Space Force (USSF). GPS has provided positioning, navigation, and timing services to military and civilian users on a continuous worldwide basis in any weather, day or night, anywhere in the world. GLONASS, [67], is a navigation system owned by the Russian Federation Government and used for providing positioning, navigation and timing services to air, marine, land and space users on a continuous worldwide basis at any point on the Earth’s surface and the near-Earth

space. Galileo, [68], is the European global navigation satellite system providing a highly accurate and global positioning service under civilian control. BeiDou, [69], has been independently developed and operated by China on the needs of the national security of China as well as its economic and social development. BeiDou provides all-time, all-weather and high-accuracy positioning, navigation and timing services to global users.

Table 3.1 shows the details of the GNSS constellation structures. In each constellation, it comprises three orbital planes, except GPS with six orbital planes, where the number of satellites ranging from 4-10 satellites are allocated into each plane. As a result, in full operation, each constellation has more than 25 satellites or more than 100 satellites in total. The geometries of the GNSS constellations are shown in Figure 3.1. The orbital plane inclination is the angle between the orbital plane and the plane of reference, which generally expressed in degree. In GNSS case the reference plane is equatorial plane due to their small semi-major axes of the orbital plane. Satellite revisit period is the time elapsed between observations of the same point on earth by a satellite, expressed in terms of the sidereal day. A sidereal day is approximately 23 hours, 56 minutes, 4.0905 seconds.

Figure 3.2 shows the frequency spectrum band of the GNSS signals. It can be seen that the frequencies occupied by any single GNSS signal are between approximately 4-40 MHz. For example, Galileo E5a has a bandwidth of 25 MHZ, while GLONASS G1 has a bandwidth of 17 MHz.

Table 3.1 GNSS constellations structures and characteristics

Constellation	Number of Planes	Plane Inclination	Altitude (km)	Number of Satellites	Orbital Period (hh:mm:ss)	Revisit Time (sidereal day)
GPS	6	55°	20200	24	11:58:02	1
Galileo	3	56°	23222	30	14:04:45	10
GLONASS	3	64.8°	19100	24	11:15:44	8
BeiDou	3	55°	21528	27	12:53:00	7

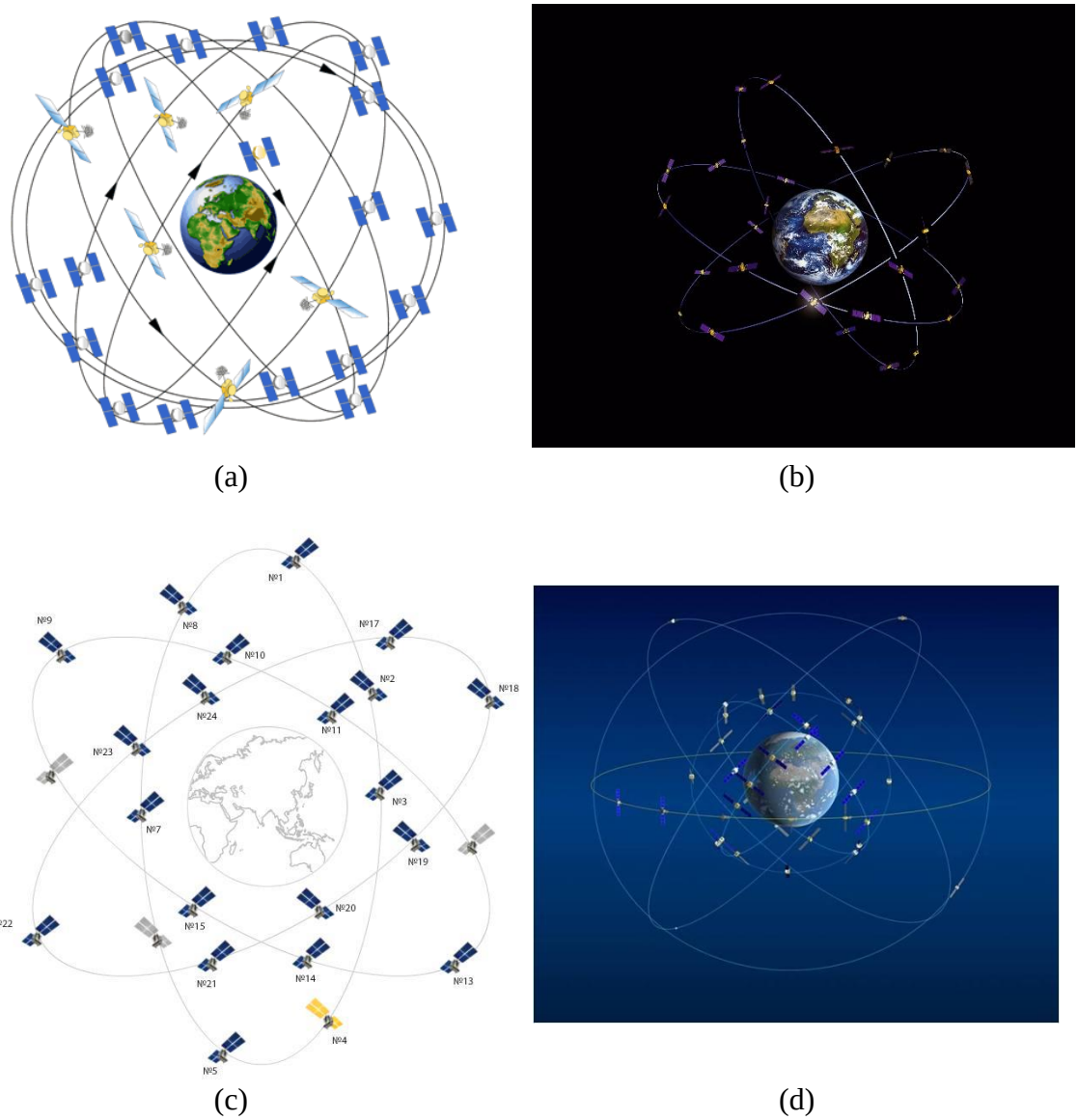

Figure 3.1 Geometries of GNSS constellations (a) GPS (b) Galileo (c) GLONASS (d) Beidou
(source: https://gssc.esa.int/navipedia/images)

Table 3.2 shows the details of examples of the GNSS signals used in GNSS-based SAR. In GNSS-based SAR, a signal that used for imaging is a primary code which is embedded in the GNSS signals. Therefore, knowledge of a primary code structure is essential in extracting it from the transmitted signals.

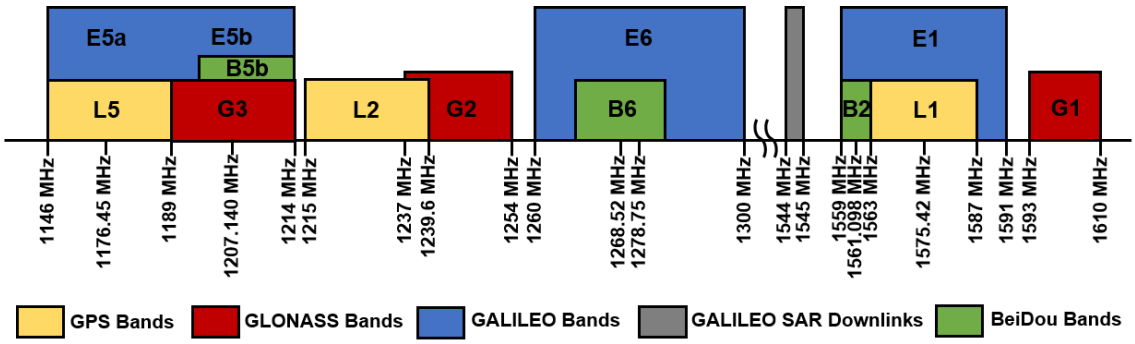

Figure 3.2 Frequency spectrum band of GNSS signals, (adapted from [70])

Table 3.2 Example of signals and their structure that used in GNSS-based SAR

Satellite	Signal	Modulation Type	Carrier Frequency (MHz)	Primary Code Rate (Mchips/s)
Galileo	E5a	BPSK	1176.450	10.23
Galileo	E5b	BPSK	1207.140	10.23
GLONASS	G1	BPSK	1602.0000+ 0.5625k	0.511 (C/A code) 5.11 (P code)
GLONASS	G2	BPSK	1246.0000+0.4375k	0.511 (C/A code) 5.11 (P code)

3.3 GNSS Signals Description

In general, A GNSS signal consists of a primary and a secondary ranging codes, and a navigation message. Primary and secondary codes are pseudo-random sequences whilst a navigation message is a binary phase-shift keying (BPSK) signal. Some signal does not contain a navigation message, e.g. E5a/b-Q of Galileo satellites. A generic form of a signal transmitted from GNSS satellite, [13], is expressed as

$$Y(t) = P(t)M_P(t)cos(\omega_c t + \varphi) + D(t)M_D(t)sin(\omega_c t + \varphi), \tag{3.1}$$

where t is time, $P(t)$ and $D(t)$ are a primary and a secondary ranging code envelope, $M_P(t)$ and $M_D(t)$ are a navigation message, ω_c is the carrier frequency, and φ is an initial phase. $P(t)$ and $D(t)$ are the pseudo-random sequences and generally modulating a navigation message.

A direct received signal after quadrature demodulation and SAR data formatting into fast-time and slow-time axes, it can be expressed, [13], as

$$\begin{aligned} s(t_n, u) = {} & P\big(t_n - \tau_{dP}(u)\big)M_P\big(t_n - \tau_{dP}(u)\big)exp\big[j\big(\omega_d(u)t_n + \varphi_{dP}(u)\big)\big] + \\ & jD\big(t_n - \tau_{dD}(u)\big)M_D\big(t_n - \tau_{dD}(u)\big)exp\big[j\big(\omega_d(u)t_n + \varphi_{dD}(u)\big)\big], \end{aligned} \tag{3.2}$$

where $t_n \in [0,\text{PRI}]$ is a fast time and PRI is a pulse repetition interval, $u \in [-T/2, T/2]$ is a slow time and T is the dwell time on target. $\tau_{dP/D}(u)$, $\omega_d(u)$, and $\varphi_{dP/D}(u)$ are instantaneous time delay, Doppler and initial phase associated with each code of a direct signal, respectively. These parameters are varied with slow time and can be tracked using the synchronisation algorithm.

3.4 Spatial Resolution

Spatial resolution is an ability to resolve or separate two or more target. In bistatic SAR (BSAR), spatial resolution can be analysed using generalised ambiguity function (GAF) (in the form of a single bistatic pair of Eq. 2.67 and see section 3.5 for its derivation). This approach can be applied for analysing the GNSS-based SAR since it is a subclass of BSAR. Figure 3.3 shown general bistatic imaging geometry where the transmitter is a satellite, and a receiver is an aircraft.

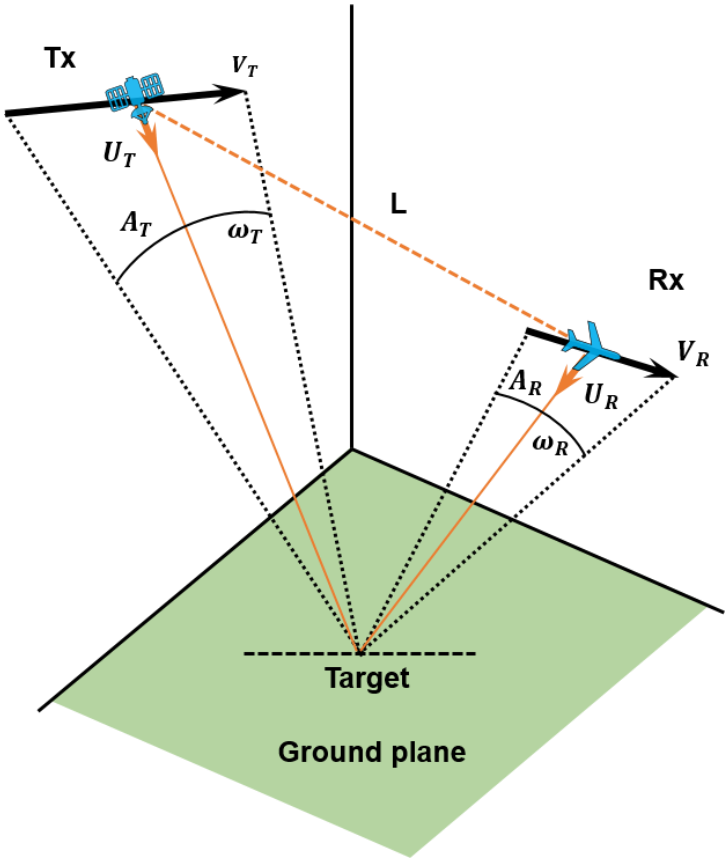

Figure 3.3 General bistatic SAR geometry, (adapted from [15])

From Figure 3.3, L denotes a bistatic base line which is a range between a transmitter and a receiver. Parameters V_T, ω_T, and A_T are velocity, angular speed and total angular movement of a transmitter, respectively, and V_R, ω_R, and A_R are similar parameters for a receiver.

Parameters U_T and U_R are the unit vectors of a transmitter and a receiver to a target at T_{gt}, respectively. From Figure 3.4, Range resolution δ_r is in the direction of U which is defined as a bisector. While azimuth resolution δ_a is in the direction of ω which is defined as $\omega_T + \omega_R$. Basic plane is spanned by U and ω.

For practical consideration, resolution parameters are projected onto the ground plane. δ_r is projected onto the ground using angle φ, and yields ground range as δ_{rg} while δ_a is projected onto the ground using θ. In BSAR range and azimuth are not necessary, and in this case, they are separated by angle α. In a ground plane, cross-range resolution δ_{cr} is introduced for simplicity of analysis.

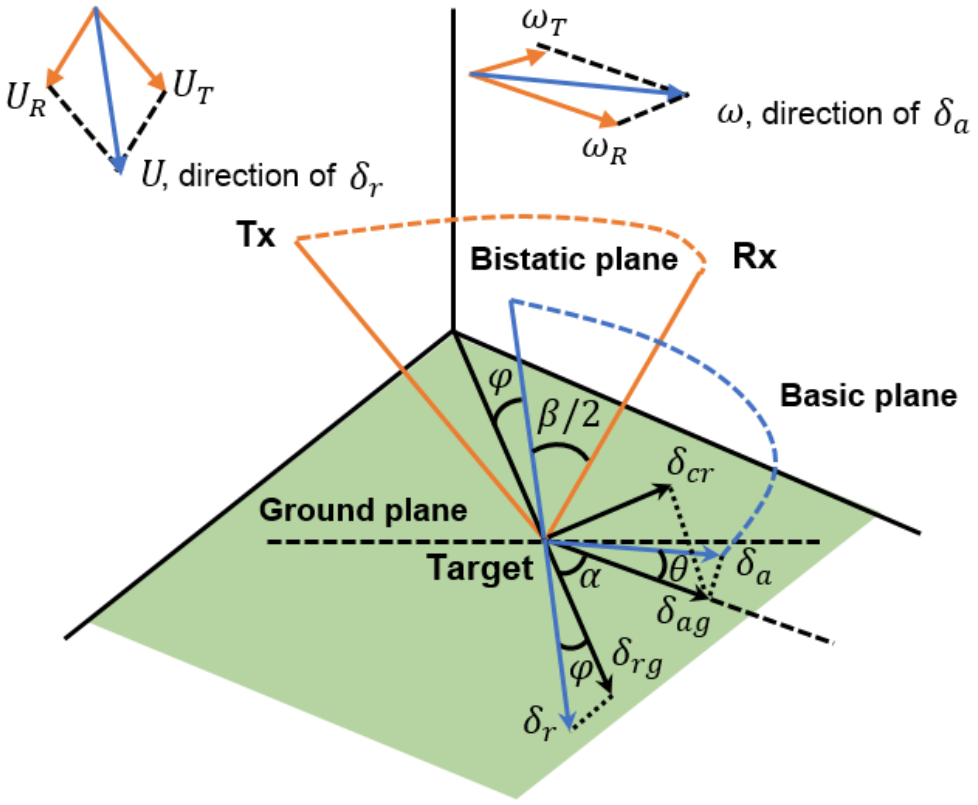

Figure 3.4 Bistatic geometry parameters projection onto ground plane, (adapted from [15])

3.5 Point Spread Function

The point spread function (PSF) of an imaging system, as defined in [71], is the system response to a point target. It is the impulse response of an imaging system to a point object and used for expressing the imaging performance. In the general case, PSF is defined as

$$I(x,y) = \iint O(u,v)h(x-u,y-v)\,dudv, \tag{3.3}$$

where $O(u,v)$ is an object function, $I(x,y)$ represents the resulting reconstructed image of the object, and $h(x,y)$ is the PSF of the imaging system representing the linear mapping of

the object to the image. The quality of an imaging system can be represented in terms of the degree of spreading of the point object.

PSF is related to the many parameters which are transmitted signal waveform, transmitting and receiving antenna patterns, object properties, and image formation processing. The ambiguity function is determined only by signal waveforms without accounting for other factors. Therefore, in radar imaging systems the ambiguity function of the radar signal waveform is not precisely the PSF of the system but is a weighted sum of ambiguity functions

3.6 BSAR Generalised Ambiguity Function

The Generalised ambiguity function for BSAR has been derived in [34]. This section briefly reiterates that derivation.

The SS-BSAR topology is shown in Figure 3.5. The topology is represented in Cartesian (x-y-z) coordinate system.

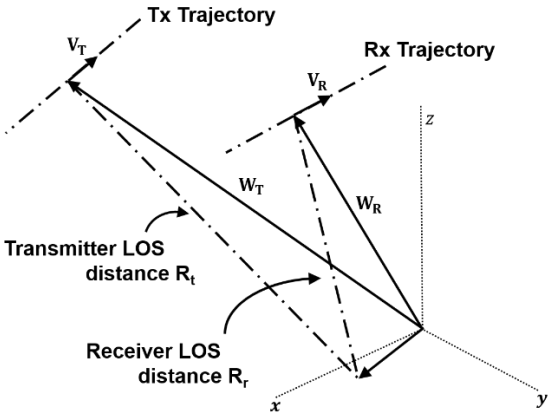

Figure 3.5 SS-BSAR topology, (adapted from [15])

Figure 3.5 W_T and V_T are the respective vector of the transmitter position and velocity, W_R and V_R are the respective vector of the receiver position and velocity, A is the vector of the target in the observation area, R_{TA} and R_{RA} defines the respective range between the target A and transmitter, and between the target A and the receiver.

The time difference between transmitting and receiving signal is defined as

$$\tau_A(u) = \frac{R_{TA} + R_{RA}}{c}. \tag{3.4}$$

Using the radar equation (Eq. 2.1) to compute the ratio of received to transmitted power (M_A) and it gives

$$M_A(u) = \frac{P_r}{P_t} = \frac{G_t G_r \lambda^2 \sigma}{(4\pi)^3 R_{TA}^2 R_{RA}^2}. \tag{3.5}$$

The received signal reflected from target A can be expressed as

$$h_A(t,u) = \sqrt{M_A(u)}s(t - \tau_A(u))e^{j2\pi f_0[t-\tau_A(u)]}. \tag{3.6}$$

Next, the correlation between signal return from target A and the reference target B then is computed as

$$\chi(A,B) = \iint \frac{h_A(t,u)h_B^*(t,u)}{\sqrt{\iint |h_B(t,u)|^2 dtdu}\sqrt{\iint |h_B(t,u)|^2 dtdu}} dtdu = \tag{3.7}$$

$$\iint \frac{\sqrt{M_A(u)}\sqrt{M_B(u)}s(t-\tau_A(u))s^*(t-\tau_B(u))e^{j2\pi f_0[\tau_B(u)-\tau_A(u)]}}{\sqrt{\iint M_A(u)|s(t-\tau_A(u))|^2 dtdu}\sqrt{\iint M_B(u)|s(t-\tau_B(u))|^2 dtdu}} dtdu.$$

Transforming Eq. 3.7 into the frequency domain using Parseval's theorem yields the correlation function as

$$\chi(A,B) = \iint \frac{h_A(t,u)h_B^*(t,u)}{\sqrt{\iint |h_B(t,u)|^2 dtdu}\sqrt{\iint |h_B(t,u)|^2 dtdt}} dtdu = \tag{3.8}$$

$$\iint \frac{P(f)e^{j2\pi f[\tau_B(u)-\tau_A(u)]}df\sqrt{M_A(u)M_B(u)}e^{j2\pi f_0[\tau_B(u)-\tau_A(u)]}du}{\sqrt{\int P(f)df \int M_A(u)du}\sqrt{\int P(f)df \int M_B(u)du}}.$$

Equation 3.8 can be simplified using the assumptions that

1) the antenna gain in the directions to both targets are approximately the same due to the two targets are located close to each other. In such a case, the power returned from both targets are approximately equal, and
2) the length of the synthetic aperture is much smaller than the ranges to the target. In such case, the difference of total propagation path lengths can be neglected, and
3) the ranging signal is narrowband so that the phase term $2\pi f[\tau_B(u) - \tau_A(u)] \approx 2\pi\tau_D$.

The assumptions above yield that

$$\chi(A,B) = e^{j2\pi f_0 \Delta\tau(u_A)} \frac{\int P(f) e^{j2\pi f \Delta\tau(u_A)} df}{\int P(f) df} \tag{3.9}$$

$$\times \frac{\int M_A(u) e^{2\pi(u-u_A)\Delta f_d(u_A)} du}{\int M_A(u) du}.$$

Changing the variable u gives

$$\bar{P}(f) = \frac{P(f)}{\int P(f) df}, \tag{3.10}$$

$$\overline{M_A}(u) = \frac{M_A(u+u_A)}{\int M_A(u+u_A) du}. \tag{3.11}$$

Substituting Eq. 3.10 and 3.11 to Eq. 3.9 yields the simplified correlation function (compared to Eq. 3.8) as

$$\chi(A,B) = e^{j2\pi f_0 \Delta\tau(u_A)} \int_{-\infty}^{\infty} \bar{P}(f) e^{2\pi f \Delta\tau(u_A)} df \int_{-\infty}^{\infty} \overline{M_A}(u) e^{j2\pi \Delta f_d u} du. \tag{3.12}$$

Transforming $\bar{P}(f)$ to $p(\Delta\tau)$ and $\overline{M_A}(u)$ to $m_A(\Delta f_d)$ gives the ambiguity function for SS-BSAR as

$$\chi(A,B) = e^{j2\pi f_0 \Delta\tau} p(\Delta\tau) m_A(\Delta f_d). \tag{3.13}$$

where $p(\cdot)$ is the inverse transform of the signal power spectrum (i.e., the autocorrelation function), and $m_A(\cdot)$ is the inverse transform of the normalised signal magnitude pattern across the receiving array (i.e., the ratio of received to transmitted power). The former parameter describes range resolution while the latter specifies the Doppler-based resolution.

The ambiguity function in Eq. 3.13 can also be expressed in terms of spatial coordination through suitable approximation. The vectors used in the approximation are shown in Fig. 3.6.

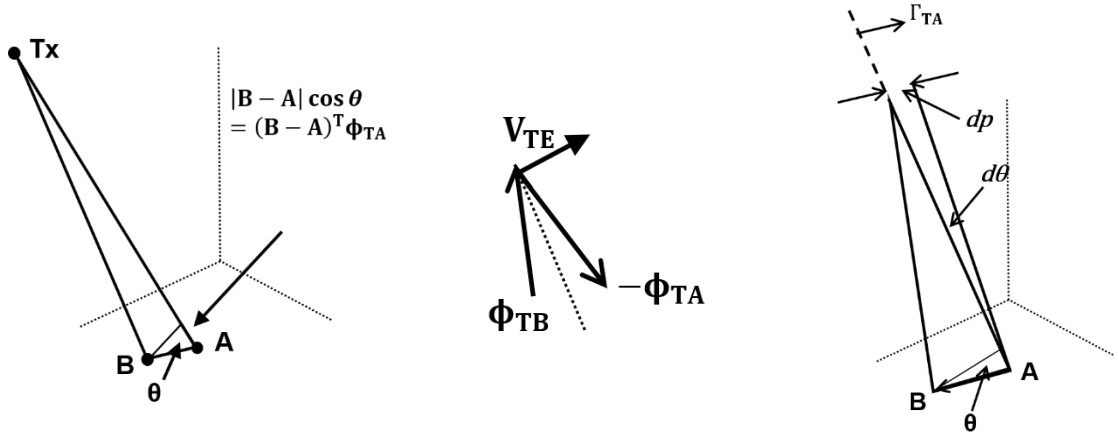

(a) (b) (c)

Figure 3.6 Vector position, (adapted from [15])

Figure 3.6 (a) illustrates the vectors which are used for approximating the total delay difference. Vector $(B-A)$ is the target separation while Φ_{TA} is unit vector of the transmitter-to-target direction. The path length difference is defined as $(B-A)^T\Phi_{TA}$. The same approach is applied to the direction of receiver-to-target (Φ_{RA}). Therefore, combining these two results leads to the approximated total delay difference at the time u_A as

$$\Delta\tau(u_A) \approx \frac{1}{c}(B-A)^T[\Phi_{TA}+\Phi_{RA}]. \tag{3.14}$$

The vectors used for approximating the Doppler difference is illustrated in Figure 3.6 (b). Vector V_{TE} is the transmitter velocity that is projected to the direction perpendicular to a bisector line of the two unit vectors, Φ_{TA} and Φ_{TB}. It is used for determining Doppler difference as

$$\dot{R}_{TB} - \dot{R}_{TA} = V_{TE}[\Phi_{TB} - \Phi_{TA}], \tag{3.15}$$

where $\dot{R}_{TA}$ and $\dot{R}_{TB}$ are the respective rate of change of path length to point A and B. If the separation between A and B is small, the direction of the velocity vector V_{TE} can also be approximated as the unit vector Γ_{TA} that perpendicular to Φ_{TA} (see Figure 3.6 (c)). Figure 3.6 (c) also shows that a small separation in position (dp) caused by Γ_{TA} will cause the angular changes by $d\theta$. As a result, the path difference in Figure 3.6 (a) is changed to $(B - A)\cos(\theta + d\theta)$. Using trigonometric identity and approximation that $\cos(d\theta) \approx 1$ and $\sin(d\theta) \approx d\theta$, Eq. 3.15 gives the rate of change of path difference as $(B - A)^T \Gamma_{TA} \omega_{TA}$, where ω_{TA} is the rotation rate of the transmitter about point A. The same approach is also applied to the path from A to B and the receiver. Both results then yield the Doppler difference as

$$\Delta f_d(u_A) \approx \frac{1}{\lambda}[\omega_{TA}\Gamma_{TA} + \omega_{RA}\Gamma_{RA}](B - A). \tag{3.16}$$

Substituting Eq. 3.14 and 3.16 to 3.13 leads to

$$\chi(A, B) \approx e^{j2\pi\frac{1}{\lambda}[\Phi_{TA}+\Phi_{RA}]^T(B-A)} \times p\left\{\frac{1}{c}[\Phi_{TA} + \Phi_{RA}]^T(B - A)\right\} \tag{3.17}$$

$$\times m_A\left\{\frac{1}{\lambda}[\omega_{TA}\Gamma_{TA} + \omega_{RA}\Gamma_{RA}]^T(B - A)\right\}.$$

From Eq. 3.17, the vector $\Phi_{TA} + \Phi_{RA}$ is a bisector of the bistatic angle of β. Defining Θ as a unit vector in the bisector direction gives

$$\Phi_{TA} + \Phi_{RA} = 2\cos(\beta/2)\,\Theta. \tag{3.18}$$

Also, from Eq. 3.17, the vector $\omega_{TA}\Gamma_{TA} + \omega_{RA}\Gamma_{RA}$ is in the direction between the rotation and angular speed of the transmitter and the receiver. Defining Ξ as a unit vector in this direction and $\omega_E = \frac{|\omega_T+\omega_R|}{2}$ give

$$\omega_{TA}\Gamma_{TA} + \omega_{RA}\Gamma_{RA} = 2\omega_E\Xi. \tag{3.19}$$

Please note that in the original derivation [15, 34], ω_E and Ξ are respectively referred to as the equivalent angular speed and the equivalent motion direction. This is due to that azimuth resolution performance of the monostatic SAR will be equivalent to the bistatic SAR if the monostatic platform is moving in the direction of Ξ with the angular speed ω_E. The vectors Θ and Ξ span a basic plane which is the plane defining range and azimuth resolutions and has a similar impact to a slant plane in the monostatic SAR.

Substituting Eq.3.18 and 3.19 to 3.17 gives

$$\chi(A,B) \approx e^{j2\pi\frac{1}{\lambda}[\Phi_{TA}+\Phi_{RA}]^T(B-A)} \times p\left\{\frac{1}{c}2\cos(\beta/2)\,\Theta^T(B-A)\right\} \tag{3.20}$$

$$\times\, m_A\left\{\frac{1}{\lambda}2\omega_E\Xi^T(B-A)\right\}.$$

Determining resolution performance is performed by taking the magnitude of the GAF as

$$|X(A,B)| \approx \left|p\left[\frac{2cos(\beta/2)\Theta^{\mathrm{T}}(r)}{c}\right]\cdot m_A\left[\frac{2\omega_E\Xi^{\mathrm{T}}(r)}{\lambda}\right]\right|, \tag{3.21}$$

Range and azimuth resolutions (δ_r and δ_a respectively) are determined at -3 dB width of GAF using

$$\delta_r = \frac{\delta_\tau c}{2cos(\beta/2)} = \frac{c}{2Bcos(\beta/2)}, \tag{3.22}$$

$$\delta_a = \frac{\delta_D \lambda}{2\omega_E} = \frac{\lambda}{2T_c\omega_E}. \tag{3.23}$$

where δ_τ and δ_D are the delay and Doppler resolutions, respectively. Derivation of these equations can be found in [34]. Since in bistatic configuration, range and azimuth resolution are not necessarily orthogonal. Therefore, cross-range resolution (δ_c) was defined by

$$\delta_c = \frac{\delta_a}{sin\alpha}, \tag{3.24}$$

where α is the angle between vector Θ and Ξ.

From Eq. 3.22, range resolution depends on the bistatic geometry, and the bandwidth of transmitting signal and the optimum value can be achieved under quasi-monostatic geometry (β is nearly zero). For example, assuming a Galileo satellite is used, its primary code has 10.23 MHz of bandwidth. This bandwidth yields range resolution of 15 m under quasi-monostatic geometry and are further degraded as a bistatic angle increases.

According to Eq. 3.23, in most cases of GNSS-based SAR, a transmitter is at high altitude whilst a receiver is at low altitude; hence a receiver dominates azimuth resolution since the angular speed of a receiver is larger than those of a transmitter. If a geostationary satellite is used, a transmitter's angular speed can be negligible respect to a ground target. In this case, the synthetic aperture depends on a receiver motion solely and can be determined by

$$\delta_a = \frac{\lambda R_R}{L_c} = \frac{\lambda R_R}{V_R T_c}, \tag{3.25}$$

where L_c is a length of synthetic aperture and V_R is a receiver velocity. Similarly, for a fixed receiver case, a synthetic aperture is based on the motion of a satellite. An azimuth resolution can be determined by

$$\delta_a = \frac{\lambda R_T}{V_T T_c}, \tag{3.26}$$

V_T is a satellite velocity. In practical, projecting onto the ground plane enables spatial resolution more meaningful and better perception. They can be determined by

$$\delta_{rg} = \frac{\delta_r}{cos\varphi} = \frac{c}{2Bcos(\beta/2)cos\varphi}, \tag{3.27}$$

$$\delta_{ag} = \frac{\delta_a}{cos\theta} = \frac{\lambda}{2T_c\omega_E cos\theta}, \tag{3.28}$$

where φ and θ are the angles between range and azimuth directions and ground plane, respectively. Equation 3.27 and 3.28 show that resolutions are further degraded when project onto the ground by the cosine term.

The GNSS-based SAR requires long dwell time (5-10 minutes) on target to obtain sufficiently azimuth resolution (less than 3 m), [17]. This can be explained using Eq. 3.23, which shows that increasing dwell time can improve azimuth resolution. In such long dwell time, satellite's trajectory cannot be approximated as a straight line. The extended GAF, [17], was derived for curved trajectory as

$$|X(A,B)| \approx c\left|\int p\left[\frac{f_{dc}}{f_c}\cdot(\bar{u})\right]\cdot\widetilde{M}_A(\bar{u})exp(j2\pi f_{dc}\bar{u} + j\pi f_{dr}\bar{u}^2)d\bar{u}\right|, \tag{3.29}$$

where $\bar{u} = u - u_C$, u_C is a midpoint of a synthetic aperture, f_c is the carrier frequency of the transmitted signal, f_{dc} is Doppler centroid difference between two scatters (A and B), and f_{dr} is Doppler chip rate difference. The f_{dc} and f_{dr} can be computed by

$$f_{dc} = \frac{1}{\lambda}(U_{TB} - U_{TA})^{\mathrm{T}} V_T, \tag{3.30}$$

$$f_{dr} = \frac{1}{\lambda}\left\{(U_{TB} - U_{TA})^{\mathrm{T}} a_T + V_T^{\mathrm{T}}\left[\frac{I_{3\times3} - U_{TB}^{\mathrm{T}} U_{TB}}{|B - R_T(u_C)|} - \frac{I_{3\times3} - U_{TA}^{\mathrm{T}} U_{TA}}{|A - R_T(u_C)|}\right] V_T\right\}, \tag{3.31}$$

where I is an identity matrix and a_T is an acceleration vector. In [17], the extended GAF (Eq. 3.31) were demonstrated that it could estimate point spread function for a case of long dwell time on target more precisely than the GAF using Eq. 3.21.

3.7 Power Budget

Power budget of GNSS-based SAR considers entire the chain of power transmission from a satellite until a receiver. This analysis can be separate into two parts: transmitter power parameters and a receiver power parameter. Transmitter power parameters are the power transmitted by a satellite and a power near a receiver or a target area. A receiver power parameter is calculated in term of signal-to-noise ratio (SNR) of radar channel.

In the communication system, the amount of emitted power from a transmitter is expressed as Equivalent Isotropically Radiated Power (EIRP). The EIRP is a product of transmitter power (P_T), an antenna gain (G_a) in a given direction relative to an isotropic antenna, and losses in the transmission line (L_f). It can be written as

$$EIRP = P_T - L_f + G_a. \tag{3.32}$$

EIRP of three GNSS constellation is shown in Table 3.3.

Table 3.3 Transmitter power budget parameters, calculated by [70]

GNSS Constellation	Power Output (W)	EIRP (dBW)	Orbit Altitude (km)	Power Density (dBW/m^2)
Galileo	50	32	23222	-126
GPS	50	30	20180	-127
GLONASS	50	28	19130	-128

From Table 3.3, Power parameters on this table are based on free-space propagation with a global beam. All GNSS constellations have the same power output.

For a receiver part, the system SNR, which was derived in [72], after range and azimuth compression, and spatial resolution are determined and can be written as

$$\frac{S}{N} = \frac{EIRP}{4\pi R_T^2} \cdot \frac{A_r \sigma}{4\pi R_R^2} \cdot \frac{1}{KT_0 BF} \cdot \frac{\tau_i}{\tau_0} \cdot \frac{PRF \cdot R \cdot \lambda}{V \delta_a} \cdot \eta, \tag{3.33}$$

where $\frac{EIRP}{4\pi R_T^2}$ is a power flux density near the Earth's surface generated by a GNSS satellite, τ_i and τ_o are the signal durations of compressed and the uncompressed ranging signal, and (τ_i/τ_o) is an SNR after range compression. The term $\frac{PRF \cdot R \cdot \lambda}{V \delta_a}$ is a number of integrated signals during dwell time on target and also an SNR after azimuth compression. If assuming system loss factor is $\eta \approx 0.1$ and a receiver's system noise bandwidth and a transmitting signal bandwidth are matched so that $B \cdot \tau_0 = 1$. For the airborne receiver, the SNR can be written as

$$\frac{S}{N} = \frac{EIRP}{4\pi R_T^2} \cdot \frac{A_r \sigma}{4\pi R_R} \cdot \frac{t_c}{KT_0 F_n} \cdot \frac{PRF \cdot R \cdot \lambda \eta}{V_a \delta_a}, \tag{3.34}$$

where t_c is a period of transmitting signal and V_a is an aircraft velocity. Examples analysis of an airborne receiver with various RCS is shown in Table 3.4. For the fixed receiver, the SNR is written as

$$\frac{S}{N} = \frac{EIRP}{4\pi R_T^2} \cdot \frac{A_r \sigma}{4\pi R_R^2} \cdot \frac{R_T}{KT_0 F_n} \cdot \frac{\lambda \eta}{V_s \delta_a}. \quad (3.35)$$

Table 3.5 shows the SNR from the system with a fixed receiver.

Table 3.4 Power budget of GNSS-based SAR with an airborne receiver, [72]

RCS (m^2)	Receiver-to-target Distance (km)	Receiver Speed (m/s)	Dwell Time on Target (s)	SNR (dB)
10	3	25 (90 km/h)	30.6	6.17
50	3	25	30.6	13.16
50	6	25	61.2	10.15
50	10	25	102	7.93
50	10	50 (180 km/h)	51	4.92
250	10	25	102	14.92
250	15	50	76.5	10.15

Table 3.5 Power budget of GNSS-based SAR with a fixed receiver, [72]

RCS (m^2)	Receiver-to-target Distance (km)	Satellite Speed (m/s)	Dwell Time on Target (s)	SNR (dB)
1	1	3500	1000	20.86
1	2	3500	1000	14.84
10	3	3500	1000	21.32
10	10	3500	1000	10.86
50	10	3500	1000	17.85
50	30	3500	1000	8.31
250	15	3500	1000	21.32
250	30	3500	1000	15.29

From Table 3.5, SNR from a fixed receiver case is high because of long dwell time on target (more than 15 minutes).

3.8 Signal Synchronisation

As GNSS-based SAR is a passive system, a bistatic geometry is a fundamental element, which can be composed to form a multistatic geometry. A transmitter and a receiver are spatially separated in bistatic geometry. Signal synchronisation is a process that required to recover coherence between transmitted and received signals. Coherence is essential for

image formation. To perform synchronisation, one additional channel (HC), compared to a single channel of radar signal (RC) in a monostatic system, is required and used to capture the direct signal from a satellite. In case that both channels are on the same receiver (as in this study), clocks and local oscillators are shared between them. Therefore, clock slippage and local oscillator drift between a transmitter and a receiver are identical to both channels. As a result, synchronisation parameters which are tracked from a direct signal at an HC can be used to compensate a reflection signal at RC.

In GNSS-base SAR system, primary code is an essential code to define bandwidth for imaging, hence tracked parameters are extracted based on this code whilst secondary code and navigation message can be considered as interference signals. The well-known Block Adjustment Synchronising Signal (BASS), [73], which is used for GNSS signal tracking purposes in navigation was adopted to be used for synchronisation in GNSS-based SAR system. Its block diagram of the adopted algorithm is shown in Figure 3.7. This algorithm is computed based on pulse repetition frequency (PRF).

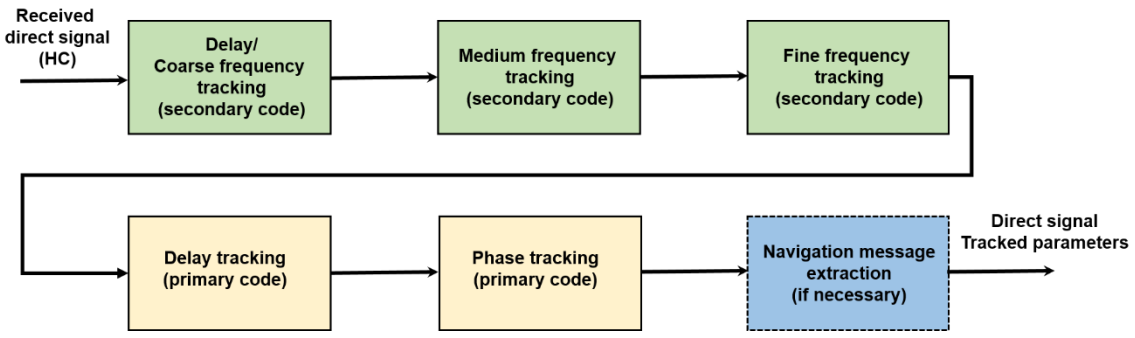

Figure 3.7 Block diagram of the synchronisation algorithm in GNSS-base SAR, (adapted from [13])

From the block diagram in Figure 3.7, the received signal is a direct signal received at HC, which is based on Eq. 3.2. The first three steps are performed on a secondary code to

determine its time delay using three different Doppler frequency resolutions. In the first step, matched-filter banks are used with an envelope of a secondary code as a reference signal. Doppler frequency has a coarse increment of 1 kHz from -20 to 20 kHz, to locate the peak of the signal (estimated time delay). These figures based on pulse repetition interval (PRI) in GNSS-based SAR, which is usually 1 ms (based on a primary code PRI) and yields pulse repetition frequency (PRF) of 1 kHz, and maximum expected Doppler frequency from GNSS satellites is between -20 and 20 kHz, [73]. The output of this step is estimated time delay and coarse Doppler frequency in the order of kHz.

The medium Doppler frequency tracking refines the searching with 200 Hz resolution via the fast Fourier transform (FFT), which is the same technique as in the coarse frequency tracking. In contrast, the phase difference of signals between adjacent PRIs is used for the fine Doppler frequency tracking. This technique, in practical, can track Doppler with an accuracy up to two decimal places, [13]. The output of the fine Doppler frequency tracking is the time delay and Doppler frequency of the secondary code (also is a direct signal Doppler). These parameters are used to remove components of a secondary code from Eq. 3.2. A navigation message of a secondary code (M_D) is not tracked but it has low correlation with a primary code, hence it can be neglected. The remaining signal can be expressed as

$$s(t_n, u) = P\big(t_n - \tau_{dP}(u)\big) M_P\big(t_n - \tau_{dP}(u)\big) exp\big[j\big(\omega_d(u) t_n + \varphi_{dP}(u)\big)\big]. \qquad (3.36)$$

To track for the time delay (τ_{dP}) of a primary code, the matched filter is used with an envelope of a primary code as a reference signal which is shifted by tracked Doppler (ω_d) from the previous step. Doppler frequency from the previous step can be used since it determined from phase difference, which is approximately equal for both codes. Time delay of a primary code obtained from this step is used to obtain phase (φ_{dP}) of a primary code

from a navigation message (M_P) through the phase transition detector. Finally, the tracked parameters from a direct signal, which are time delay (τ_{dP}), Doppler frequency (ω_d), and phase (φ_{dP}), are obtained at the output of the synchronisation algorithm. These parameters are used to generate a reference signal in an image formation algorithm.

3.9 Image Formation

An image formation is an algorithm that used to generate imagery of a target area. This algorithm requires parameters which are tracked from a direct signal by a synchronisation algorithm. Those tracked parameters are essential to maintain coherency for a reflected signal in bistatic SAR image formation. This is one of the factors to be considered when choosing an image formation algorithm. Equally, efficient processing in the frequency domain may or may not be allowed, depends on bistatic geometries as well as bistatic range and Doppler histories. These are particularly true for the GNSS-based SAR case, where there is little control of the GNSS satellite trajectory. A receiver is also a factor, both moving and fixed configurations. A moving receiver requires a motion compensation to be added to an image formation, hence more complex processing. In case of a fixed receiver, despite more straightforward processing, it requires longer dwell time on target for sufficiently high azimuth resolution. As a result, the GNSS trajectory cannot be approximated as a straight line, in this case; thus it is challenging to derive frequency domain algorithms.

A back-projection algorithm (BPA) is a suitable solution for GNSS-based SAR. Although it works in the time domain, hence time-consuming algorithm, its global operation for various configurations of GNSS-based SAR is attractive. The BPA can accommodate all GNSS satellites as well as a different type of receivers, both moving and stationary. Its capability was demonstrated in [13] using a GLONASS satellite with a fixed receiver and a Galileo

satellite with a moving receiver on ground vehicle and aircraft. For BPA, either a moving or a fixed receiver, processing steps are similar. The only difference is motion compensation which is an additional step for a moving receiver case. Block diagram of the BPA with motion compensation is shown in Figure 3.8. When motion error is presented, the moving platform deviates from its nominal trajectory. This deviation could be caused by atmospheric turbulence during the flight in the airborne case or by road anomalies in the ground moving vehicle case. In SS-BSAR, the motion compensation is used for correcting trajectory deviation of the receiving platform only. In contrast, the satellite is assumed to fly in a straight line, which is approximately true for a relatively short observation time.

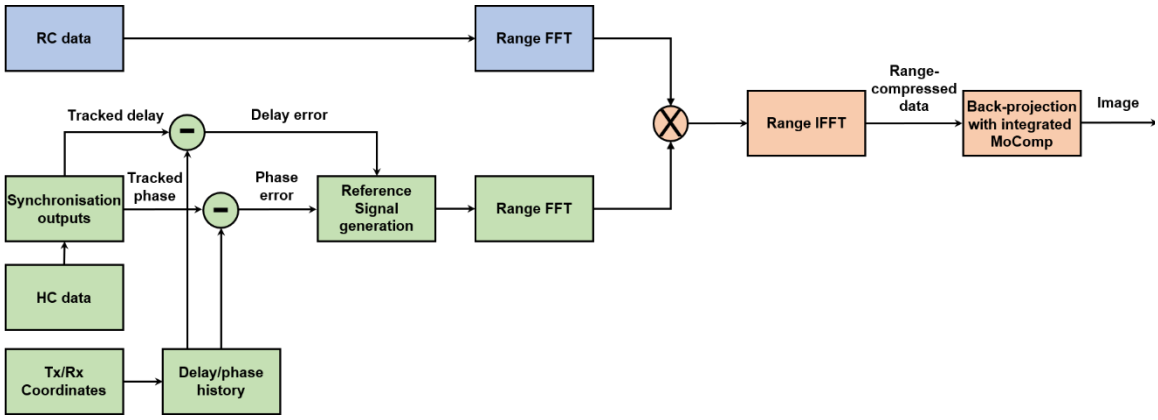

Figure 3.8 Block diagram of BPA for GNSS-base SAR with moving receiver, (adapted from [13])

The BPA comprises two main steps: range compression and back-projection integration. Range compression is a matched filtering between a reference signal and an RC signal. Back-projection integration requires knowledge of a transmitter and receiver positions to determine time delay for each grid point. Assuming a fixed receiver is used, given a satellite is at (x_T, y_T, z_T), a receiver is at (x_R, y_R, z_R), and a point target is at (x_{Ta}, y_{Ta}, z_{Ta}). A transmitter-to-target range, a receiver-to-target range, and a transmitter-to-receiver range can be written respectively as

$$R_T(u) = \sqrt{|x_T(u) - x_{Ta}|^2 + |y_T(u) - y_{Ta}|^2 + |z_T(u) - z_{Ta}|^2}, \tag{3.37}$$

$$R_R(u) = \sqrt{|x_R(u) - x_{Ta}|^2 + |y_R(u) - y_{Ta}|^2 + |z_R(u) - z_{Ta}|^2}, \tag{3.38}$$

$$R_B(u) = \sqrt{|x_T(u) - x_R(u)|^2 + |y_T(u) - y_R(u)|^2 + |z_T(u) - z_R(u)|^2}. \tag{3.39}$$

A reference signal is constructed using the output from the synchronisation algorithm. The time delay and phase do not only relate to radio propagation, baseline range in case of HC or transmitter-target-receiver range in case of RC but also contain errors caused by receiver artefacts and atmospheric propagation. The receiver artefacts may be caused by its hardware, e.g. clock slippage and local oscillator drift. The effect of the atmosphere on radar waves is bending the wave propagation deviate from a straight line. This effect is caused by the variation of the index of reflection.

The received signals at HC and RC (s_{HC}, s_{RC}) with the presence of time delay and phase errors ($t_{error}, \varphi_{error}$), which can be expressed as

$$s_{HC}(t,u) = p\left(t - \left[\frac{R_B(u)}{c} + t_{error}\right]\right) \times exp\left\{-j\left[\frac{2\pi}{\lambda}R_B(u) + \varphi_{error}\right]\right\}, \tag{3.40}$$

$$s_{RC}(t,u) = p\left(t - \left[\frac{R_T(u) + R_R(u)}{c} + t_{error}\right]\right) \tag{3.41}$$

$$\times exp\left\{-j\left[\frac{2\pi}{\lambda}\left(R_T(u) + R_R(u)\right) + \varphi_{error}\right]\right\},$$

where $p(t)$ is a transmitted signal envelope, which is a primary code, in this case, c is the speed of light, and λ is a wavelength. Both received signals can be modelled with the same error because they share common receiver error and approximately equal atmospheric error. As a result, tracked parameters in the HC synchronisation can be used to compensate RC

signal. To remove t_{error} and φ_{error} from the RC signal, a reference signal has to contain only these errors by removing delay and phase terms other than t_{error} and φ_{error} from the HC. Therefore, the delay and phase associated with baseline time ($\frac{R_B(u)}{c}, \frac{2\pi}{\lambda}R_B(u)$) have to be removed from the output parameters of synchronisation. Then the output parameters without radio propagation are used to construct a reference signal. This reference signal can be written as

$$s_0(t,u) = p[t - t_{error}] \times exp[-j(\varphi_{error})]. \tag{3.42}$$

Range compression can be performed using FFT on Eq. 3.40-3.41 and then inverse FFT. The range-compressed RC signal can be expressed as

$$r(t,u) = R_x\left[t - \frac{R_T(u)+R_R(u)}{c}\right] \times exp\left[-j\frac{2\pi}{\lambda}\left(R_T(u) + R_R(u)\right)\right]. \tag{3.43}$$

It can be seen that a time delay and a phase history of the range-compressed signal in Eq. 3.43 are due to a radio propagation solely and free of a receiver and atmospheric errors.

For back-projection integration, a rectangular grid with coordinates (x_i, y_j) is defined corresponding to a target area. At each slow-time point, the range-compressed signal is traced back based on bistatic time delay for every grid point. These data are then integrated over the entire dwell time on target (slow time). This process for each grid point can be expressed as

$$f(x_i, y_j) = \sum_u r\left[t_{i,j}(u), u\right], \tag{3.44}$$

where $r(\cdot)$ is the range-compressed signal and $t_{i,j}(u) = \frac{R_{T_{i,j}}(u)+R_{R_{i,j}}(u)}{c}$ is a bistatic time delay for a target at (x_i, y_j). Equation 3.44 can be approximated as a complex summation as

the slow time is a discrete variable from the stop-and-go assumption of the system. If a moving receiver is used, the motion compensation can be added to each grid point individually. The BPA with motion compensation can be expressed as

$$f(x_i, y_j) = \sum_u r\left[t_{i,j}(u), u\right] exp\left[j\frac{2\pi}{\lambda}\Delta R_{i,j}(u)\right], \tag{3.45}$$

where $\Delta R_{i,j}(u)$ is a phase factor of motion compensation for a target at (x_i, y_j) and $\Delta R_R(u) = R_R(u) - R_{Re}(u)$. In the case of moving receiver, $R_R(u)$ is an error-free receiver-to-target range and $R_{Re}(u)$ is an actual receiver-to-target range with motion errors which can be determined using

$$R_{Re}(u) = \sqrt{|x_{Re}(u) - x_{Ta}|^2 + |y_{Re}(u) - y_{Ta}|^2 + |z_{Re}(u) - z_{Ta}|^2}, \tag{3.46}$$

where (x_{Re}, y_{Re}, z_{Re}) are the actual position of the receiver that contains the motion error.

3.10 Summary

This chapter reviewed theoretical aspects of the GNSS-based SAR for generating bistatic imagery, which is a fundamental element to form a multistatic image. GNSS satellites were used as transmitters due to their availability and multitude. At any time and any point on the Earth's surface, at least 6-8 satellites from a single constellation are visible. Since the satellite is not primarily built for radar or remote sensing applications, the power density near the Earth's surface is uniformly low. From the analysis, it shows that the power budget in a fixed receiver case can be improved using longer dwell time target.

A primary code embedded in the transmitted signals is used for imaging. Due to the low bandwidth of the GNSS's primary code, the optimum range resolution can be obtained under a quasi-monostatic geometry. Azimuth resolution can be improved using an extended dwell

time on a target. Those spatial resolutions can be analysed using GAF for both straight-lined (for dwell time on target less than 5 minutes) and curved trajectory (for 5 minutes or more).

For processing algorithms, the synchronisation algorithm was used to track parameters (time delay, Doppler frequency, and phase) from a directly received signal. These parameters were then used to construct a reference signal used for range compression with a radar signal. The BPA, a time-domain algorithm, was used to generate a bistatic image. This step requires the knowledge of a transmitter and a receiver positions to back-projection track range-compressed signal.

Chapter 4

Experimental Campaign and Signal Pre-processing

4.1 Introduction

As this thesis was aimed to establish frameworks for non-coherent and coherent multistatic SAR through experimental methods, an experimental campaign was conducted to obtain and pre-process data for that purposes. This chapter describes the experimental campaign, the methodology of experimentation, the experimental setup and measurement parameters, as well as pre-processing and image formation results to verify the validity of the data.

In the campaign, a set of measurements was conducted to acquire signals from four different GNSS satellites (two GPS and two Galileo satellites), which are belong to two different GNSS constellations. The GPS L5, and Galileo E5a and E5b signals from those satellites were recorded, for both direct arrival and reflection from the same target area. The measurements were done either simultaneously or with very short time separations between them, and widely varying bistatic geometries that go beyond quasi-monostatic.

The experimental system that used for measurement those signals comprises a receiver and two antennas (one for direct signal and another one for reflection signal). It recorded the signals in a basis of a block of 10-minute and followed by a gap of 5-minute, for approximately six hours. Based on a total time of measurements and signals received, forty-six datasets were obtained. These data allow experimental exploration of multistatic signal

processing concepts with point-like returns and real target areas, in non-coherent and coherent modes. In addition to the measurements, these data were verified its validity from a signal strength in acquisition until synchronisation results and point spread function (PSF) conformability in pre-processing and image formation steps.

The author of this thesis designed the experimental campaign, conducted the experiment, collected the data from the satellites, verified and processed the data into images, and performed all signal pre-processing. However, receiver modification and data capture software development have been done prior to the start of this study.

4.2 Experimental System

The experimental system constructed for the experimental campaign is shown in Figure 4.1. This system was built at the University of Birmingham using commercial off-the-shelf components, including antennas for direct and reflected signal reception, and a software-defined GNSS receiver that was specially modified to operate as a SAR receiver. The system was installed on the roof of Gisbert Kapp building, within the campus of the University of Birmingham.

An experimental system is used to receive and record multiple GNSS satellite signals simultaneously both direct and reflection arrivals. In this thesis, the experimental system, as shown in Figure 4.1, comprises three components: a heterodyne channel (HC) antenna, a radar channel (RC) antenna, and a GNSS-based SAR receiver. The HC and RC antennas were used to receive different arrival of signals. The HC antenna captured direct signals from satellites whilst the RC antenna captured reflection signals from the target area. The receiver was converted from GNSS receiver to operate as SAR receiver. Both signals are recorded by the receiver for further processing into passive SAR imagery.

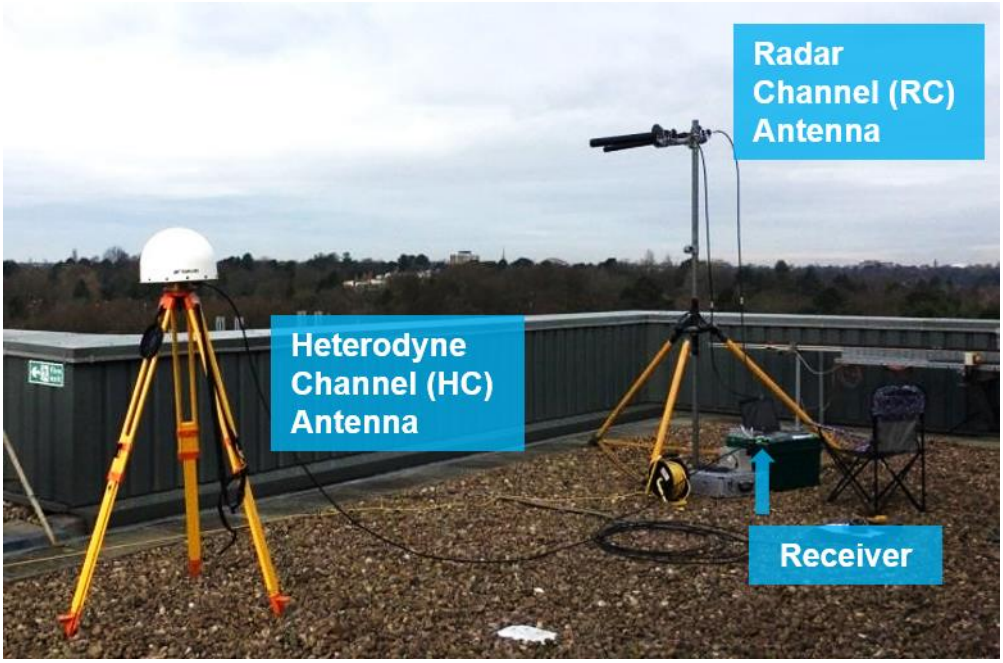

Figure 4.1 Experimental system, (adapted from [25])

4.2.1 Antennas

The heterodyne channel antenna was used to receive direct signals from satellites but also acting as point-like targets (see section 4.3). In this case, a low-gain omnidirectional antenna was used since its field of view could maximise the number of satellites that can be viewed at any time. The polarisation is right-handed circular polarisation (RHCP) to match the polarisation of the transmit signals. It is because the GNSS signals are transmitted with RHCP, and their polarisation are remain unchanged when directly arrive at the HC antenna. The chosen antenna was a choke-ring antenna model CR-G5, built by Topcon [74], that can reject signals reflected off the ground underneath it. It has two operating frequency bands. The lower band is 1230 MHz ±70 MHz and the upper band is 1565 MHz ±50 MHz. These frequency ranges cover all major GNSS constellations. The antenna has a symmetrical pattern (omni-directional) with a gain at zenith (90˚) of 7.5 dB and 5 dB for lower and upper

bands respectively. The antenna has a built-in LNA, with a gain of 43 dB and a noise figure (NF) of 1 dB.

The radar channel antenna was pointed towards the target area to receive signals reflected off the targets. Since the reflection signals are weak, thus collecting this signal in a specific direction of the target area requires a high-gain directional antenna. The antenna was cross-polarised to account for changes in signal polarisation due to target reflection mechanisms. For these purposes, the chosen antenna was a helical antenna model AMHP13-13L/909 which was built by Cobham Antenna Systems [75]. This model has a gain of 13 dBi with azimuth and elevation beamwidths of 40˚ and 40˚, respectively (Figure 4.2). This antenna has operating frequencies range from 1.00 to 1.50 GHz, which cover the candidate satellite signals (Galileo E5a and E5b, and GPS L5). The LNA connected to the RC antenna has a gain of 34 dB.

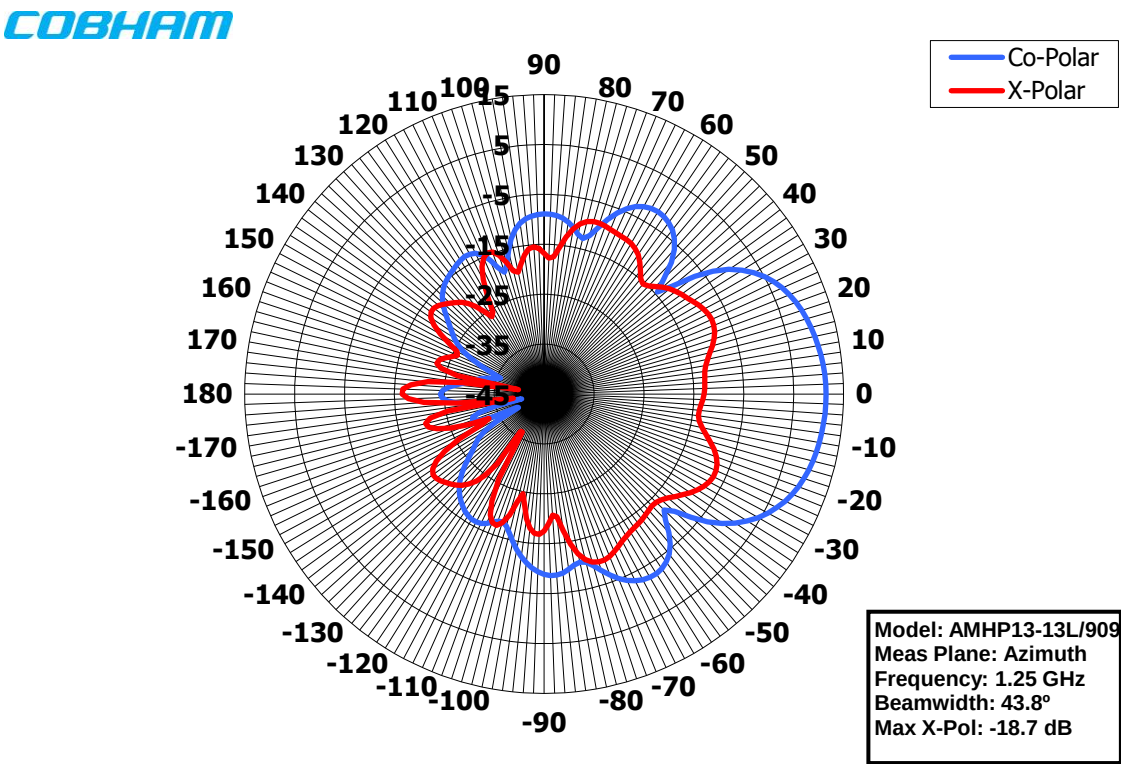

(a)

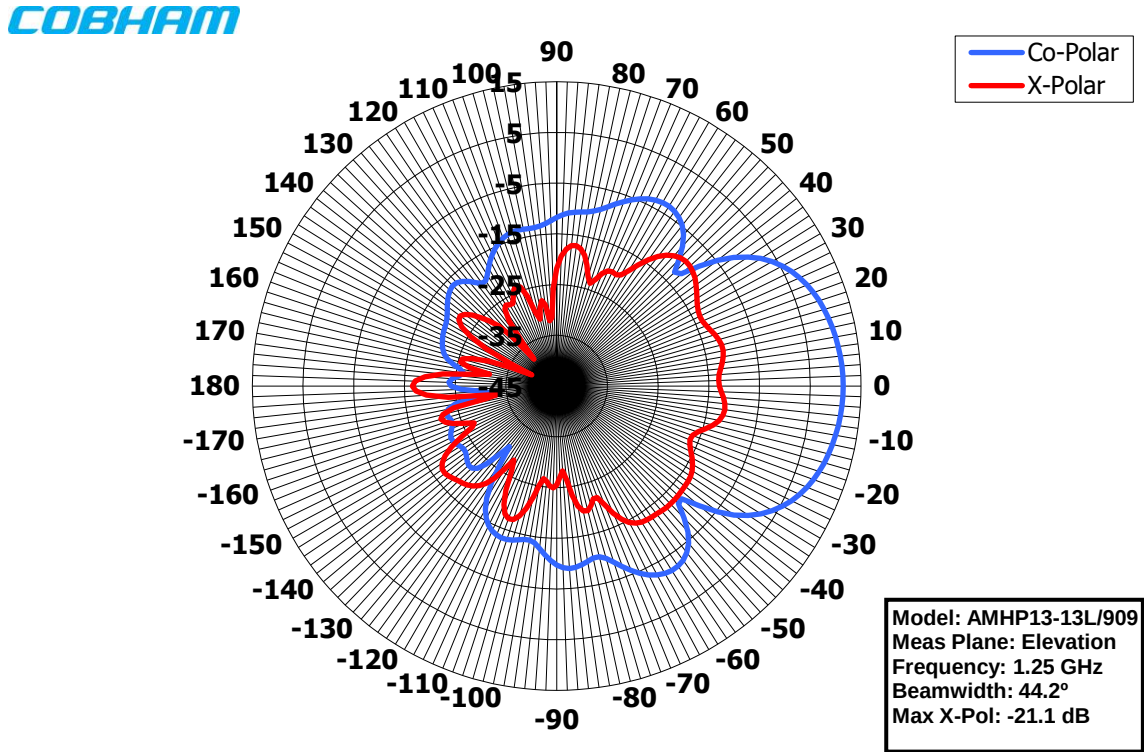

(b)

Figure 4.2 Radiation patterns of the RC antenna at 1.5 GHz measured in (a) azimuth and (b) elevation planes, (courtesy of Cobham Plc.)

4.2.2 GNSS-based SAR Receiver

The GNSS-based SAR receiver is SX-3 (Figure 4.3), a commercial off-the-shelf (COTS) GNSS receiver, which was built initially by IFEN GmbH for navigation purposes. Its operation is based on software-defined GNSS receiver and can be reconfigured according to recording signals. The receiver can receive GNSS signals from four major global constellations (GPS, Galileo, GLONASS, and BeiDou) as well as a regional constellation, IRNSS. Table 4.1 shows the signal capability of the SX-3 receiver, [76].

Table 4.1 Signal capability of the SX-3 receiver

Satellite Constellation	Signals
GPS	L1, L2P & L2C, L5, and SBAS L1
Galileo	E1, E5a, E5b (including AltBOC), and E6
GLONASS	G1 and G2
BeiDou	B1 and B2
IRNSS	L5 and S-band

The receiver has two main parts: front-end and computer system. Both parts communicate with each other through the USB 3.0 interface. At the front-end, the receiver has two input channels to receive signals simultaneously with a bandwidth of 50 MHz per each input channel. Both channels are identical since they share the same internal clock. The receiver has acquisition and tracking sensitivities of 19 and 10 dBHz, respectively. On the computer system, with Intel Core i7-4790k processor, the receiver can record 300 different satellite signals simultaneously (at 60% load) in real-time measurement. Satellite signals are recorded as a complex number in an intermediate frequency (IF) samples format and stored as a file for post-processing. The receiver has been converted to operate as GNSS-based SAR receiver through European Space Agency (ESA) grant. This capability, as a GNSS-based SAR receiver using a single satellite, has been demonstrated in [23] . In this thesis, both input channels were used, one channel was connected to the HC antenna and another one channel was connected to the RC antenna.

Figure 4.3 The GNSS-based SAR receiver, (adapted from [25])

4.3 Targets

Two types of targets were used in the experimental campaign, one is a point-like target, and another one is a real target area. A point-like target was used in the coherent experiment, whereas a real target area was used in both the non-coherent and the coherent experiments.

A point-like target is a target with small physical dimensions relative to the radar's imaging resolution, but some point-like targets can have a very high RCS. In contrast, an extended target is defined by the multiple scatterers model. Its radar cross-section (RCS) is represented by many point-like reflectors.

Ideal point-like targets for verifying signal processing algorithms are spheres, but their low RCS combined with the low GNSS transmit power makes them unfeasible. Moreover, corner reflectors are not recommended to be used in bistatic configuration although they have high radar return in backscatter direction. This is because, in bistatic measurement, their response is no longer dominated by specular scattering which makes high backscatter. Therefore their radar return will be lower and difficult to predict at some bistatic angles beyond 6˚ [17]. Alternatively, the HC antenna, which was Topcon's omnidirectional antenna was used to serve as a high-reflectivity point target at zero range from the receiver (at the origin), [77]. In such case, know power radiation at any directions can be expected from the Topcon

antenna due to the information on radiation pattern provided in section 4.2.1. In this case, a direct signal from a satellite is used to produce point-spread function (PSF) of the target. This method is similar to using an active transponder, but a cable is used instead of free space transmission.

A real target area is located to the west of the Gilbert Kapp building on the University of Birmingham campus. The area comprises a variety of targets with a mixture of the urban and rural environment, as shown in Figure 4.4. On the right-hand side of the area comprises mainly lawns with tree lines at their sides. This is in contrast to multi-storey buildings that mimic an urban area to the left-hand side. Many distinctive features are in this area including sports fields, residence towers (~1.2 km range) marked as target (A), tree lines (at 700 to 900 m range) marked as target (B), as well as different complex buildings on the lower-left part of Figure 4.4, which are the university's Medical School, Women's Hospital (C), multi-storey car park (E), Medical School and Institute of Biomedical Research (D), Institute of Translational Medicine (F), and Queen Elizabeth Hospital Birmingham Charity (G). Height of the target buildings is in similar range between 20 m to 30 m except for the rightmost residence tower block in the target area A. It is the tallest target with a height of 47 m [78].

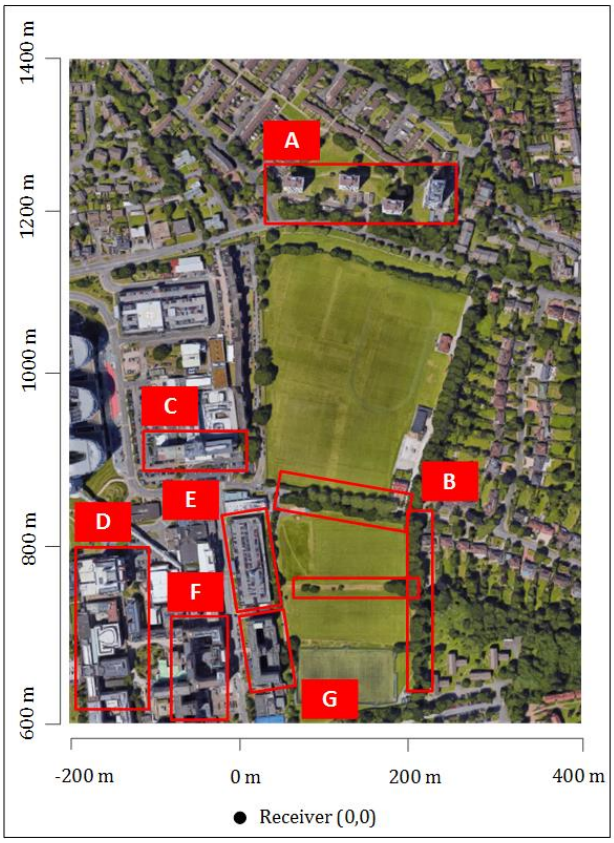

Figure 4.4 Satellite imagery of the target area (© Google Earth), (adapted from [25])

4.4 Satellites Used

The signals were acquired from four satellites that are two GPS satellites (BIIF-05-30 and BIIF-07-09) and two Galileo satellites (GSAT-0205-E24 and GSAT-0214-E05). Signals from these satellites (Galileo E5a and E5b, and GPS L5) were recorded in a 10-minute block followed by a 5-minute gap basis. The satellites parameters are listed in Table 4.2 and their trajectories during the time of measurement are shown in Figure 4.5. The satellite's azimuth angle is clockwise-measured relative to the north and shown as the figure at the outside of the plot. The elevation angle is shown inside the circle. The bistatic angles are defined at the midpoint of satellite's trajectory (i.e. the centre of synthetic aperture) and the receiver line-of-sight via the centre of the target area. These notations under bistatic geometry are depicted

in Figure 4.6. Although only four satellites were used, those satellites were observed for extended periods of time (more than one hour in total), therefore, within each acquisition, there is a substantial change in the bistatic geometry due to satellite motion.

In total, the signals were recorded into thirty-three raw datasets, based on the total time of measurement and number of frequencies used, with the size of 6 GB per raw dataset (both channels). As a result, disk space of nearly 200 GB was used to store these raw datasets. These raw datasets were then processed into forty-six experimental bistatic images with a size of 20 MB each image and size of 920 MB in a total of images.

The satellite signals used in this work were Galileo E5a-Q and E5b-Q, and GPS L5-Q. These are so-called pilot signals which do not contain navigation messages. As a result, the signals are easier to synchronise since navigation message decoding is omitted. These signals had the same ranging code bandwidth at 10.23 MHz. Thus they provided the same system range resolution.

In passive SAR system, the range resolution is varied with ranging code bandwidth and bistatic angle (see Chapter 3). Despite the same bistatic angle, using signals with different ranging code bandwidth can lead to bistatic images with different range resolution. If range resolutions are much different, they can deteriorate resultant range resolution when those bistatic images are combined to form a multistatic image. Therefore, using the signals with the same ranging code bandwidth can prevent further image quality degradation.

From Figure 4.5 and Table 4.2, it can be seen that a variety of satellite's azimuth and elevation angles were made so that high spatial diversity of satellite position can be obtained. Total satellite positions were spanned from 48˚ until 203˚ in azimuth plane and between 26˚ to 80˚ in the elevation plane. Equally, these satellites were chosen because they were in the

area behind the receiver to reduce further degradation in range resolution which caused by bistatic geometry.

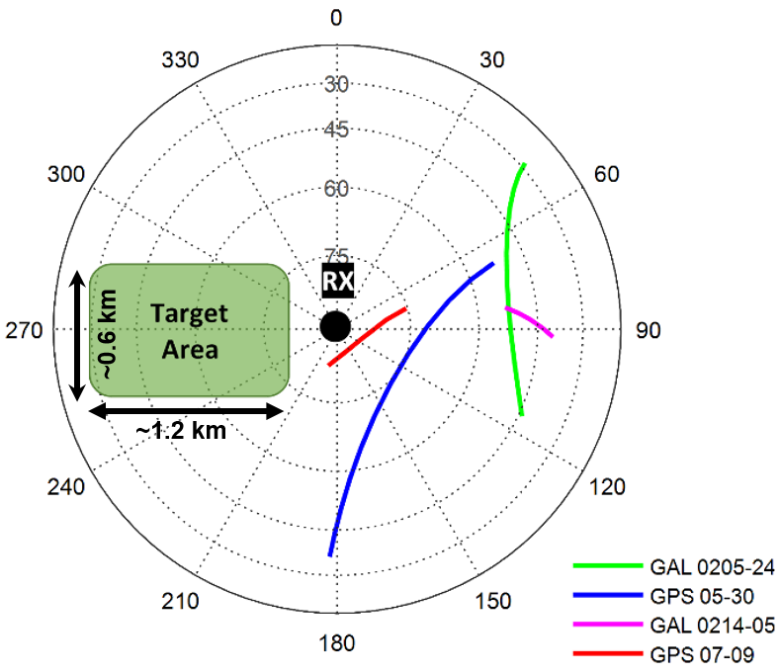

Figure 4.5 Satellites trajectories during the time of measurement, (adapted from [25])

Table 4.2 GNSS signals characteristic and experimental parameters

Parameter	GPS BIIF-05-30	Galileo GSAT-0205-E24		GPS BIIF-07-09	Galileo GSAT-0214-E05
Signal	L5	E5a	E5b	L5	E5a
Modulation	BPSK	AltBOC	AltBOC	BPSK	AltBOC
Carrier Frequency (MHz)	1176.45	1176.45	1207.14	1176.45	1176.45
Ranging Code Bandwidth (MHz)	10.23	10.23	10.23	10.23	10.23
Dwell Time on Target (s)	600	600	600	600	600
Azimuth, |θ| (Degree)	182.19 – 66.67	117.24 – 48.36		203.39 – 71.99	81.51 – 93.33
Elevation (Degree)	34.34 – 51.00	42.55 – 26.37		80.30 – 72.97	55.04 – 38.84
Bistatic Angle, |β| (Degree)	91.51 – 56.49	49.35 – 48.54		91.80 – 75.90	53.74 – 40.47

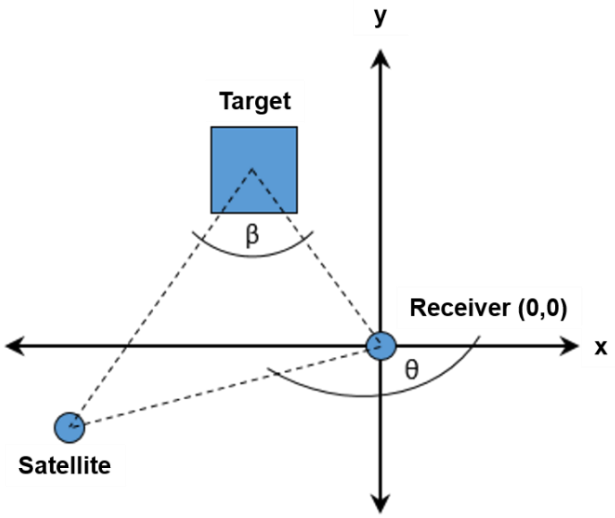

Figure 4.6 Bistatic imaging geometry, (adapted from [25])

4.5 Experiment Designs and Procedures

Two separate experiments were conducted in this campaign for two different combination techniques. They were ultimately aimed to establish individual frameworks for non-coherent and coherent multistatic SAR. Design of the experiments was described below.

4.5.1 Non-coherent Multistatic SAR Experiment Design

The aim of this experiment was to understand how image information space of a multistatic image may be able to be enhanced compared to its bistatic counterparts. The first question was whether the information could be enhanced in a non-coherent multistatic SAR image compared to a single bistatic one. If the non-coherent combination can enhance information, the next question was how the enhancement could be achieved. For this question, it was assumed that information could be enhanced using a large number of bistatic images with the condition that the images were obtained from a sufficiently diverse spatial position of the satellites. In this experiment, forty-six experimental bistatic image which obtained from

the diverse spatial position of satellite between 48˚ until 203˚ in azimuth were used to achieve information enhancement. This understanding was ultimately to establish a framework for non-coherent multistatic SAR.

A basic non-coherent combination was used to form a multistatic image since this experiment was focussed on information enhancement compared to a single bistatic image. In this case, the experimental bistatic images were combined by adding their magnitudes in a pixel-by-pixel basis. The distinct feature of non-coherent combination is that it has no restriction on coherence between signals. Thus, this experiment used all available bistatic images. The real target area was the only type of target used in this experiment since it was more informative target than a point-like target when considering the information contained within images. After the multistatic image was formed, information was compared with its bistatic counterparts. Since the phase information is not available in the multistatic image, the comparison concentrated on information related to the magnitude of echoes strength that can be seen on the images. Specifically, geometric features and variation of echo strength were inspected.

According to the experiment design, a procedure to conduct this experiment were summarised as follows.

Step 1) Analysed the available GNSS trajectories and chose the candidate signals

Step 2) Obtained the candidate GNSS satellites signals

Step 3) Performed synchronisation

4.5.2 Coherent Multistatic SAR Experiments Design

The coherent combination can benefit passive SAR system with substantial spatial resolution improvement. Since limited experimental results have been published, this experiment aimed to experimentally validate whether the principles of coherent combination can be applied to a multistatic SAR system to enable that improvement. This experiment used the GNSS-based system as an experimental testbed with two different types of target. The first target was a point-like target, whereas the second target was a real target area. The first step used the point-like target to validate at a system level, and the same method was then applied to the real target area for validating at an image level.

According to the experiment design, a procedure to conduct this experiment were summarised as follows.

Step 1) Analysed k-space (Chapter 6, section 6.3) support of the available GNSS trajectories and chose the candidate signals

Step 2) Obtained the candidate GNSS satellites signals

Step 3) Performed synchronisation

4.6 Data Verification

From acquisition to signal pre-processing stages, data were verified to ensure that they had the good quality to be used in the signal processing stages. The verification includes signal strength at an acquisition stage, synchronisation outputs, and PSF conformability to the theoretical expectation. Figure 4.7 shows the main part of the SX-3 software when the configuration was loaded and recording signals. It showed the details of the acquiring signals. From Figure 4.7, at the fourth row, carrier-to-noise-ratio (CNR) was used to judge

the quality of the signal being processed. Signals were processed when they have CNR between 30 to 50 dBHz, which is typical CNR for the GNSS satellites. The front-end of the receiver had a bandwidth of 50 MHz. As a result, the SNR after the front-end of the receiver was between -46 to -20 dB. Data are recorded at an intermediate frequency (IF), not in the baseband. Therefore, in synchronisation and image formation, the IF was required to be removed. Sampling frequency was set by the factory default to 20 MHz. As a result, each 1 ms had 20,000 samples.

Figure 4.8 shows an example of synchronisation results which are tracked delay, track Doppler, and phase spectrum. These results obtained from E5a signal of Galileo satellite (GSAT-0205-E24), which was acquired at 09:45-09:55 am. From Figure 4.5, this dataset was at the beginning (at the bottom) of the satellite's trajectory in the green line. The tracked delay shows the delay of primary code during the time of measurement. The tracked Doppler shows the frequency shift when the satellite passes the receiver. From Figure 4.8 (b), the shift was decreased as expected as the satellite approached the receiver. This shift will become zero when the satellite was behind the receiver and started to increase when departing from the receiver. The amount of Doppler shift was 220 Hz which is within the theoretical range of 4 kHz, [79]. This Doppler shift amount was coincident with the phase spectrum or Doppler spectrum in Figure 4.8 (c), which was 219.6 Hz. The linearity of tracked delay and Doppler as well as a near-perfect chirp of the phase spectrum show stability and confirm the validity of the data used in the experiments.

	1	2	3	4	5	6	7	8	9
System	GPS	GPS	GPS	GPS	Galileo	Galileo	Galileo	Galileo	Galileo
Service	L1CA	L1CA	L1CA	L5	E1	E5a	E1	E5a	E1
PRN	16	18	26	26	11	11	12	12	14
C/N0 [dBHz]	42.54	43.64	43.19	49.21	41.46	44.20	42.85	44.50	46.04
Elevation [deg]	61.50	59.50	61.73	61.73	65.14	65.14	56.16	56.16	35.53
Azimuth [deg]	290.84	59.84	194.24	194.24	253.51	253.51	56.20	56.20	94.34
Lock Time [s]	580.65	580.66	580.66	589.00	566.07	570.77	566.07	570.77	580.66
Receiver ID / MC	0 / -	0 / -	0 / -	1 / -	5 / -	6 / -	5 / -	6 / -	5 / -
Range Rate [m/s]	-230.34	293.20	284.68	284.68	-235.38	-235.45	259.09	259.04	1019.15
Pseudorange [m]	19277352.1	19312416.8	19302217.1	19302216.1	20916506.0	20916503.2	20909256.0	20909253.7	1856039
Carrier Phase [cyc]	N -831849.3	N 829005.6	N 783887.4	F 542219.8	F -720694.7	F -538184.4	F 705825.6	F 527077.0	F 280037
Doppler [Hz]	1210.45	-1540.76	-1496.02	-1117.14	1236.95	923.97	-1361.55	-1016.51	-5355.68
CMC Doppler [Hz]	-134.76	10.32	159.24	1.13	1.19	-5.00	-3.76	-3.69	8.19
#Paths/Chi2	- / -	- / -	- / -	- / -	- / -	- / -	- / -	- / -	- / -
SPP Flag	Ok	Ok	Ok	Ok	Ok	Ok	Ok	Ok	Ok
Tropo. Delay [m]	2.61	2.66	2.60	2.60	2.53	2.53	2.76	2.76	3.94
Iono. Delay [m]	2.15	2.27	2.25	4.04	2.13	3.82	2.35	4.21	3.39
SPP Residual [m]	-0.19	0.23	-0.04	0.00	0.50	-0.01	0.36	-0.01	-1.11
PR Accuracy [m]	1.50	1.50	1.50	1.50	1.50	1.50	1.50	1.50	1.50
Orbit Accuracy [m]	4.12	4.12	4.12	4.12	3.60	3.60	3.60	3.60	3.60

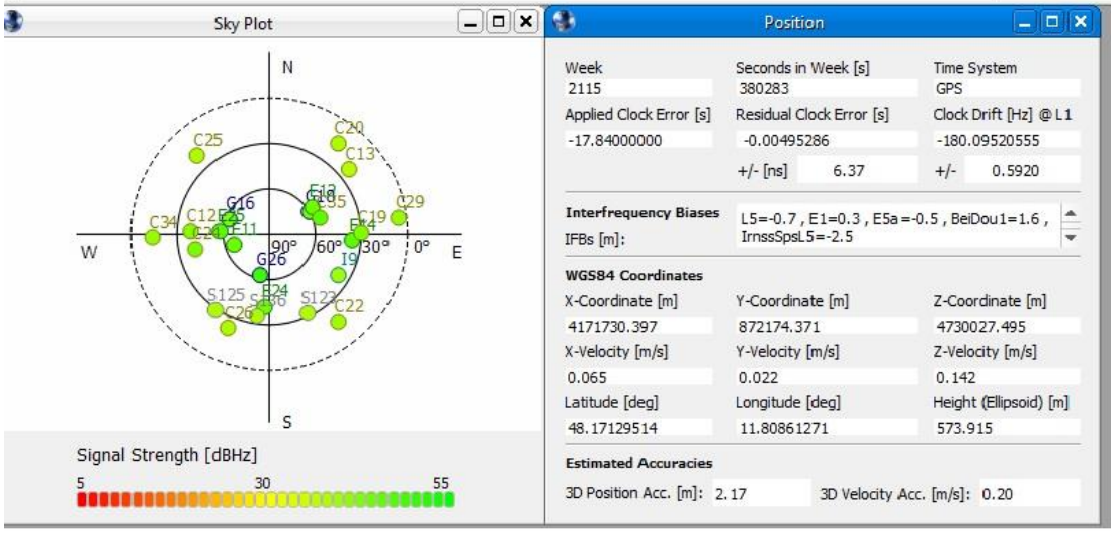

Figure 4.7 Main part of the software window when recording signals (© Ifen)

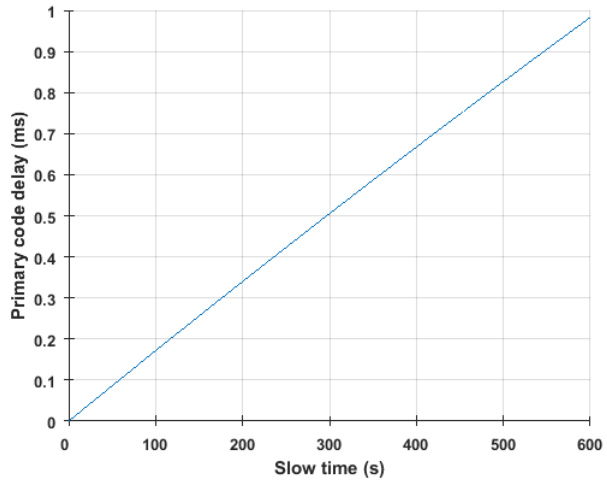
Primary code delay (ms)
Slow time (s)
0
0.1
0.2
0.3
0.4
0.5
0.6
0.7
0.8
0.9
1
0
100
200
300
400
500
600

(a)

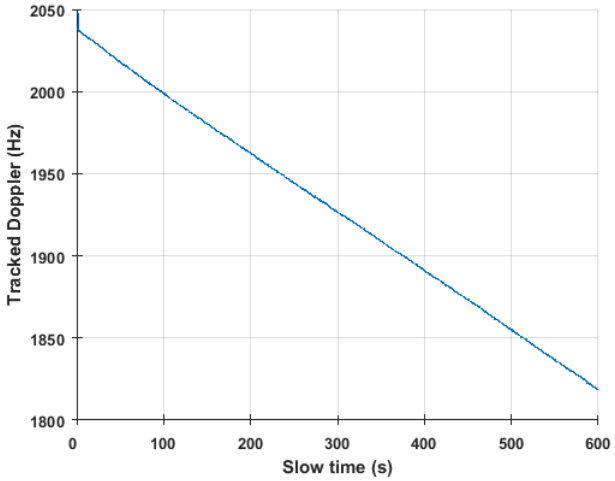
Tracked Doppler (Hz)
Slow time (s)
1800
1850
1900
1950
2000
2050
0
100
200
300
400
500
600

(b)

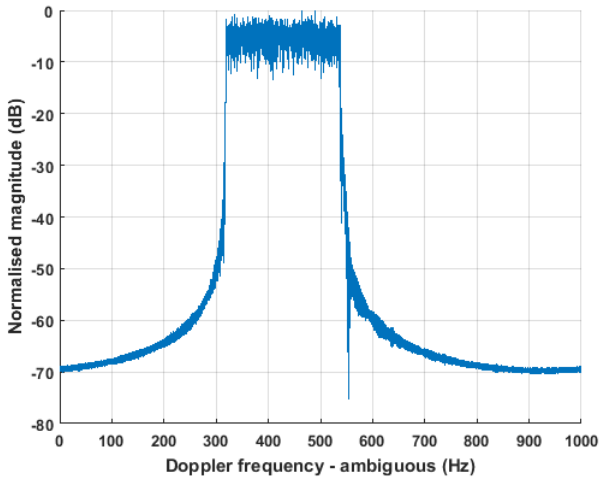

(c)

Figure 4.8 Synchronisation results obtained from Galileo GSAT-0205-E24 acquired at 09:45, which are (a) tracked delay (b) tracked Doppler, and (c) phase spectrum

The final step of data verification was to obtain the experimental bistatic PSF and compare to its theoretical expectation. This is done using a point-like target to produce its corresponding PSF. The experimental PSF of the target was compared with the corresponding theoretical PSF. The theoretical PSF was produced using Eq. 3.3.

If both PSF is in good agreement (e.g. overall shape or main lobe), this indicates that the system is working correctly and corresponding bistatic images can be used in the experiments. Figure 4.9 shows an example of the PSF results using data acquired from GPS BIIF-05-30. Full PSF results can be found in Appendix A. All of them showed a good agreement between experimental and theoretical expectation. This indicated that the system and bistatic processing were working correctly, and bistatic PSF and images can be used in the combinations.

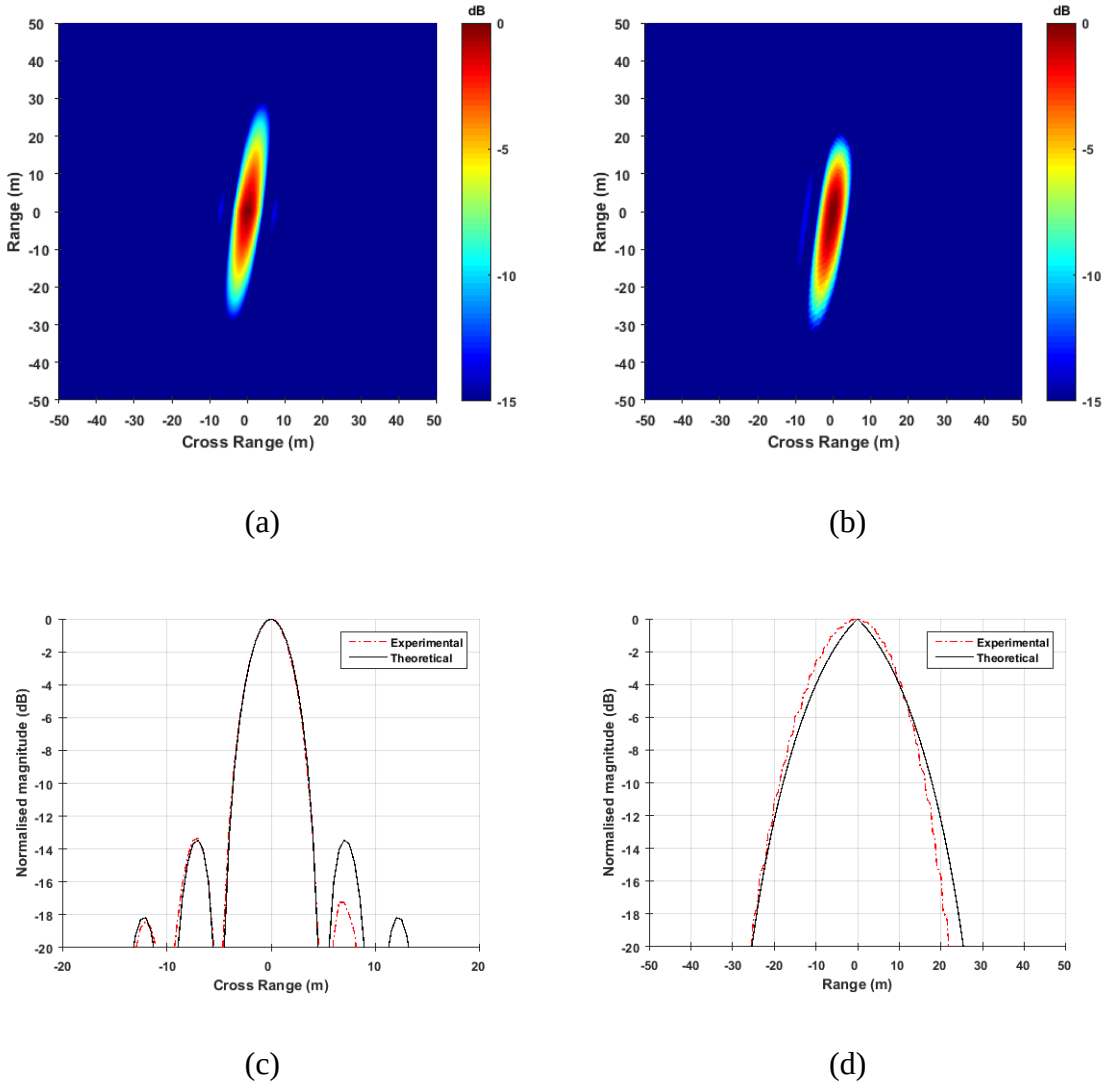

Figure 4.9 Comparison of (a) theoretical and (b) experimental bistatic PSF in (c) cross-range and (d) range directions for system acceptance test

For the image calibration, the direct compressed signal was used as a reference signals at 0 dB for normalisation echo strength in radar image into dB scale. Among the bistatic images, the maximum direct signal was used to normalise all forty-six images so that they can be directly compared.

Data were process into bistatic and multistatic images using processing routines written in MATLAB. All images were produced using the same grid where the origin is at the receiver (0,0). Thus no further co-registration process required.

The routines from extracting raw data, synchronisation to producing bistatic imagery has been developed and modified for many years by members of the Microwave Integrated System Laboratory (MISL), the University of Birmingham including Dr Michail Antoniou, Dr Hui Ma, and Dr Dimitrios Tzagkas. The author of this thesis modified the routines for bistatic processing of the GPS L5 signal and developed the routines for multistatic processing.

4.7 Summary

The experimental campaign was described in this chapter. The individual experiments were designed to achieve the goal, the one for non-coherent multistatic SAR and the other one for coherent multistatic SAR. The experimental system comprises three parts, the HC antenna, the RC antenna, and the GNSS-based SAR receiver. It was used to acquire signals from GNSS satellites. The experimental system was tested that it was functioning correctly, and all experimental bistatic images were matched with their theoretical expectations. The GNSS satellites were acquired their signals both came directly from the satellites and came via the target area. Two different types of the target were used, one is a point-like target, and another one is a real target area. The chosen satellites were behind the receiver so that range resolution was as less degraded as possible. These signals were recorded simultaneously using the experimental system, which consists of two separate antennas and a single GNSS receiver.

Received signals are then processed into passive imagery using the routines written in MATLAB. The receiver records direct and reflected signals through its separate input channels. The synchronisation can be done at the receiver for all satellites in near real-time. Image formation can be done offline. Synchronisation was performed to recovery coherence

of the received signals. This step can be done in near real-time. Image formation used the output of the synchronisation and reflection signals to produce passive bistatic SAR imageries. This set of the bistatic images was used to form a multistatic image, both coherent and non-coherent. For comparison, results from multistatic techniques were compared to their corresponding bistatic counterparts.

Chapter 5

Non-coherent Multistatic SAR

5.1 Introduction

In GNSS constellations, a multitude of satellites is orbiting above the particular area with high spatial diversity of their trajectories. In this case, it is preferable to form a multistatic SAR image using the non-coherent combination. This is because images obtained from different viewing angles can be combined regardless coherency of their mutual phase relationship. In other words, this technique relaxes a restriction of having coherence in forming a synthetic aperture by summing magnitude of the image in a pixel-by-pixel basis rather than its complex value.

This chapter presents the experimental results of non-coherent multistatic SAR obtained the GNSS-based SAR system. Forty-six experimental bistatic images were combined to form a multistatic image. These bistatic images were obtained from a variety of imaging geometries with total azimuth span from 48 to 203 degrees and a total elevation span between 26 to 80 degrees. Comparing that experimental multistatic and bistatic images, their appearances were first analysis by visual identifying an object. The analysis was further done by extracting information within the images. Finally, the information in terms of echo strength variation instead of combining image was combined to investigate whether they can be used to distinguish between different objects, e.g. trees vs buildings. The idea behind this is that

if two objects differently exhibit their scattering properties over different observing angles, an information-combined multistatic image can be used as a basic classification tool to distinguish objects.

5.2 Non-coherent Multistatic SAR Experiment

The experimental bistatic and multistatic images were compared to verify whether information can be enhanced in term of a number of identified targets. Basic geometric features (edges and shapes) then were inspected. Dimensions of the target were estimated and compared to the reference estimation from Google satellite imagery. Variations of the echo strength of the two different types of objects (tree vs building) were plotted to verify the ability of non-coherent multistatic in classifying composition of the scene whether they are trees or human-made structures. This step information contained within individual bistatic images was combined instead of images themselves.

Procedures to conduct this experiment were summarised as follows.

Step 1) Performed image formation to obtain experimental bistatic SAR images

Step 2) Performed a non-coherent combination for non-coherent multistatic SAR experiment

5.3 Non-coherent Combination

The multistatic image was formed by a basic non-coherent combination by adding the magnitude of bistatic image pixels in a pixel-by-pixel basis. The basic non-coherent combination can be expressed as

$$I_M = \frac{1}{N}\sum_{i=1}^{N}|I_i|, \tag{5.1}$$

where I_M is a multistatic image, I_i is an i^{th} bistatic image, $|\cdot|$ is absolute operator, and N is a total number of bistatic images used in the combination.

5.4 Experimental Bistatic Images

Based on the total recording time and the number of acquired signals, a total of 46 experimental bistatic images were obtained from the system under imaging geometry shown in Figure 4.5. Satellite image taken from Google Earth is shown in Figure 5.1 for comparison with the results obtained. Five examples of the experimental bistatic images obtained from different satellites with different bistatic and azimuth angles over the total observation period of six hours are shown in Figure 5.2. Full set of the experimental bistatic images can be found in Appendix B. All images were superimposed manually on a Google Earth photograph of the target area to pair radar echoes with their corresponding targets for comparison only. Their intensity was plotted in dB with the same dynamic range clipped to 35 dB. The colour bar is shown in the last image of this figure (Figure 5.2 (e)). The intensities were normalised to the same value, which is the highest compressed direct signal among those bistatic images so that enables a direct comparison of the relative intensities across the images. The bistatic angle (β) and the angular position (θ), which are quoted in the figures, correspond to the satellite-target-receiver angle and the azimuth spanning of the satellite position during data acquisition, respectively.

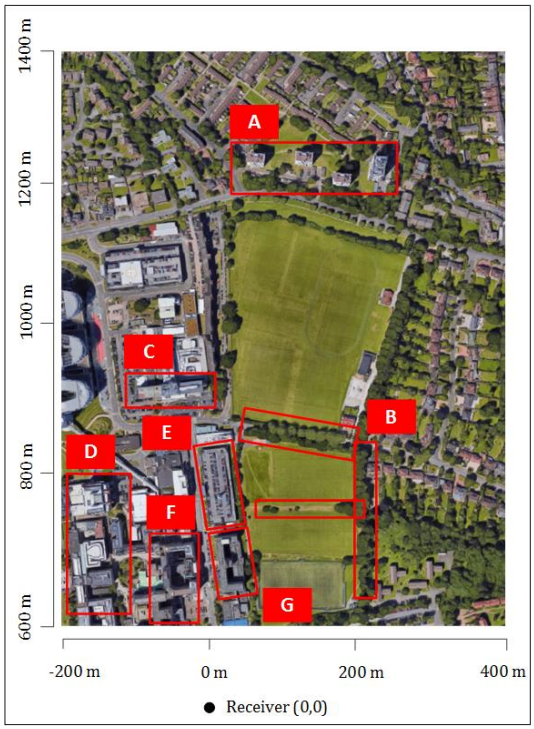

Figure 5.1 Example the satellite image taken from Google Earth

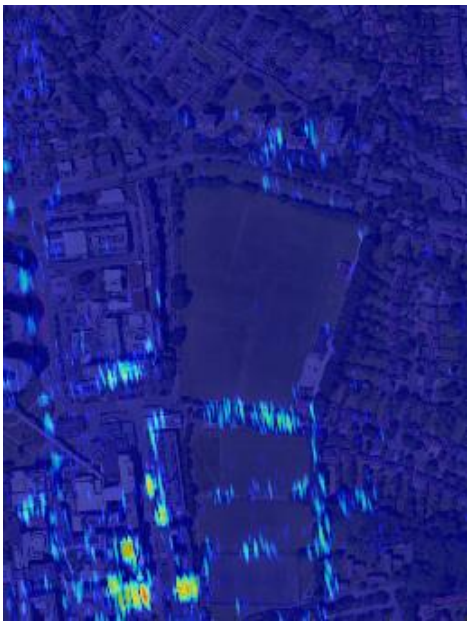

(a) β=53.27˚, θ=76.30˚-70.71˚

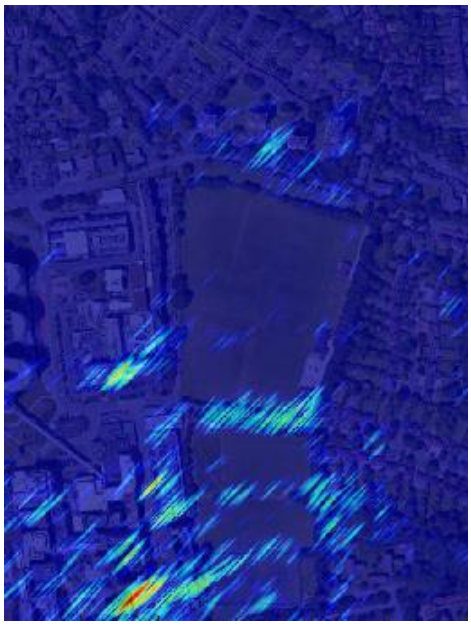

(b) β=61.78˚, θ=70.96˚-68.39˚

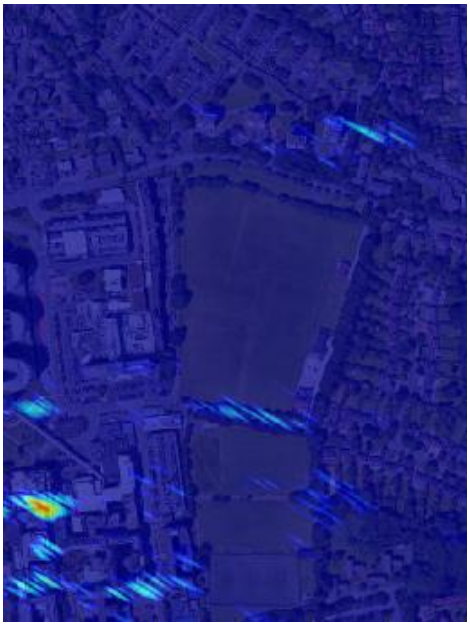

(c) β=43.30˚, θ=88.75˚-91.16˚

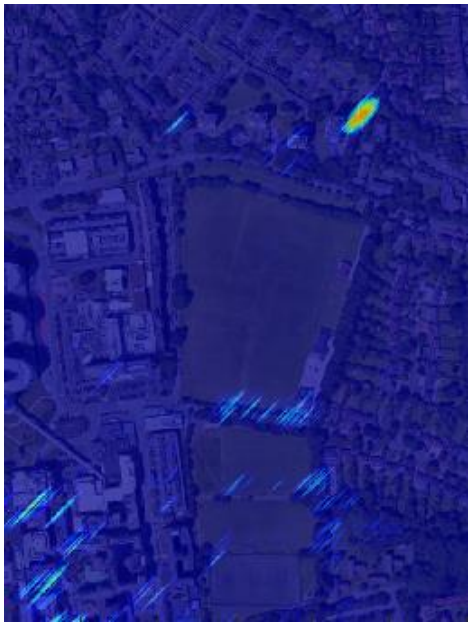

(d) β=87.99˚, θ=184.07˚-126.40˚

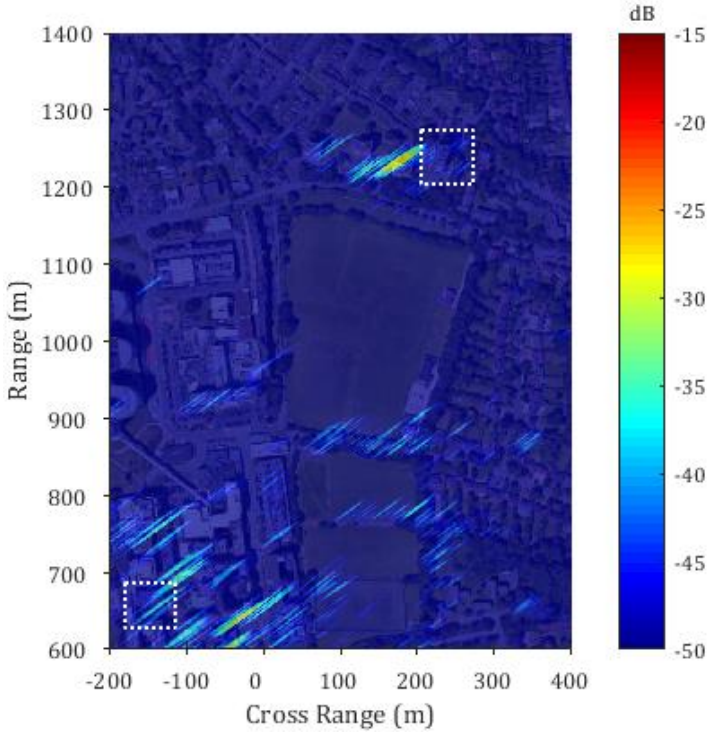

(e) β=79.98˚, θ=83.62˚-74.79˚

Figure 5.2 Example bistatic images obtained from (a) Galileo GSAT-0205-24 E5a, (b) GPS BIIF-05-30 L5, (c) Galileo GSAT-0214-05 E5a, and (d)-(e) GPS BIIF-07-09 L5

From individual bistatic images, the radar returns appear point-like. This is caused by the modest spatial resolution of the passive SAR system and the limited system sensitivity due to the low satellite power flux density near the Earth surface. As a result, only the strongest echoes at a particular scattering angle can be visible. Despite echoes from extended objects such as a building, they still appear point-like.

Although all bistatic images were obtained from the same target area with the same fixed receiver, radar returns appear differently and are varied by the satellite position. This is because scattering properties of an object in the bistatic geometry are varied with different viewing angles. Substantial different in radar returns is especially spotted from a large complex structural object such as a building. For example, this can be seen prominently from the left part of Figure 5.2 (e) where buildings are dense located.

In addition to different appearances, the returns from the same target area also differed in term of intensity. In this case, different in intensity can be observed at an object that may be highly visible in some images while it may be undetected in other images. For example, the two areas across images, marked by white boxes in Figure 5.2 (e) and corresponding to the areas A and D in Figure 4.4, which is shown again in Figure 5.3 (b) to aid analysing the multistatic results. The change in echo intensity measured across all images from the largest tower block at the upper right corner in the image. This was up to nearly 30 dB. For the medical school at the lower left part of the building, this can be up to 20 dB (Table 5.1).

Furthermore, shadowing effect can be observed from the images, for example, the area beyond the target C, This area affected from shadowing due to the height of the target C and the buildings on the lower left part of the scene are higher than the area beyond the target C.

With the fixed receiver position at the bottom of the scene and most of the satellite positions used, shadowing effect can be expected from that area.

Table 5.1 Examples of intensity change across images

Target	Minimum Intensity (dB)	Maximum Intensity (dB)	Difference (dB)
A	-42.35	-13.71	28.64
D	-39.52	-19.78	19.74

5.5 Experimental Multistatic Images

All forty-six experimental bistatic images were combined to form a multistatic image. The experimental multistatic image obtained by the non-coherent combination is shown in Figure 5.3. The image is shown in a similar manner as its bistatic counterparts. It is superimposed with a satellite image taken from Google Earth to pair radar return with their corresponding targets, as the same purpose as in the case of bistatic images. The distinct targets in the scene are marked with letter A-G for help visual comparison with the satellite image taken from Google Earth (Figure 5.1). The image intensity is represented in dB where 0 dB represents the maximum of the compressed direct signal in the multistatic image. A dynamic range was clipped between -20 and -45 dB. The vertical and horizontal axis is the relative distance from the receiver.

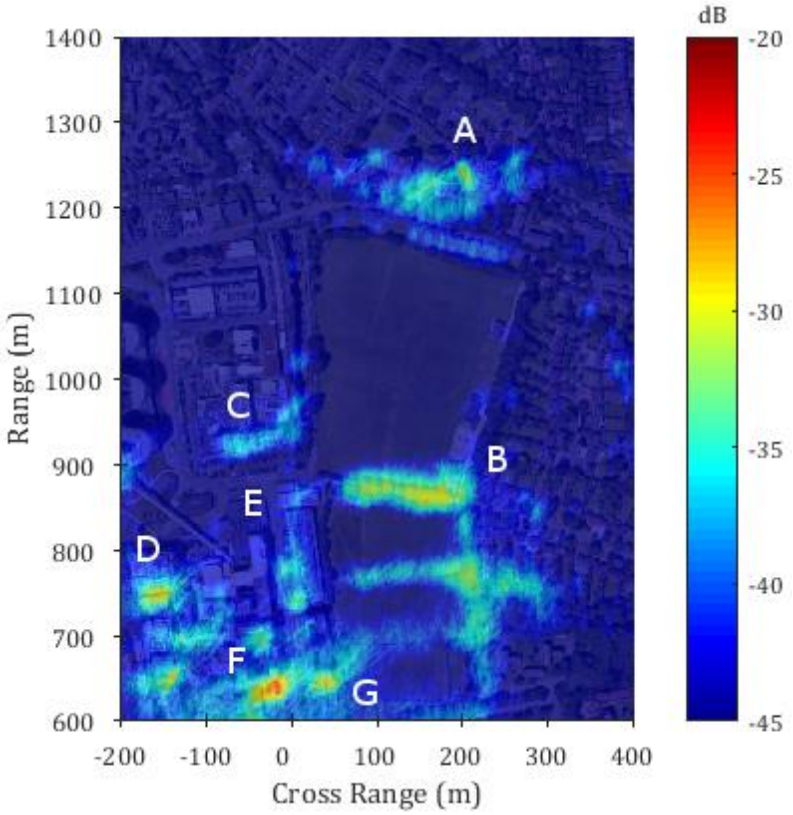

Figure 5.3 The multistatic SAR image, obtained by the non-coherent combination of forty-six bistatic SAR images

Comparing the multistatic image to the bistatic images (Figure 5.2 and Appendix B), in term of the information contained within the image, it is visually apparent that the multistatic image has substantial improvement than its bistatic counterparts. Presence of the targets can be more identified in the multistatic image than in the individual bistatic images. Specifically, all distinctive targets (the target A-G) on the target area, which shown in the satellite image, can be seen in the multistatic image. On the contrary, in the case of the bistatic images, the presence of these targets can be identified depends on the viewing angle. For example, residence tower blocks (the target A) are visible in Figure 5.2 (d) but not in Figure 5.2 (b).

From the multistatic image, radar returns appear rough shape than in the bistatic images. Returns from the same target, especially a building, which has high dispersion of scattering centre across the bistatic images can be gathered to form edge or shape that similar to its corresponding target in the mulstatic image. Interestingly, this enables several enhanced features of targets which can be observed from the image, including edges and shapes. These were not possible to be observed with any single bistatic image due to the resolution and bistatic scattering effects. The edges and shapes were formed roughly as actual features of their corresponding targets. These revealed features show that the multistatic image formed by non-coherent combination can provide not only identifying the presence of a target but also revealing geometric features (edge and shape).

Despite shadowing effect was relief in the lower left part of the image due to diversity of the bistatic image used, it is noted that the area behind the target C cannot be seen due to the height of the target C that block the reflection of targets from those areas. For the tree line between 900 and 1150 m range and 200-300 m cross-range, due to their orientation relative to the receiver position, reflections cannot arrive at the receiver. Some reflections possibly blocked by the trees themselves and some were bounced to other directions. For the houses and trees on the right-hand side, their reflection possibly blocked by the long vertical tree lines at 200 m cross-range. All of these areas cannot be seen from both the multistatic and bistatic images due to the targets were blocked by the other targets surrounding them.

So far, the results showed that the multistatic image contains more information than the individual bistatic images. In the next sections, the geometric information contained within those images will be presented and analysed in detail. Impact of number and configurations

of multistatic on the quality of the final non-coherent combined image will be discussed in section 5.10.

5.6 Edges Identification

Edge is a boundary of an object. It is a basic geometric feature of an image. From the multistatic image, the edge can be seen from the target A, B, C and E. Results of identifying edge from the obtained multistatic image was analysed in this section.

The target A, in which located at the upper part of the scene, was noticeable. The strongest reflection came from the rightmost tower block. This is possibly due to the rightmost tower block has larger dimensions among those tower blocks. The side facing toward the receiver is approximately twice larger than the other three blocks. The metal structure on its roof and the acquisition geometries where strong reflections were obtained are also a possible cause.

The target B consists of tree lines and tree cluster. These trees were in the middle of the scene between 700 to 900 m and towards its far range (~1200 m range). Outlines of these trees were visibly highlighted. The horizontal and vertical tree lines were revealed their outline as an upside-down and inverted L-shape outline. The tree cluster at ~750 m range and 200 to 300 m cross-range were also highlighted. Furthermore, tree lines in which following a road just below the residential tower blocks became distinct. In the bistatic counterpart, these tree lines never have been visible on their own before and been difficult to distinguish.

The target C is a building in which located at ~0 m cross-range and horizontally oriented as a wall facing towards the receiver. The edge of its front and right sides was identifiable. The shadowing can also be anticipated from buildings beyond the target C towards the far range.

Height of these buildings was lower than the target C and those in the lower-left part of the scene. The vertical edge of the target E, at ~700 to 850 m range and 0 to 50 m cross range, was also pronounced. In the following sub-sections, the potential to identify building shapes and estimate buildings dimensions are examined more closely.

5.7 Shapes Identification

The multistatic image reveals not only edges but also the shapes of the target. These geometric details can be seen across the image, especially in the lower left of the image, which was previously difficult to gauge from individual bistatic images.

The target D, at approximately 650 to 750 m range and -200 to -100 m cross range, were visible as a Pi-shape reflection in the image. Most of the visible reflections came from IBR building on the upper part of the target and the Medical School building on the lower part, as well as the building on the right side. Also, shadowing can be observed in the middle part. This effects from this building can be anticipated since the middle buildings had a lower height than the surrounding. In other words, reflections from the middle part of the building were blocked at most bistatic geometries utilised.

The lower part of the target F at 600 to 650 m range, -100 to 0 m cross-range and its adjacent buildings were oriented as an L-shaped building. One side of the wall behaves like a wall towards the receiver. It, therefore, behaved like a large corner reflector. As a result, a high-intensity reflection can be observed from this part. The reflection was seen as an L-shape as their actual shape. On the right of the target F was a part of the target G with one side of the wall is facing towards the receiver as the target F. Hence a presence of this side can be detected with a strong return.

5.8 Dimensions Estimations

In the previous section, the capability of the multistatic image to reveal edges and shapes were shown. The next step is to identify whether it can provide estimates of object dimensions. In this case, buildings in the target area D (the IBR and the Medical School), whose shape was revealed in the previous section, were further examined for this purpose. From Figure 5.4, the target was zoomed in on the individual bistatic images and the multistatic image, as well as the corresponding Google Earth satellite image. It can be seen that in the individual bistatic images, it is not possible to estimate building dimensions. Due to the reflections were not formed into a single extent of target responses, and it is difficult to gauge the boundary of the extent. In the multistatic image, estimation might be possible.

In the multistatic image, responses from the upper and lower buildings were formed as a near rectangle whilst the building in the middle between them was not seen as any shape. Therefore, dimension could be estimated from these extents.

Building dimensions were estimated by measuring the extent of target responses in the image. The red boxes were drawn manually to show the estimated extend of dimensions. Those dimensions then were compared to the dimensions of the building, measured from Google Earth satellite images. The obtained results for the two buildings in Figure 5.4 (e) are shown in Table 5.2 and Table 5.3.

Measured dimensions of both buildings from the multistatic image (Figure 5.4 (e)) and the reference were comparable within 5 m. Although the differences were within that promising narrow range, there are ten times of percent difference between both buildings. Comparing two differences, the medical school buildings have more significant difference than the IBR, e.g. 0.03 m vs 3.91 m. It is possible because the medical building has a similar height to the

vertical building that it is attached to. Thus, estimating the response extent at the side that attached to the vertical building is slightly challenging to find the exact boundary. For the IBR, its height is distinct from the surrounding building. In this case, the boundary of the response extent is clear. As a result, estimating can be done precisely than the medical building.

Table 5.2 Dimensions of the IBR building

Image	Length	Width
Satellite Image	50.50 m	45.35 m
Multistatic Image	50.53 m	44.55 m
Difference	0.03 m	0.80 m
% Difference	0.05	1.76

Table 5.3 Dimensions of the medical school building

Image	Length	Width
Satellite Image	34.32 m	22.43 m
Multistatic Image	30.41 m	25.23 m
Difference	3.91 m	2.80 m
% Difference	11.39	12.48

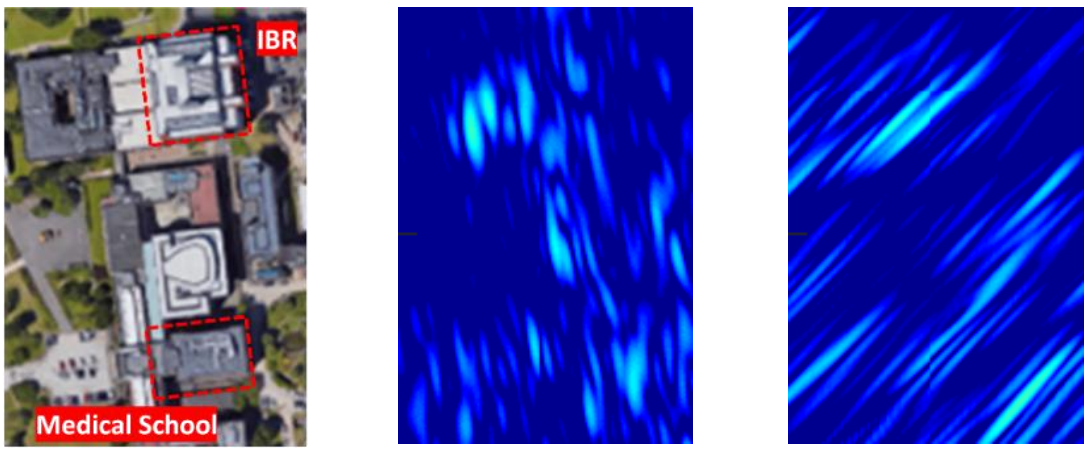

(a) (b) (c)

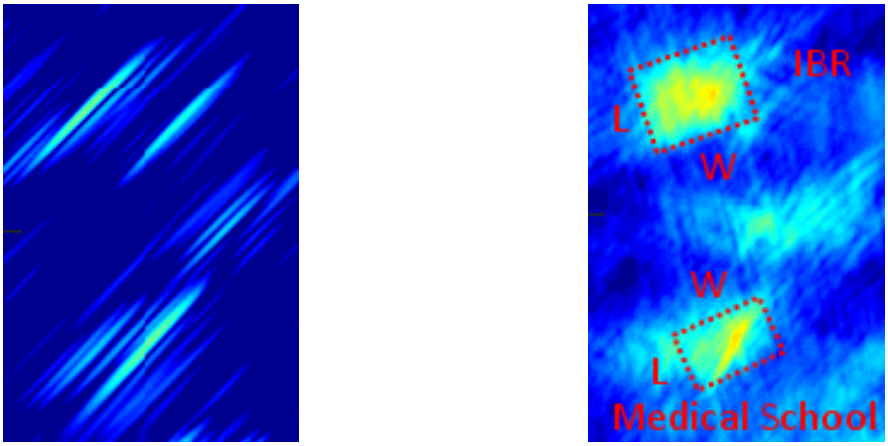

(d) (c)

Figure 5.4 Dimensions measurement for the target D (a) Google Earth satellite image of the target D, (b) bistatic image (Figure 5.3 (a)), (c) bistatic image (Figure 5.3 (b)) bistatic image (Figure 5.3 (d)), and (e) multistatic image

5.9 Context-based Classification

The objective is to identify whether there is substantial variation in echo intensity as a function of acquisition geometry as a function of acquisition geometry. The enlargements of the selected target areas (the four residence tower blocks and tree lines) are shown in Figure 5.5 and variations of reflection strength from these targets are shown in Figure 5.6 and Figure 5.7, respectively. These reflection strengths were extracted from the individual experimental bistatic images. The vertical axis represents the strength of reflection in dB where the upper bound, 0 dB, represents the highest intensity of the compressed direct signal across all bistatic images and -50 dB represents the lower bound of the dynamic ranges shown in the bistatic images. The horizontal axis represents the image number. Image number 1-12 represent GPS BIIF-05-30 L5, image number 13-24 and 25-36 represent Galileo GSAT-0205-24 E5a and E5b respectively, image number 37-41 represent Galileo GSAT-0214-05

E5a, and image number 42-46 represent GPS BIIF-07-09 L5. Their relative imaging geometries are listed in Table 4.2. The reason to use image number is that since some images have similar bistatic angle but different azimuth angle or vice versa. As a result, plotting the variation against these parameters individually, its interpretation will be problematic. Instead of those parameters, the image number is used to show variation of echo strength from different observing angles clearly. Specifically, each image number represents individual acquisition geometry (i.e. position of the satellite). It is expressed and distinguished by all three parameters, azimuth, elevation, and bistatic angles (analogous to coordinate systems).

For the variation from the residential tower blocks, as can be seen from Figure 5.6, these variations are not continuous. At specific images (e.g. image number 20), intensities are below the dynamic range, and they thus disappear from the plot, whereas, at other images, strengths can be up to 25 dB. Returns within the dynamic range span approximately 25 dB. Presence of the returns depends on their imaging geometries.

Discontinuity is not only the feature that can be observed from the variation but also a peak. Peaks of between -25 and -27 dB can be observed from image number 16, 28 and 43 and all correspond to the tower 4. For image number 16 and 28, tower 4 was observed by Galileo GSAT-0205-24 satellite with E5a and E5b respectively. The satellite was at 91.66 degrees in azimuth, 52.20 degrees in elevation, and a bistatic angle of 53 degrees. This position is exactly behind the receiver, and the tower 4 is almost in the direct line-of-sight of the receiver. These two factors enabled specular reflections from the tower 4. For image number 43, the high echo strength occurred when GPS BIIF-07-09 satellite was at 155.24 degrees in azimuth and 85.20 degreed in elevation, with a bistatic angle of approximately 88 degrees. This position is not possible to enable specular reflection. As a result, the geometric

perspective cannot be used solely to explain in this case. This indicated that there possibly be the contribution from some more complex scattering mechanism. Relationship between imaging geometry and scattering properties can be further studied to comprehend but this is beyond the scope of this thesis.

The variation trends from image number 13-24 and 25-36 are similar. The reflections can be seen in the first 4-5 images with the substantial peaks from the tower 4 at image number 16 and 28 and then the intensities disappear in the later images. This is because these images were obtained by the same satellite at the same imaging geometries but two different frequencies.

For the tree lines, as shown in Figure 5.7, intensity variations from all eight trees were expressed similarly across all images. They were span within range of approximately 5 dB. It can be considered that their variations practically independent from the bistatic imaging geometry. This is because the major contribution from a tree at L-band comes from its canopies which is more diffuse and isotropic. The experimental campaign was conducted in winter. Although fewer leaves remain than in the summer, its aboveground portion is large, and the trees are densely located to each other.

(a)

(b)

Figure 5.5 Enlargements of Figure 5.2 around (a) area A, (b) area B

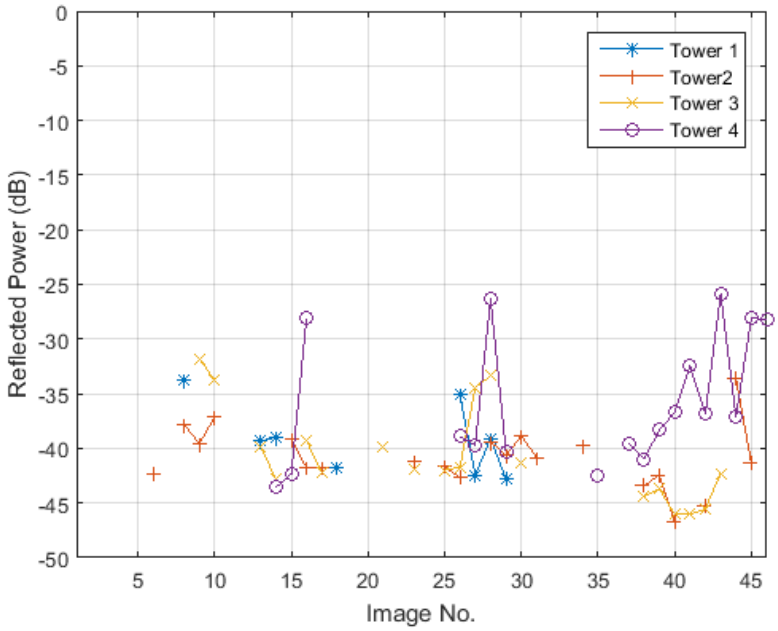

Figure 5.6 Variations in echo strength across forty-six bistatic images for towers in area A

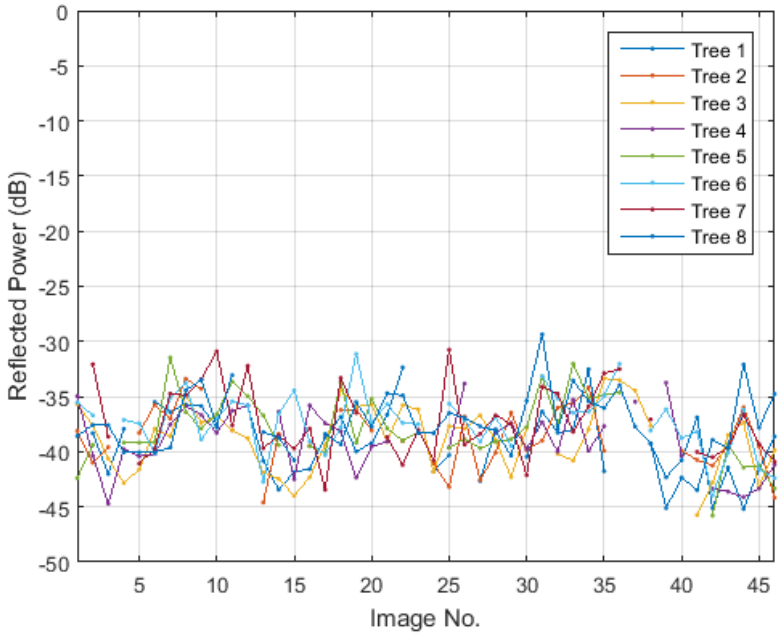

Figure 5.7 Variations in echo strength across forty-six bistatic images for trees in area B

5.10 Discussion

The aim of this chapter is to understand how a multistatic SAR may be able to enhance the information space of a target area over an individual bistatic image. In this chapter, the multistatic image was formed by combining the forty-six experimental bistatic images using the basic non-coherent combination. Those bistatic images were obtained from the GNSS-based SAR system with high spatial diversity of satellite positions. The results show that the obtained multistatic image can enhance the information space of the target area by revealing geometric features of the targets which are edge, shape, and dimensions. This was due to some shadowed area was revealed.

Moreover, combining at the feature level, instead of image level, can distinguish the structural composition of the targets (i.e. tree versus building). The enhanced information, in general, is similar to the output of image segmentation. These features can be used in automatic target recognition. Moreover, capability in distinguishes structural composition can be used in terrain classification.

Among the information as mentioned above, to the best knowledge of the author, multistatic SAR capability to reveal dimensions and distinguish the structural composition of an object has not been publicly reported before whilst identifying edge and shape have been demonstrated in the previous study [37, 39, 80, 81]. All these enhanced information in this thesis were compared to the previous works in three aspects to understanding how multistatic SAR able to enhance information space over the bistatic counterparts. These three aspects are combination method, approach in selecting monostatic/bistatic image to form a multistatic image, and system configuration (active and passive).

In term of combination method, this chapter used the basic non-coherent combination as same as in [37, 39, 80, 81]. For the approach for image selection, this chapter was based on a large set of bistatic images with high spatial diversity and nearly-equal distribution of satellite position. The final aspect is a system configuration, active or passive systems, which causes different image resolution. This aspect compared ability to resolve shadow effect which affects the quality of revealed information from a blocked area.

For edge and shape, despite using the same combination method as in [37, 81], the more prominent edge and shape in this chapter possibly due to using a large set of bistatic images (46 images) with high spatial diversity of satellite position. This approach was demonstrated by simulation in [80] using two bistatic images which contained reflections extensively from the target (which was assumed as a building). Despite the number of the image was small, [80] it produced simulated images so that it yielded a similar effect to the approach used in this chapter. The similar visual quality of edge and shape were also found in [39] where different combination method was used with 26 bistatic images obtained from wide total azimuth angle span of 115 degrees. Therefore, it suggests that the approach in selecting images has more contribution to quality of revealed edge and shape than the combination method.

This aspect is also a major contribution in revealing dimensions and classifying an object. This is because, in general, revealing this two information, requires not only large set of images but also gathering as large as possible set of images with high spatial diversity and appropriate distribution of satellite position. This approach enables as less as possible redundant information within a resultant multistatic image.

In a system configuration aspect, despite modest spatial resolution provided by passive systems in general, high spatial diversity of satellite position can resolve shadow effect and revealed information from previously blocked areas in the individual bistatic images (e.g. lower left part of the target area). In [82, 83], high spatial diversity is also used with 2-4 monostatic and active bistatic images respectively to resolve shadow effect and reveal information from those affected areas. This show that although spatial resolution depends on system configuration, high spatial diversity and appropriate distribution of satellite position can reveal information from the shadowed areas regardless of the system used.

Although high spatial diversity are suggested, effective position of a satellite in multistatic configuration with a fixed receiver, as in this chapter, is limited by the bistatic angle which affects the system spatial resolution. In this configuration, satellites at certain bistatic angles (e.g. opposite to the receiver) provide very low-resolution images and will degrade the overall image quality if they are used. A low-quality image will cause problematic for interpretation and analysis. As a result, some area still unrevealed under this system but it can be resolved using one another receiver at the opposite side of the present receiver.

From the above discussion in three aspects, a framework for non-coherent multistatic SAR can be established. High spatial diversity and appropriate distribution of satellite position are major factors in enhancing geometric features in terms of the number of revealed information and their quality while combination method has a minor effect. This framework can be applied to a multistatic system in general regardless of active or passive configurations.

The large set of bistatic images was used in this chapter, but a lower or upper bound figure has not been investigated. Further study is to find the optimum number of bistatic images. The optimum might be in terms of the angular separation between satellites. It is because a

vast number of images in a certain range of satellite position may not increase information effectively since they contain a high amount of redundant. However, a number of images possibly depends on the complexity of an area and vary from area to area. Therefore, the further study should include investigating an optimum number of images for a different type of target areas. The optimum number of images used can then be further derived optimum transmitter separation and bistatic angle. Such information can be used as criteria to automatically select a pair of TX-RX in the case that constant stream of data from many different geometries.

5.11 Summary

In this chapter, the potential of a passive non-coherent multistatic SAR employing the navigation satellites as the transmitters has been investigated. Signals from four different GNSS satellites that reflected off the real target area were collected simultaneously and then processed into bistatic images. A set of forty-six experimental bistatic results have been obtained and combined by basic non-coherent combination to form a multistatic SAR image. The non-coherent combination was done by adding the absolute value of their corresponding bistatic images in a pixel-by-pixel basis.

The results showed that such non-coherent multistatic SAR provides a considerably superior object detection performance as well as the ability to reveal the object geometric features, such as edges, shapes, and dimensions. In addition, information obtained from individual bistatic images can be combined and used to classify composition of the target whether it is a tree or building. These results can be considered as a baseline for providing high-quality images by using more advanced processing techniques.

Chapter 6

Coherent Multistatic SAR

6.1 Introduction

The coherent combination can enable substantial spatial resolution improvement to a multistatic SAR image compared to a bistatic counterpart. This technique benefits the modest resolution passive SAR system. The understanding gained in the experiment was ultimately aimed to establish a framework for coherent multistatic SAR image formation.

This chapter presents experimental results of coherent multistatic SAR experiment. The experiment was conducted using the GNSS-based SAR system with basic multistatic configuration. In the basic configuration, two transmitters and a receiver were used. Two separate apertures were synthesised by collecting signals from the same satellite at two different time slots. These two apertures were chosen using k-space support to analyse their mutual coherence. Although they had a gap between them in the k-space domain, it was shown later that the gap was sufficiently small to maintain coherence and enable successful combination.

The technique was first applied to a point-like target. The experimental point-spread functions (PSF) both bistatic and coherent multistatic were compared their spatial resolution. Furthermore, the experimental multistatic was compared to its theoretical expectation PSF.

Then the technique was applied to the real target area. Experiment PSFs of three objects across the area from both bistatic and multistatic were extracted and compared.

6.2 Coherent Combination

In this chapter, the multistatic image was formed basic coherent combination by adding complex bistatic image pixels in a pixel-by-pixel basis. The basic coherent combination can be express as

$$I_M = \frac{1}{N}\left|\sum_{i=1}^{N} I_i\right|, \tag{6.1}$$

where I_M is a multistatic image, I_i is an i^{th} bistatic image, $|\cdot|$ is absolute operator, and N is a total number of bistatic images used in the combination. In contrast to non-coherent technique, coherence between bistatic image had to be considered to obtain successful coherent combination.

6.3 K-space Support

Coherent combination for mulstistatic SAR involves considering scattering and transmitter (i.e. signal) coherences. For the former case, it requires proximity between transmitters to maintain scattering coherence from different viewing angles. This is a major limiting factor in the passive multistatic SAR system since the transmitter trajectories are uncontrollable to satisfy the condition. In this paper, this kind of coherence is beyond the scope of the paper and was assumed that the condition for scattering coherence was met.

For the latter case, this coherence considers the spatial location of the signal for a given transmitter and target. In active system, signal coherence between transmitters can be maintained by placing the transmitting platform in close proximity positions. This concept

has been proposed, e.g. in [49], with a high possibility of having signal coherence using one satellite with an onboard transmitter and multiple receive-only satellites follow the transmitting satellite on the same orbit. For a passive system, maintaining signal coherence between platforms is challenging since the orbit or trajectory of transmitters cannot be controlled. However, the transmitted signal can be analysed whether they have the possibility of having coherence using k-space. If high coherence between signals exists, they can be used in coherent combination.

The requirement on coherency between signals is that phase of these signal must be kept in-phase. In the case of target scattering coherence, the phase can be maintained by using transmitters that are proximity to each other so that echoes from the target are not fluctuated, and consequently, the phase can be kept in-phase. In case of signal coherence, despite phase are unknown at the transmit, common clock receiver and synchronisation algorithm can be used to obtain phase information at receiving.

Signal coherence can be determined in the spatial frequency domain, i.e. k-space. This domain transforms a signal into its corresponding k-space support extent whose shape and location are determined by transmitting carrier frequency and bandwidth, and angular distance of platforms. K-space can be used to predict transmitter coherence. Two or more signal is more coherent when their k-space support extents are adjacent. In this case, the individual shorter extent can form a wider k-space support extent. A wider resultant k-space support indicates higher possibility in refining spatial resolution of a combined image possibly both in range and cross-range.

6.3.1 Monostatic SAR Configuration

In the monostatic configuration, where a transmitter and a receiver are co-located (i.e. zero angular distance between them), signal travels cover a round trip to an arbitrary given target, and its samples are at a distance from the target in a spatial frequency domain of $2k = 4\pi f_c/c$, where $k = 2\pi f_c/c$ is a wavenumber, f_c is a carrier frequency and c is the speed of light. If a target is assumed at the origin and a platform moves over azimuth angle of 360˚ (Figure 6.1), signal samples will trace circular k-space support whose centre point is at origin and radius is $2k$ (Figure 6.2 (a)). From [61], its components in k_x and k_y axes are expressed as

$$k_x = 2kcos(\theta), \tag{6.2}$$

$$k_y = 2ksin(\theta). \tag{6.3}$$

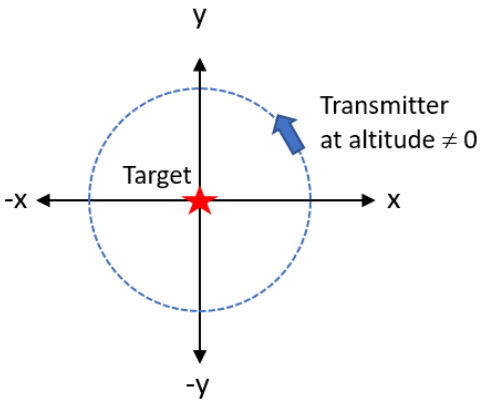

Figure 6.1 Monostatic SAR geometry where the transmitter has a circular flight path of 360˚

6.3.2 Bistatic SAR Configuration

For a bistatic case, the angular distance between platforms are considered, and the signal travels in the direction of the bisector. Therefore, as transformed from polar format derived in [84] into the Cartesian grid, the location of a signal sample considers a transmitter and receiver and is expressed as

$$2kcos(\tfrac{\theta_T-\theta_R}{2}) = (4\pi f_c/c)cos(\tfrac{\theta_T-\theta_R}{2}), \tag{6.4}$$

where θ_T is the azimuth angle of a transmitter, θ_R is the azimuth angle of a receiver and $(\theta_T - \theta_R)$ is a bistatic angle. In this case, each component in k_x and k_y axes are described as

$$k_x = 2kcos\left(\tfrac{\theta_T-\theta_R}{2}\right) cos\left(\tfrac{\theta_T+\theta_R}{2}\right)$$

$$= k(cos\theta_T + cos\theta_R), \tag{6.5}$$

$$k_y = 2kcos\left(\tfrac{\theta_T-\theta_R}{2}\right) \sin\left(\tfrac{\theta_T+\theta_R}{2}\right)$$

$$= k(sin\theta_T + sin\theta_R). \tag{6.6}$$

K-space support for general bistatic is shown in Figure 6.2 (b) where each circle represents a case when the transmitter moves with an angular position of a receiver (solid red line). When a receiver moves to another position, the new circle will be formed as seen as a dashed red line. The orientation of a circle in bistatic depends on a transmitter and a receiver positions. Comparing k-space from monostatic and general bistatic, k-space support changes from a circle whose centre point is at the origin to a circle that pass the origin.

In the bistatic case with a receiver is fixed as in the GNSS-based SAR, if a receiver is assumed at 0˚, as same as those in [85], and Eq. 6.5-6.6 are then

$$k_x = k(cos\theta_T + 1), \tag{6.7}$$

$$k_y = ksin\theta_T, \tag{6.8}$$

and the k-space support will be a solid-line circle in Figure 6.2 (b).

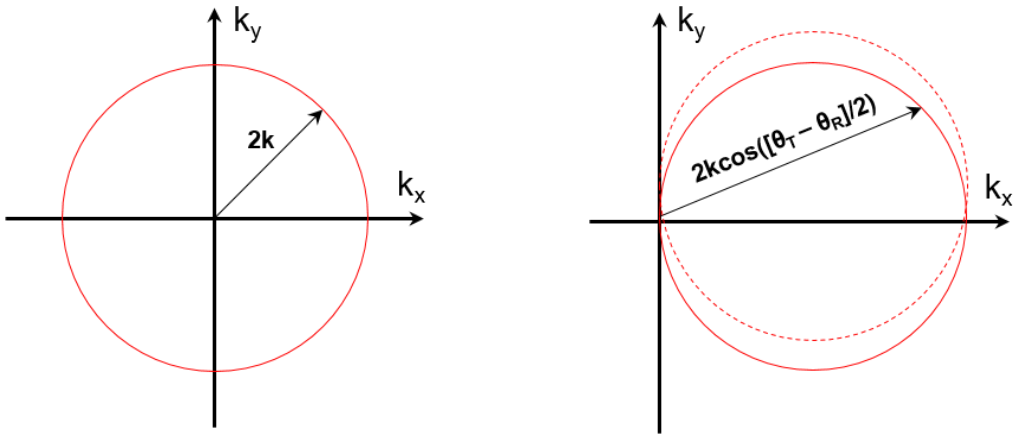

(a) (b)

Figure 6.2 K-space support for (a) monostatic and (b) general bistatic configurations

6.3.3 Coherent Multistatic GNSS-based SAR

Multistatic configuration can be considered as a combination of multiple bistatic pairs. Multistatic configuration of GNSS-based SAR, where M multiple satellites and a fixed receiver are employed. Each m^{th} a satellite moves along a trajectory with an azimuth angle of θ_{Tm} whereas the angular position of the fixed receiver, θ_R, is defined at 0˚ relative to the x-axis (Figure 6.3). Satellite use ranging code with bandwidth, B. For any given target, components of k-space support for each transmitter-receiver pair are determined, based on [31], by

$$k_x = \frac{2\pi(f_c+f_b)}{c} \times \left(cos\left(\theta_{Tm,k}\right) + 1\right), \tag{6.9}$$

$$k_y = \frac{2\pi(f_c+f_b)}{c} \times sin\left(\theta_{Tm,k}\right), \tag{6.10}$$

where $\theta_{Tm,k}$ is k^{th} azimuth position of the m^{th} satellite, f_c is a carrier frequency, and f_b is a b^{th} frequency in the range of bandwidth of the ranging code. In this case, where narrow bandwidth is used, if the transmitter span in a narrow range, k-space support extent will be shaped as a rectangular.

The example of k-space from this case, where two satellites are spatially separate and transmit the same carrier frequency, is shown in Figure 6.4. As the bandwidth used is narrow and the transmitter span within sufficiently narrow. Therefore, their k-space supports, one on the lower-left corner and another one on the upper right corner, has a rectangular shape as anticipated and have a gap between them. The two regions can move toward each other when they move closer in azimuth position. Size of a gap proportionally affects the possibility of having coherence. Although the platforms are at different positions, their k-space supports are laid on the same circle as they employ the same carrier frequency and same fixed receiver. When they move closer to each other, their k-space support will also be moved towards each other and the possibility of having signal coherence will be increased. Choosing appropriate two or more signals whose k-pace are adjacent so that having high coherence can enable successful coherent combination.

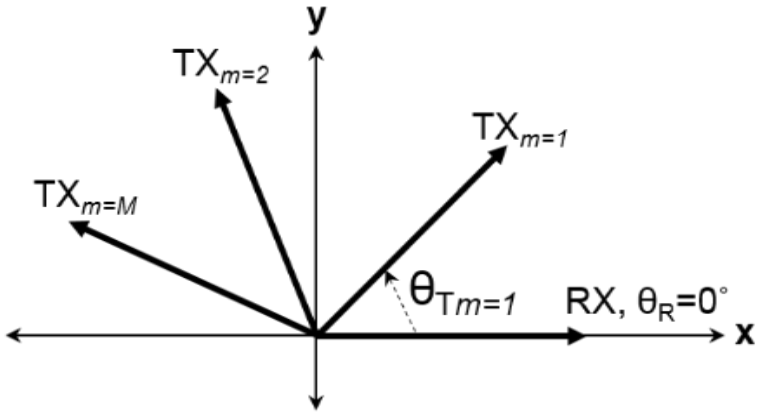

Figure 6.3 The multistatic GNSS-based SAR imaging geometry

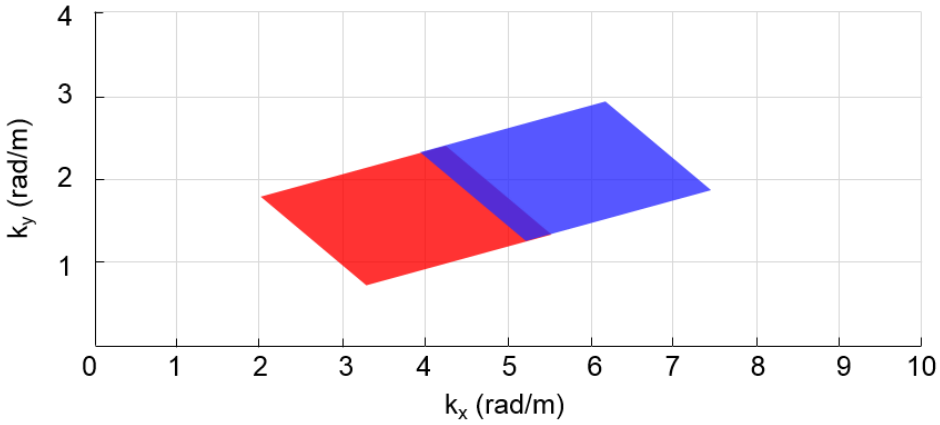

Figure 6.4 GNSS-based multistatic SAR k-space supports of the two datasets

6.4 Coherency in Passive Multistatic Imaging

Coherence is an ability to maintain a phase relationship between signals. In other words, the phase information of the signals must be known. In multistatic imaging, the target is being illuminated by different opportunistic illuminators from different aspect angles. Coherency in such configuration may be affected by transmitting signals from the illuminator and target scattering. For the former source, since the illuminators in passive operation is not possible

to be controlled; therefore, it is difficult to synchronise or phase lock the signals at the output of the transmitters.

Consequently, knowledge of the phase of the transmitting signal at the output of the illuminator is not possible to obtain. As a result, it is difficult to maintain coherent of the illuminator at transmitting. Although coherency at the transmitter is not feasible for passive operation, it can be realised as coherent-on-receive using a common clock for all receive channels so that receiving artefacts are common to all signals. This thesis also used a single receiver to realise a common clock. Subsequently, the synchronisation algorithm with the information on the structure of the signal being transmitted is used to extracted phase delay from the received direct signal. In such a method, the phase at the output of the transmitter is assumed to be zero delays. This phase delay is later used for correcting reflected signal in the subsequent process. This coherence condition is referred hereafter as signal coherent.

For the latter cause, the phase is also affected when the signal scattered by the target. Signal scattered by a target whose dimensions are much larger than the wavelength of the transmitting signal may be considered as a sum of partial signal scattered by multiple scattering centres of the target [86]. Change in observed angle will lead to a significant change in distance, as compared to the wavelength of the transmitting signal, from different scattering centres to illuminators and receivers and hence cause acute phase responses. This response results in complex amplitude fluctuation of the total return from the target. In this thesis, this condition assumed to be met from the fact that GNSS constellations have many satellites illuminating the same area simultaneously (six to eight satellite per each constellation) at any time and anywhere on the Earth surface. The multitude of the satellites allows choosing two different satellites with the sum of their aperture synthesis span within

10° can be realised. This restricted angular spanning within this range can remain the scattering centres locations' and phase response approximately constant [47], and enhance target coherence can be maintained. This coherence condition is referred hereafter as target scattering coherent.

6.5 Coherent Multistatic SAR Experiment

The experimental bistatic point-spread functions (BPSF) of the point-like target were obtained from the direct signal received by the HC antenna. These BPSFs were then coherently combined into the coherent multistatic point-spread functions (MPSF). Both types of PSFs have compared their spatial resolution in both range and cross-range direction. Theoretical BPSF and coherent MPSF were also obtained for visual comparison with the experimental counterparts. For the theoretical coherent MPSF, instead of using two theoretical BPSFs, it was obtained using coherent integration time that covers the start of dwell time on target of the first BPSF until the end of dwell time on target of the second BPSF. Principally, this yields the same effect as a coherent combination but without a gap.

For the real target area, the radar images were obtained using signals captured by the RC antenna. The same principle as in the point-like target case was applied to produce the coherent multistatic SAR image. The experimental bistatic and multistatic images were compared, then experimental PSFs were chosen from three areas across the target area. Their spatial resolutions were compared in both range and cross-range directions.

Procedures to conduct this experiment were summarised as follows.

Step 1) Performed image formation to obtain bistatic point spread function and SAR images

Step 2) Performed a coherent combination to form coherent multistatic PSF and image

6.6 K-space Support Analysis

As previously mentioned, k-space support can be used to analyse signal coherence. In this section, a method to analyse coherence between signals was shown. This was used to identify appropriate signals that having coherence possibility. From all the signals acquired in the experimental campaign, the candidate signal was L5 signal from GPS BIIF-05-30 recorded between 09:45-10:15 am. The parameters of the two datasets are listed in Table 6.1. Their k-space support can be plotted as in Figure 6.5 to show their suitability for using in coherent combination. Although two k-space extends do not overlap, they still have coherency between them. The level of their coherency is discussed in the discussion of this chapter. The individual k-space extend of the acquisition 1 are represented in red whilst the acquisition 2 are represented in blue. It can be seen that the k-space support of the acquisition 1 is slightly shorter by 0.47˚ than the acquisition 2 due to their unequal azimuth span despite both were recorded for 10 minutes.

Table 6.1 Parameters for calculating k-space support

Parameter	**Value**
Satellite	GPS BIIF-05-30
Carrier Frequency	1176.45 MHz
Ranging code bandwidth	10.23 MHz
Dwell time on target	10 min (with 5 min gap)
Acquisition 1 Azimuth	171.622˚-172.647˚
Acquisition 1 Elevation	34.340˚-39.056˚
Acquisition 2 Azimuth	169.668˚-171.166˚
Acquisition 2 Elevation	41.432˚-46.205˚

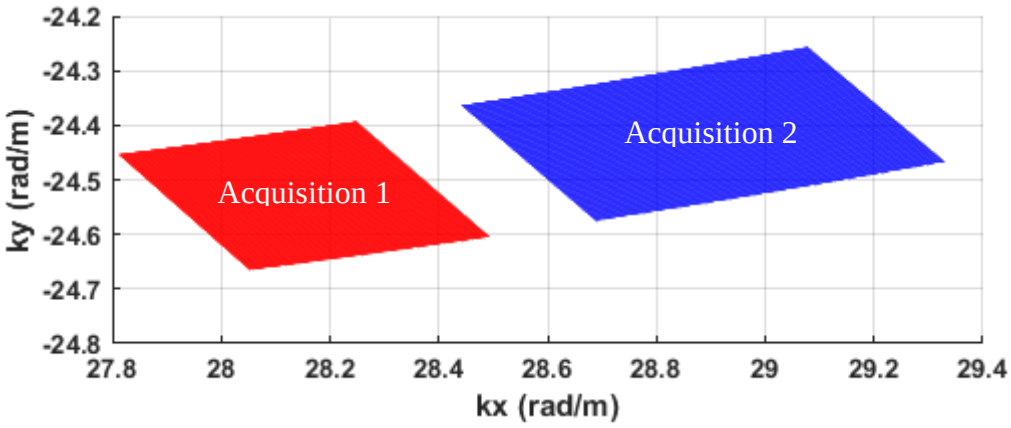

Figure 6.5 K-space support obtained from the two datasets which their satellites were vicinity

6.7 Point-like Target

The combination technique was validated using point-like target by obtaining their corresponding experimental PSFs, and the results are shown in Figure 6.6. Figure 6.6 (a)-(b) shows the experimental bistatic PSFs of a point-like target obtained from the datasets that recorded using heterodyne channel (HC) antenna. Both PSFs were similar in orientation due to the positions of the satellite were different within a narrow range, approximately 0.5˚ in azimuth. As a result, both PSFs had a similar spatial resolution, as shown in Table 6.2, which are 3-4 m in cross-range and 17-19 m in range. The range is the distance from the receiver located at the origin and cross-range is a direction perpendicular to range direction. After applying the coherent combination, main lobe of the MPSF is narrower than the BPSFs, hence spatial resolution improved.

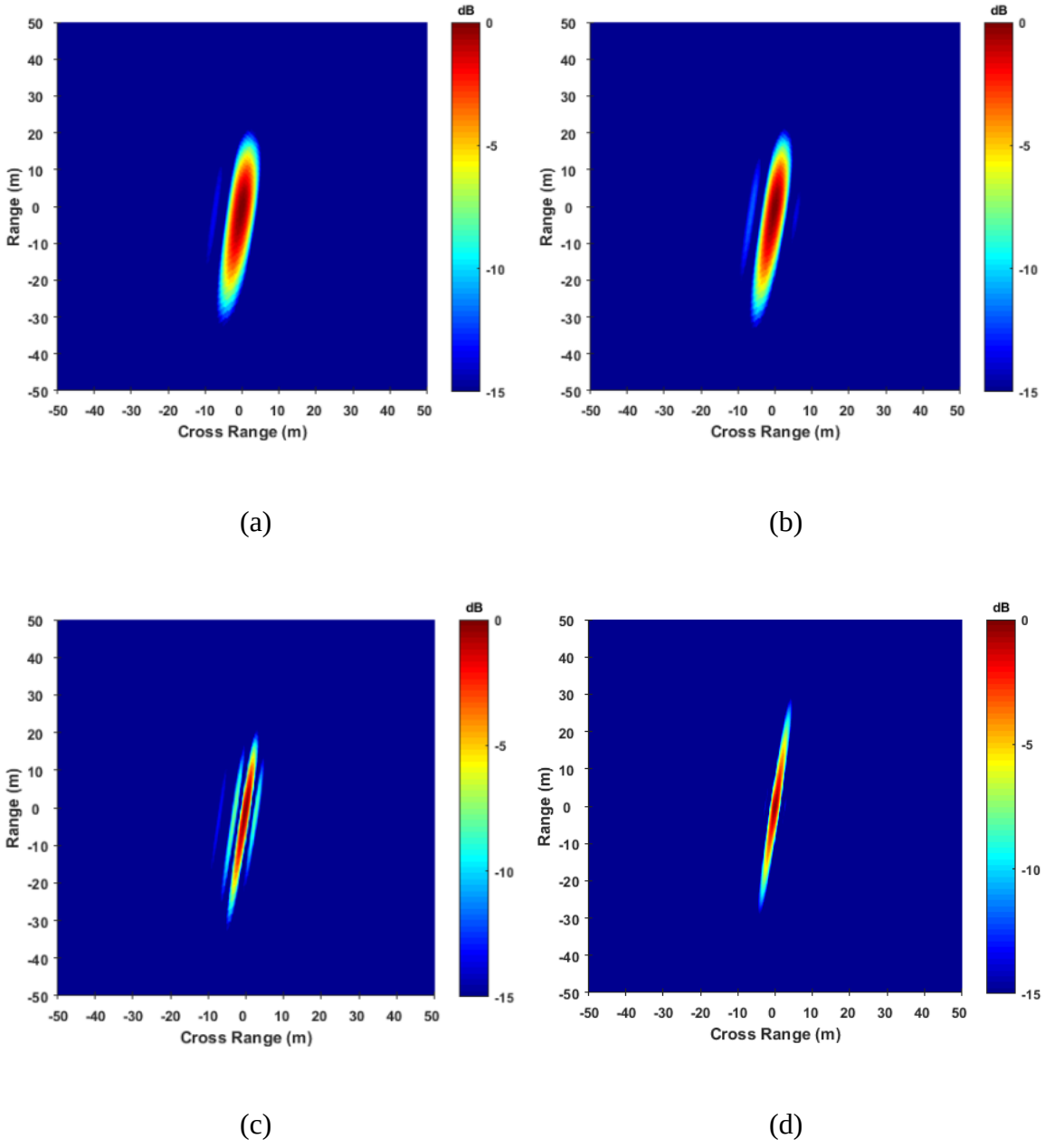

Figure 6.6 Experimental PSFs (a) BPSF 1 (b) BPSF 2 and (c) experimental coherent MPSF (d) theoretical coherent MPSF

Figure 6.6 (c) shows the experimental coherent multistatic PSF (MPSF) obtained by coherently combining the aforementioned bistatic PSFs. A theoretical coherent MPSF counterpart, shown in Figure 6.6 (d), was also obtained for comparison purposes. The theoretical coherent MPSF was obtain using coherent integration that covered dwell time on target from the start of acquisition 1 until the end of acquisition 2 without the gap. In other words, entire signal covered that period was used. As a result, the signal has no phase discontinuity. Therefore, sidelobe can be kept lower than the experimental case. Theoretically, this method is the same as using a coherent combination using two bistatic PSFs. Both theoretical and experimental coherent multistatic PSFs were further compared, as shown in Figure 6.7. Overall, both were in good agreement. It is seen that they had a similar size. Sidelobe level of the experimental MPSF was noticeable and higher than the theoretical MPSF (see Figure 6.7). This was expected due to the gap in the experimental MPSF that affects the coherency and hence sidelobe level. However, the gap size was sufficiently small. Thus coherency was still maintained.

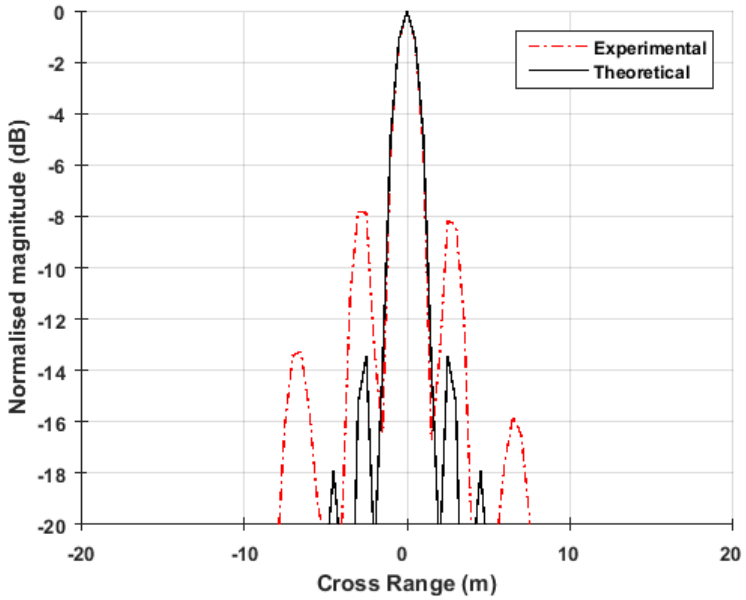

(a)

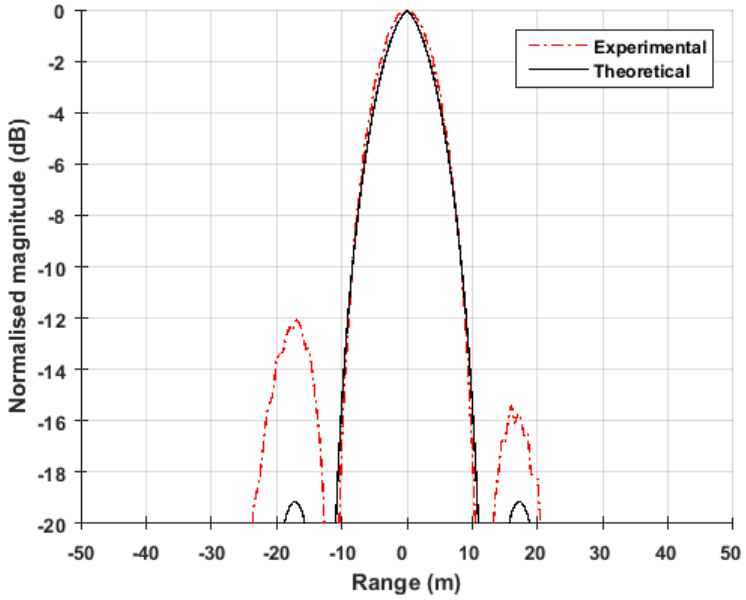

(b)

Figure 6.7 Comparison between the experimental coherent multistatic PSF and its theoretical PSF in (a) cross-range and (b) range

Comparing the experimental coherent MPSF (Figure 6.6 (c)) to the two BPSF (Figure 6.6 (a)-(b)), it can be seen that the multistatic PSF was much narrower than the individual bistatic PSFs. Details of this comparisons are shown in Figure 6.8. From Figure 6.8, cross-sectional plots in cross-range and range show comparison between these PSFs, where red, black, and blue lines represent BPSF 1, BPSF 2, and coherent MPSF, respectively. The narrower main lobe is prominent with the blue lines. This confirms the improvement of spatial resolution in the multistatic image. The details of quantitative comparison are shown in Table 6.2, which the multistatic is improved by a factor of two. This is due to that coherent combination of multiple bistatic apertures will form a single effective multistatic synthetic aperture which its angular span is a total sum of those individuals and improvement is equal to the length of the multistatic over the individuals [42]. As a result, in our case, the effective synthetic aperture of the multistatic results which formed by two bistatic apertures is approximately twice larger than that of the individual bistatic counterparts. Another observation is that the amount of improvement in the multistatic case is consistent with the size of the total k-space extent relative to individual extents. The spatial resolution also improved in both range and cross-range directions as similar manner as of the total k-space support (Figure 6.5) which extends in both $k_x$and k_y directions. However, this observed consistent might or might not have any linkage between them. It can be included in future work.

Also, slightly high sidelobes can be seen in the resultant coherent multistatic PSF, and this was expected due to a small gap. In this case, the sidelobes level is below -7 dB in the cross-range and below -12 dB in the range which is still deemed practical. As a result, this confirms that, at the system level, a coherent combination using the system is possible and enable finer spatial resolution.

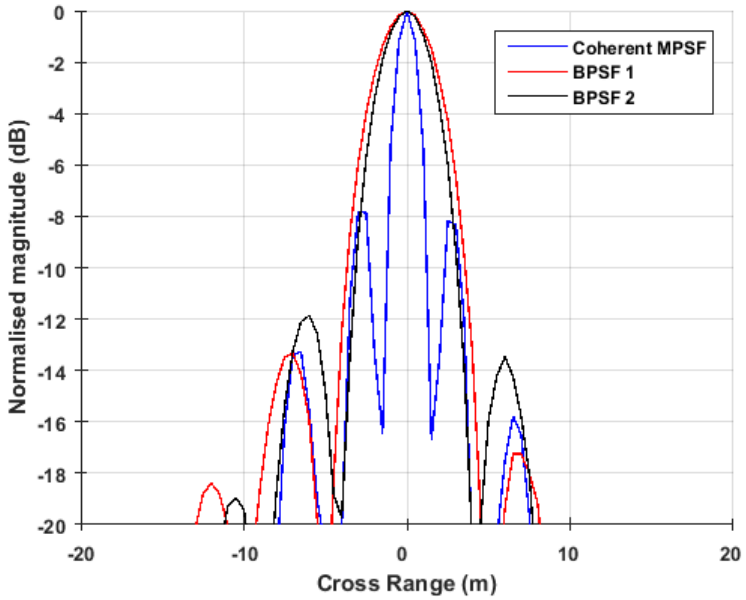

(a)

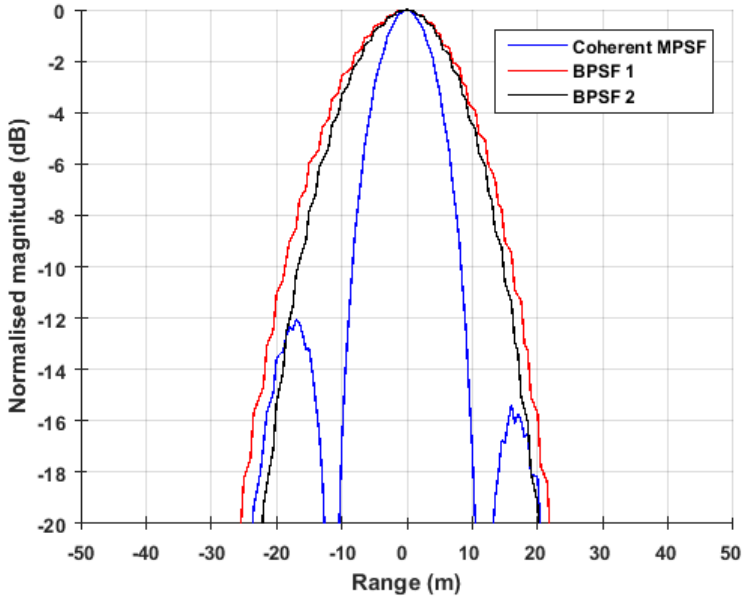

(b)

Figure 6.8 Comparison between the coherent multistatic PSF and the individual bistatic PSFs in (a) cross-range and (b) range

Table 6.2 Spatial resolution comparison between the two bistatic and multistatic PSFs

PSF	Cross-range (m)	Range (m)
BPSF 1	4.281	19.343
BPSF 2	3.656	17.406
Coherent MPSF	1.437	9.875

6.8 Real Target Area

In this section, the same method and was applied to the real target area to evaluate whether an improvement still valid at the image level. The bistatic images of the real target area were obtained from the dataset that captured from the radar channel of the receiver. These datasets contain signals reflected off the real target area in Figure 4.4 in Chapter 4. They were then processed into bistatic images using the same algorithms as in the case of the point-like target datasets. Figure 6.9 (a)-(b) shows the obtained experimental bistatic images.

Visually, the appearance of echoes in both images is in a similar pattern, which is due to the similarity of their imaging geometries, as same as in the point-like target case. The tree lines in the middle of the scene (between 50-200 m cross-range) are prominently spotted in both images. This is expected because their scattering properties allow them to be visible with similar echo strength in most of the observation angles [25]. In contrast, this is not always the case for buildings, e.g. residence tower blocks at the far end or complex buildings at the bottom left of the scene. Scattering properties is the key factor in affecting this type of object, which raises difficulty in identifying them in some viewing angles.

These bistatic images were then formed a multistatic image using the coherent combination. Figure 6.9 (c) shows the obtained coherent multistatic image. Comparing the bistatic and multistatic, it is seen that the multistatic image is visually similar to the bistatic images in term of the appearance of returns. This is due to the similarity of the bistatic images that do

not enhance much different information about the target area in term of the identified target. However, it can be seen that PSFs in the coherent multistatic image are much narrower than those in the bistatic images. The examples of the comparison are shown in Figure 6.10, Figure 6.12 and Figure 6.14, which are the enlargement of parts across the images from the tree lines, the women's hospital and the left-most residence tower block (the area B, C, and A from Figure 4.4, respectively). Their location in the local coordinate is shown in Table 6.3.

Quantitative investigation of spatial resolution used the experimental PSFs extracted from the enlargement images to analyse spatial resolution. In this case, a distinct PSF in each enlargement image was selected (marked by the red arrow). These selected PSFs came from the proximity area in each set of enlargement image so that bistatic angles were less varied and approximately fixed. Their cross-sectional profiles in both range and cross-range are shown in Figure 6.11, Figure 6.13 and Figure 6.15. Scattering centre of the PSFs was marked with a red arrow. Their resolution was evaluated at -3dB from the peak of the PSF's main lobe and compared to each other. Results of the quantitative analysis were shown in Table 6.4 to Table 6.6. Spatial resolutions from all target areas were improved in the coherent multistatic image compared to a single bistatic image.

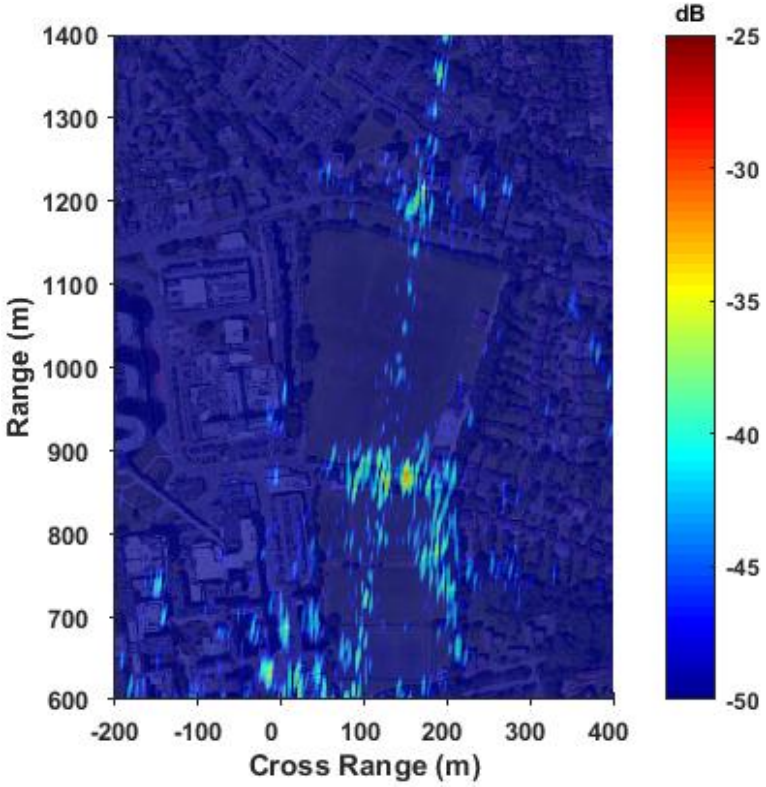
dB
-25
-30
-35
-40
-45
-50
1400
1300
1200
1100
1000
900
800
700
600
Range (m)
-200
-100
0
100
200
300
400
Cross Range (m)

(a)

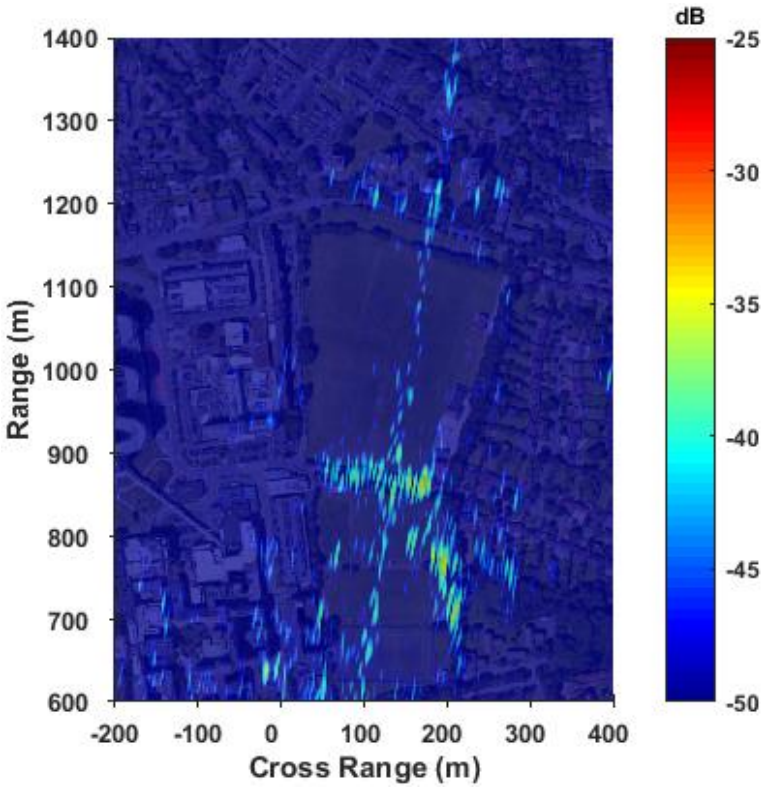
dB
-25
-30
-35
-40
-45
-50
1400
1300
1200
1100
1000
900
800
700
600
Range (m)
-200
-100
0
100
200
300
400
Cross Range (m)

(b)

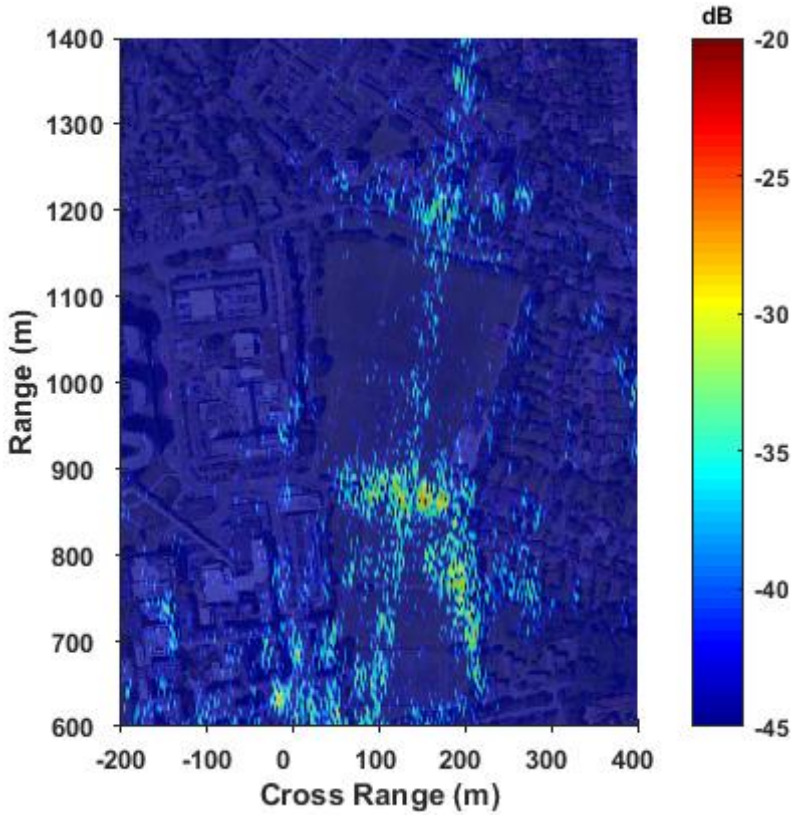

(c)

Figure 6.9 Experimental images (a) bistatic image 1 (b) bistatic image 2 and (c) coherent multistatic image

Table 6.3 Location of the chosen experimental PSFs in terms of cross-range and range

Images	Tree Line	Women's Hospital	Left-most Tower
Bistatic 1	(+150,870)	(+4,973)	(+56,1236)
Bistatic 2	(+171,865)	(-3,972)	(+60,1232)
Coherent Multistatic	(+171,868)	(-4,971)	(+57,1234)

It is seen that the spatial resolution of the experimental PSFs from the images are similar to those from the point-like target (i.e. system PSF). Spatial resolutions were refined in the same trend (see Table 6.2 and Table 6.4 to Table 6.6), that in the same direction they are approximately in the same order. Slightly differences are caused by location of the target from the receiver that governs the size of PSF. This also confirms the possibility of coherent

combination using the GNSS-based system that can enable finer spatial resolution of the multistatic image than the individual bistatic.

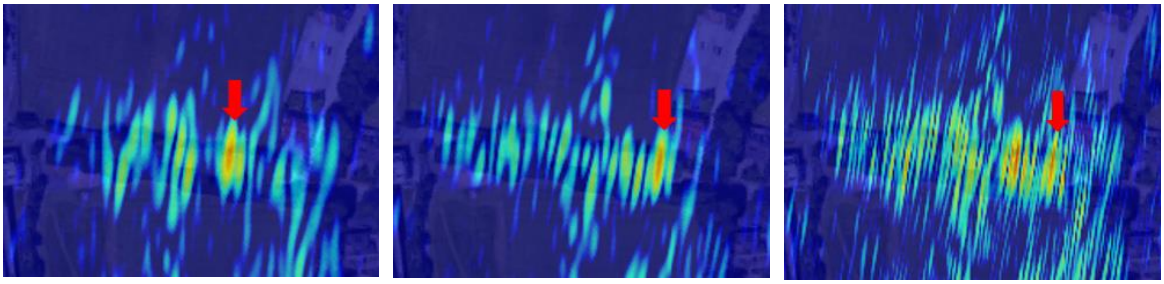

(a) (b) (c)

Figure 6.10 Enlargement of the tree lines from (a) bistatic image 1 (b) bistatic image 2 and (c) coherent multistatic image

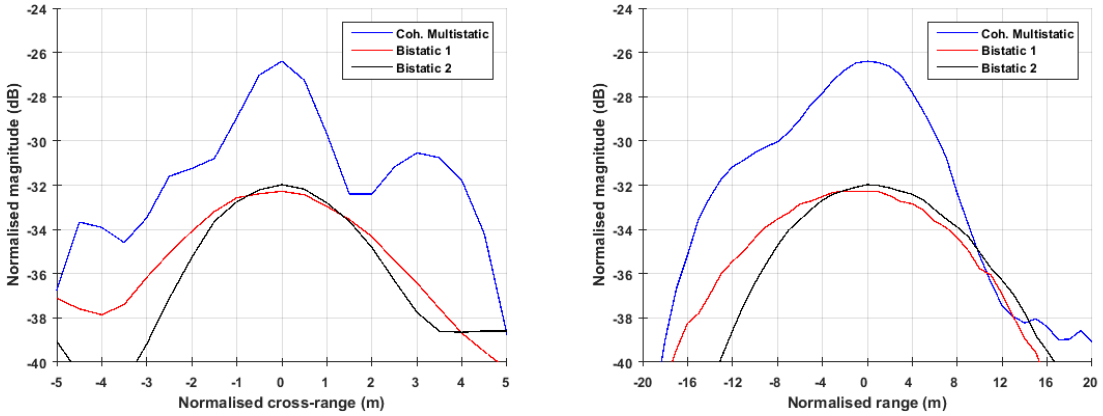

(a) (b)

Figure 6.11 Comparison of cross-sectional profiles in (a) cross range and (b) range directions using PSFs extracted from the tree line

(a) (b) (c)

Figure 6.12 Enlargement of the women's hospital building from (a) bistatic image 1 (b) bistatic image 2 and (c) coherent multistatic image

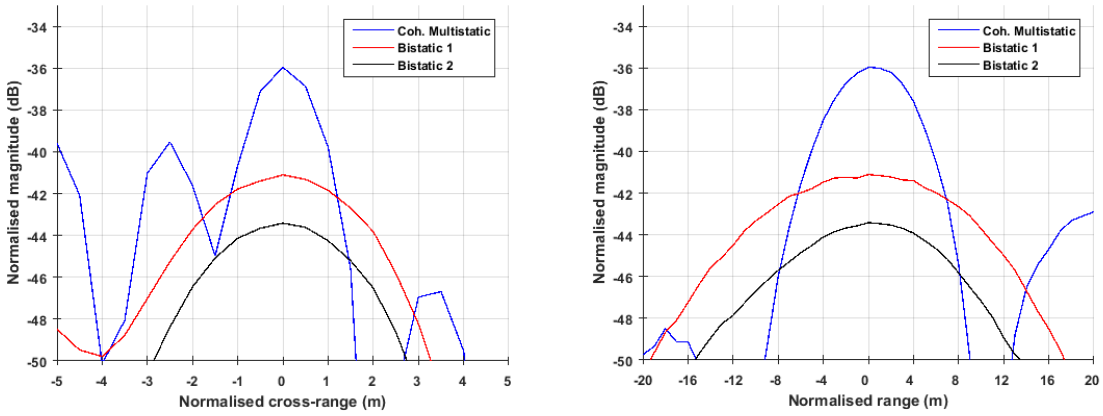

(a) (b)

Figure 6.13 Comparison of cross-sectional profiles in (a) cross range and (b) range directions using PSFs extracted from the women's hospital building

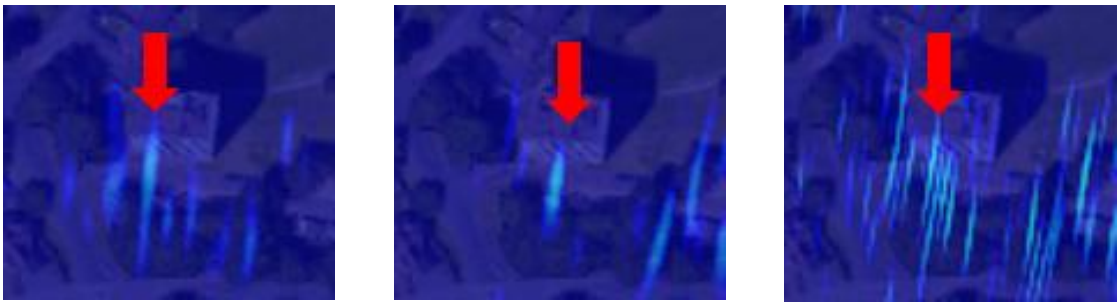

(a) (b) (c)

Figure 6.14 Enlargement of the leftmost residence tower block from (a) bistatic image 1 (b) bistatic image 2 and (c) coherent multistatic image

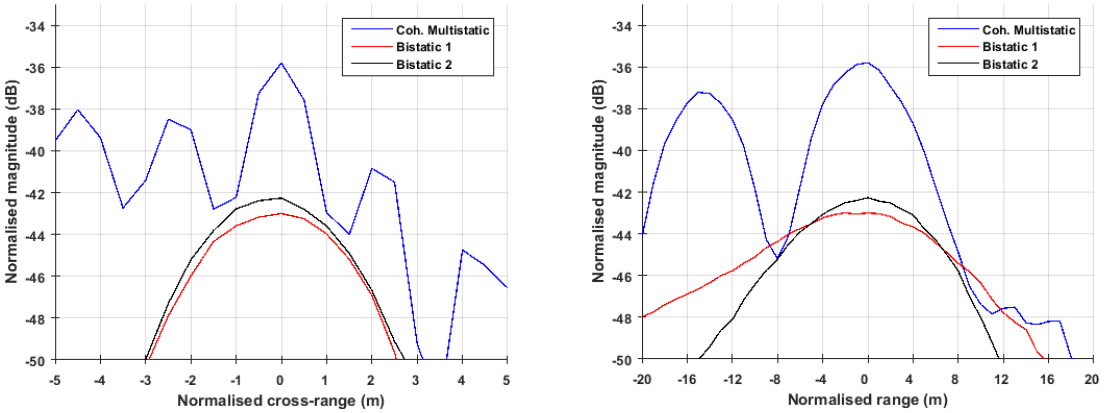

(a) (b)

Figure 6.15 Comparison of cross-sectional profiles in (a) cross range and (b) range directions using PSFs extracted from the leftmost residence tower block

Table 6.4 Comparison of spatial resolution between the two bistatic and multistatic images using PSFs extracted from the tree line

Image	Cross-range (m)	Range (m)	Intensity (dB)
Bistatic 1	5.03	21.02	-32.28
Bistatic 2	3.96	18.21	-31.98
Coherent Multistatic	2.06	12.37	-26.40

Table 6.5 Comparison of spatial resolution between the two bistatic and multistatic images using PSFs extracted from the women's hospital building

Image	Cross-range (m)	Range (m)	Intensity (dB)
Bistatic 1	4.19	22.03	-41.11
Bistatic 2	3.95	18.29	-43.42
Coherent Multistatic	1.62	9.36	-35.97

Table 6.6 Comparison of spatial resolution between the two bistatic and multistatic images using PSFs extracted from the leftmost residence tower block

Image	Cross-range (m)	Range (m)	Intensity (dB)
Bistatic 1	3.74	22.31	-43.00
Bistatic 2	3.61	15.42	-42.26
Coherent Multistatic	1.27	8.69	-35.80

6.9 Power Budget Improvement

Overall, the multistatic image has higher power than the bistatic images. This is due to the improvement of the power budget that enables better visibility of the targets. Table 6.7 show details of the comparison. The intensities were taken from the scattering centres used in the previous section. Not only enabling finer spatial resolution, but the coherent multistatic results can also improve the power budget by approximately 6 dB improvement over the bistatic counterpart. This is due to the combination is equal to the twice coherent integration

time of the individual bistatic images. The total k-space support was approximately twice larger than the individual extents. As a result, this doubled extents yielded 6 dB higher, as expected from dB scale conversion.

Table 6.7 Comparison of the intensity of the experimental PSFs from three areas

Image	**Intensities (dB)**		
	Treeline	**Women's Hospital**	**Left-most Tower Block**
Bistatic 1	-32.28	-41.11	-43.00
Bistatic 2	-31.98	-43.42	-42.26
Coherent Multistatic	-26.40	-35.97	-35.80

6.10 Preliminary Analysis of Spatial Resolution using K-space Support

Results shown in section 6.6 and 6.7 can be observed that the improvement of resolution in multistatic case enables up to approximately doubling the bistatic counterparts and consistent with the size of the total k-space extent relative to individual extents. This consistent may have relationship or linkage between the size of the total k-space and amount of improvement. In this section, this relationship has been initially investigated.

In this preliminary analysis, spatial resolution was determined using k-space support to investigate whether it can be predicted using k-space support. If k-space support can predict spatial resolution, this resolution can serve as a theoretical expectation of a coherent multistatic image. K-space spatial resolution was determined using inverse values of the different in k_x and k_y directions [87]. The values of k_x and k_y were taken from corners of the k-space support, both the individuals and the total extend. The obtained spatial resolutions are shown in Table 6.8.

From Table 6.8, despite values of the resolutions determined from k-space support are different from the experimental, they have a similar trend of improvement from bistatic to multisatic case. Resolution in k_y is more closer to the cross-range whilst resolution in k_x is more closer to the range direction. Differentiate in value would come from that the experimental range and cross-range were determined from the local coordinate where the receiver was at the origin, they are possibly not exactly to the k_x and k_y axes of the k-space support. Therefore, further investigation can be included as future work.

Table 6.8 Comparison between spatial resolutions determined from k-space support and the experimental PSFs

PSF	**k-space, k_y (m)**	**k-space, k_x (m)**	**Experimental Cross-range (m)**	**Experimental Range (m)**
BPSF 1	9.239	22.439	4.281	19.343
BPSF 2	7.059	19.634	3.656	17.406
Coherent MPSF	4.133	15.320	1.437	9.875

6.11 Discussion

This chapter presented the experiment to experimentally demonstrate the concept of coherent multistatic SAR. It was ultimately aimed to establish a framework for coherent multistatic SAR image formation. The experiment used a basic multistatic configuration using two different satellites and a single fixed receiver with a point-like target and a real target area. The results show promising spatial resolution improvement over the bistatic counterpart, in both point-spread function and SAR image level, at least approximately by a factor of two. In addition, a power budget of the coherent multistatic image results was found twice higher than the bistatic images.

Theoretically, spatial resolution in a multistatic image is finer than a bistatic image due to the better target localisation using multiple aspects images. Incorporating coherent

techniques to multistatic SAR system, substantial spatial resolution improvement can be expected. Number of works on this technique under laboratory conditions and at a simulation level have been presented [42, 44-49]. All works showed similarly promising results. These results are consistent with the results presented in this chapter in term of improved spatial resolution. However, in this chapter results, a power budget of the multistatic image was further found that it was improved up to twice than the bistatic images. This was possibly due to combining two bistatic images that have a high possibility of having coherence was equivalent to coherent integration to form a single bistatic image.

The present results showed successful coherent combination to form the coherent multistatic SAR image. To establish the framework, coherence was considered to gain an understanding of how coherence was maintained. Specifically, how transmitters and receivers were configured to obtain coherence conditions. Coherence is essential for successful coherent combination. In this thesis, the condition for scattering coherence was assumed that it was met. Only signal coherence was analysed using k-space support to choose candidate signals appropriately. For target scattering, transmitters have to be near placed enough so that this coherence can be maintained. In [47], suggested that this condition may apply within an azimuth range of approximately 10˚. However, using isotropic point target may not always guarantee the condition if angular range exceeds 10˚. Especially, in bistatic configuration, as bistatic angle increases, some standard point target may not hold phase stable characteristic, e.g. dihedrals [41].

In this thesis, on the one hand, this condition was assumed that it was met. On the other hand, the condition was possibly actually met. Because the point-like target was used, to ensure the isotropic characteristic, as well as the total azimuth span of the satellite, was within the

angular range of 1.9˚ relative to the receiver position. The latter might also hold true for this coherence condition in the real target area case, although the target area was not isotropic. The narrow azimuth span of the satellite occurred when the satellite was ascending to change its elevation by 11.86˚ in 25 minutes. This gradual elevation change is difficult to obtain for a long period by commercial airplanes or geostationary satellites. In this case, the GNSS satellites are the candidate who can descend or ascend their orbit steeply to obtain narrow azimuth span.

For the signal coherence, in [41], under the laboratory environment, found that phase difference between apertures (scan-to-scan) varied within approximately ±15˚. This phase difference can maintain signal coherence and enable successful coherence combination. In this thesis, k-space support was used to analyse and choose appropriate signals. Two chosen signals obtained from two apertures that had a gap between them. This gap was caused by discontinuity of the satellite trajectory and also occurred as a gap in spatial frequency or k-space domain.

Despite, total k-space support of the chosen signals (Figure 6.5) had a small gap between the individuals k-space support, it later showed that the gap was sufficiently small to maintain signal coherence. The size of the gap was approximately 0.2 rad/m in both k_x and k_y directions. The gap size can be multiplied by wavelength to convert into phase different term. As a result, the resultant phase difference between the two apertures was approximately 0.051 radian or 2.92˚. This small phase different yielded the sidelobes level less than -7 dB in cross-range and -12 dB in range directions, which was deemed practical. This indicated that there was the possibility of having coherence between the signals. Otherwise, the

sidelobes level would be as high, possibly, as the main lobe and hence degrade the ability to detect the target.

So far, the possibility of having coherence conditions was discussed above. Target scattering coherence might be maintained if transmitters move within narrow azimuth span. For signal coherence, the candidate signals can be chosen using k-space support. Those appropriate signals may have a gap between them in the k-space domain. But it has to be sufficiently small to allow maintaining the coherence. To comply with both conditions and obtain successful coherent combination, the GNSS-based SAR is one of the candidate systems. The GNSS satellites have narrow azimuth change within their natural orbit. Equally, the orbit of the GNSS satellites are publicly known, thus analysing k-space support can be done according to the published information to choose appropriate signals. The satellites broadcast signals all the time. Therefore signals can be acquired all the time whenever the conditions are met.

Obtaining improvement of spatial resolution and power budget, both coherence conditions required proximity locations of the transmitters, i.e. narrow azimuth span. As a result, this technique might not introduce more information to a multistatic image in term of identified target or geometric features (as in non-coherent case) since bistatic images contain similar information about the scene.

Interestingly, the spatial resolution improvement was a factor of two and length of the total k-space support was also approximately twice larger than the individuals. They might have some linkage between them that k-space can be used to serve as a theoretical expectation. In this chapter, this was initially analysed, and the trend of improvement is consistent. Despite, their values were different, but the order of difference is not substantial. In the analysis and

results, the resolution from k-space support was based on [87], which is a method for a monostatic system. Monostatic range and cross-range are in the directions of transmitted signal and platform trajectory, respectively. These are different from bistatic counterparts. Moreover, range and cross-range terms used in this chapter are the distance in the local coordinate from the receiver and the perpendicular line to the range direction, respectively. The further investigation is beyond the scope of this thesis, and this can be individual research on its own as future work to further investigate the association between k-space support and theoretical spatial resolution expectation.

As shown in previous sections, the resolution was improved by forming a longer effective multistatic aperture. This case can be done by using two or more transmitters to increase angular spanning of the observation. However, suitable transmitters are chosen by analysing their k-space extends which has to be selected in the manner that no gap or has a smaller gap as possible. Power budget also other improved factors which caused by the same effect, that is the longer aperture which leads to longer dwell time on target. On the other hand, using two or more different frequencies could improve the range resolution as the total bandwidth is increased.

6.12 Summary

This chapter presents coherent multistatic SAR using GNSS-based SAR. It used both a point-like target and a real target area to demonstrate the technique. Point spread functions of the point-like target and passive bistatic SAR imageries of the real target area were obtained to form their multistatic counterpart. The condition for scattering coherence was assumed it was met while the scope of the paper focused solely on signal coherence.

A basic multistatic configuration was used. It was emulated by two consecutive datasets from the same satellite with a small gap between them, and a single receiver. Two datasets were appropriately chosen by analysing in the k-space domain. They have adjacent k-space support extent with a small gap. This gap was shown that it is sufficiently small to maintain the signal coherence.

Coherent combination with both targets was done by adding the complex value of their corresponding bistatic images in a pixel-by-pixel basis. The multistatic results from both target scenarios are conformed and show approximately twice times finer spatial resolution than the bistatic counterparts.

The results showed that coherent multistatic SAR using GNSS-based SAR is possible and enable substantially improved resolution. This also establishes a framework for coherent multistatic SAR in general. Future work will investigate more realistic multistatic configuration where two or more different satellites fly along different trajectories.

Chapter 7

Conclusions and Future Work

7.1 Conclusions

In this thesis, multistatic SAR was experimentally explored using the GNSS-based SAR system with a single receiver. The experiments used both the non-coherent and coherent combination techniques to form corresponding multistatic images. Results showed that in case of non-coherent multistatic SAR, information could be enhanced in the multistatic image and in case of coherent multistatic SAR, drastically spatial resolution improvement can be obtained.

For non-coherent multistatic SAR, four different satellites from two different GNSS constellation were acquired their signals to obtain forty-six bistatic images from the real target area. These bistatic images were combined using a non-coherent method to form the multistatic image. In the multistatic image, geometric features, which are edge and shapes, were revealed with the finer quality compared to its bistatic counterpart. In this case, edges and shapes that were highlighted by returns on the multistatic image can reflect their actual shape. This was because of a high spatial diversity of the satellite position that used to observe the target area. It can gather different information from different viewing angle and enhance resulting information space.

Moreover, the dimensions of the objects in the multistatic image were further estimated and found that they were comparable to those estimated from Google satellite imagery. Estimating dimensions from those obtained bistatic images was challenging because it requires edges and shapes of the objects. These features were difficult to distinguish in a single bistatic image and depend on viewing angle and bistatic scattering properties. Alternatively, extracting features from individual bistatic images and then combining these features non-coherently, can be used to distinguish target composition. In this thesis, the results supported that a tree and a building can be classified using variations of bistatic reflections.

Through these non-coherent multistatic SAR results, using this combination method, a number of images used to form a multistatic image and spatial diversity of satellite positions are required to be balanced. High spatial diversity with a small set of images will affect the quality of a multistatic image. A large set of bistatic images with a limited diversity of satellite positions will not enhance information from the scene due to redundant information. In term of complexity of non-coherent combination, despite using basic non-coherent method, results showed that image quality and the obtained information could be used as a baseline for more complex non-coherent combination.

For the coherent multistatic SAR, a point-like target and a real target area were used to demonstrate the technique. This experiment used basic multistatic configuration using two different satellites. Two apertures with spatial separation acquired from the same satellite were used to emulate basic geometry. K-space support was used to predict which signals could be coherently combined. In this case, candidate signals were chosen from two adjacent k-space support in the spatial frequency domain, which had a small gap between them.

The results from the PSF level, which obtained from the point-like target, show that drastically improvement can be achieved from the coherent multistatic SAR. Although sidelobe level of the coherent multistatic PSF was higher than the bistatic PSF, it still deemed practical approximately below -7 dB in a cross-range direction and below -12 dB in a range direction. This amount of improvement can also be achieved at the image level from the real target area. These spatial resolution improvements were found that they had approximately twice of the bistatic counterparts. They were coincident with the size of the total k-space support of the multistatic results.

Moreover, the power budget of the coherent multistatic results was found that it was improved from the bistatic counterparts by approximately 6 dB. This figure also coincident with the double improvement from the bistatic power budget as same as the spatial resolution case. The relationship between k-space support and spatial resolution was preliminary analysed. In this case, the spatial resolution was determined from k-space. The results found that the resolution of the multistatic was finer than the bistatic by an approximate factor of two.

In the coherent multistatic SAR, the position of transmitters is essential as it constitutes coherence. The results show that despite there was a gap between the two k-space supports, spatial resolution improvement was still achieved with deem sidelobe level. It could be explained by the total azimuth span of the satellite was less than 2˚ in 25 minutes. This rate of change can be obtained from the GNSS satellites which flying in narrow azimuth span while ascending or descending their elevation.

7.2 Future Work

Suggestions for future work are the following.

- Combination method

This thesis used the basic combination methods both non-coherent and coherent multistatic techniques to explore the capability of GNSS-based multistatic SAR. However, using a more advanced combination method could obtain more information about a target area. Also, processing bistatic and multistatic images prior combination could also enhance information. Several relevant works can be found in [37, 39] where the former extended the basic non-coherent combination with the region of feature whilst the latter use CLEAN algorithm to extract scattering centre from a bistatic and/or multistatic images before non-coherent combination.

- Spatial resolution analysis using k-space

In chapter 6, as aforementioned, it was found that total k-space (multistatic PSF) whose size was approximately twice of the k-space support of the individual bistatic PSF. The resolution improvement in the coherent multistatic SAR case was also twice of the individual cases. This coincident could link relationship between k-space support and spatial resolution. The preliminary analysis in this thesis found that the resolution determined from k-space has the same trend as the case determined from PSF. Also, the resolution determined from the total k-space support (multistatic) was finer by a factor of two over the bistatic k-space support. The considered limitation of this analysis is that the PSF and image were defined on the local coordinate whose origin is at the receiver position. Spatial resolution was defined on the direction of the line of sight of the receiver and direction that perpendicular to the line of

sight. For k-space support, the origin is a target location. Understanding the geometry of k-space to develop coordinate transformation is required so that both k-space support and PSF are on the same coordinate.

- Applications of GNSS-based multistatic SAR imagery

The results of non-coherent multistatic SAR showed that information could be enhanced. The application that used the information or featured extracted from the non-coherent multistatic SAR image could complement the usefulness of the multistatic image. Suggested applications could be target composition or terrain classification as well as target recognition.

- Spatial resolution improvement by expanding K-space

K-space support can be further expanded in both directions using more platforms or more different frequencies. This could benefit further spatial resolution improvement and other performance, e.g. power. In order to achieve this relative transmitter orientation should be studied to enable contiguous k-space support and coherent target scattering. Moreover, gap-filling techniques are also equally important to study for the case that k-space continuity cannot be guaranteed.

- Translating computer vision methods for radar imagery analysis.

This work study on how to apply computer vision to analyse radar imagery. Apply typical computer vision techniques to radar imagery; some information may not be revealed, e.g. the actual shape of the target. Instead of detecting object edge, those computer vision techniques reveal blobs which is individual returns from dominant scatters. Moreover,

Binarisation of the initial intensity map degrades much information which can potentially allow to associate blobs into contiguous regions and then can reveal the shape of targets.

Appendix A Experimental Bistatic PSF

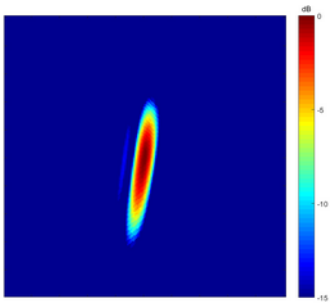

PSF 1

GPS BIIF-05-30 L5 at 09:45

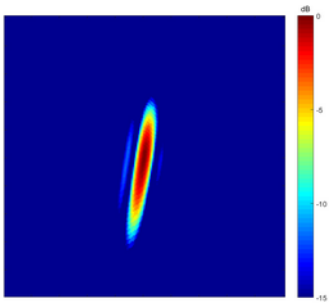

PSF 2

GPS BIIF-05-30 L5 at 10:00

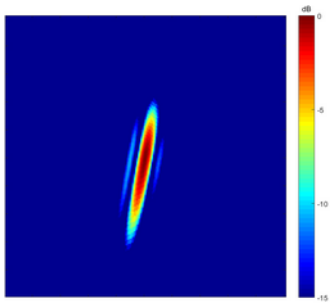

PSF 3

GPS BIIF-05-30 L5 at 10:15

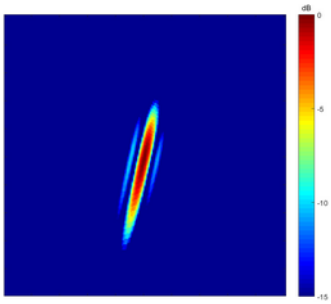

PSF 4

GPS BIIF-05-30 L5 at 10:30

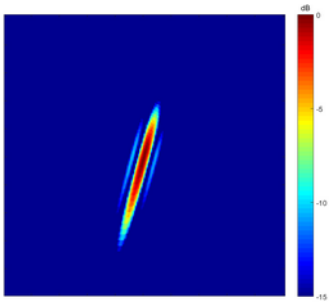

PSF 5

GPS BIIF-05-30 L5 at 10:45

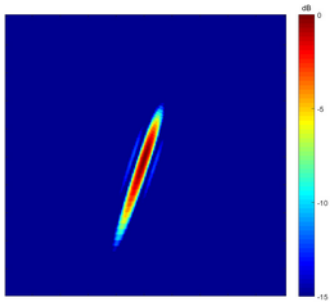

PSF 6

GPS BIIF-05-30 L5 at 11:00

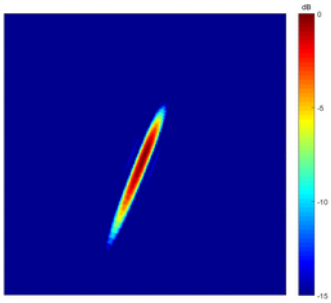

PSF 7

GPS BIIF-05-30 L5 at 11:15

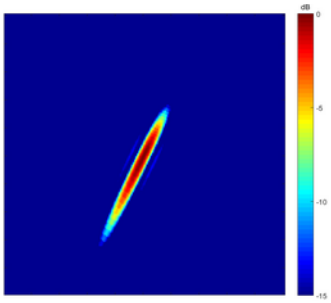

PSF 8

GPS BIIF-05-30 L5 at 11:30

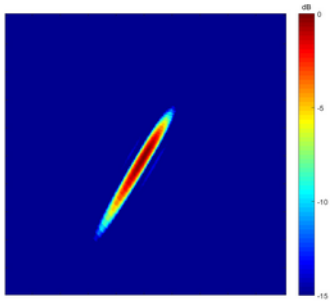

PSF 9

GPS BIIF-05-30 L5 at 11:45

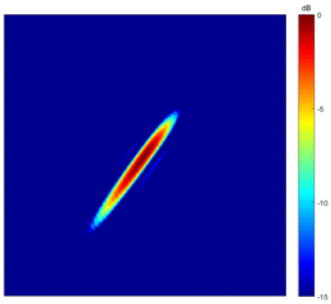

PSF 10

GPS BIIF-05-30 L5 at 12:00

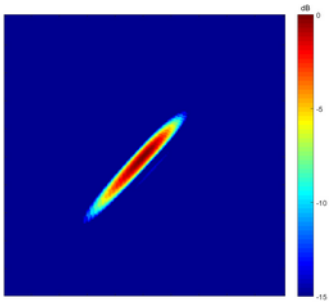

PSF 11

GPS BIIF-05-30 L5 at 12:15

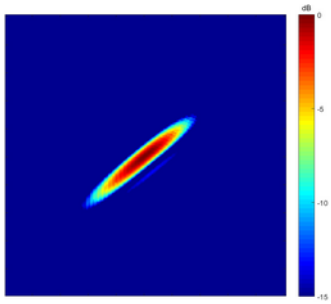

PSF 12

GPS BIIF-05-30 L5 at 12:30

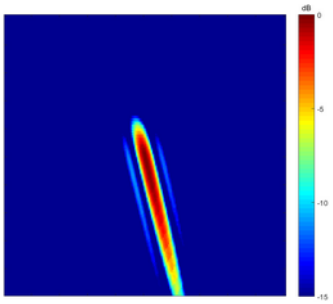

PSF 13

Galileo GSAT-0205-24 E5a at 09:45

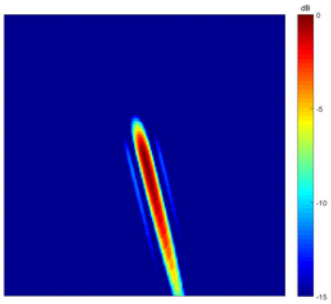

PSF 14

Galileo GSAT-0205-24 E5a at 10:00

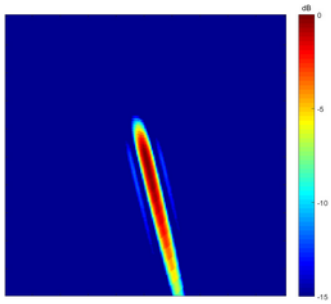

PSF 15

Galileo GSAT-0205-24 E5a at 10”15

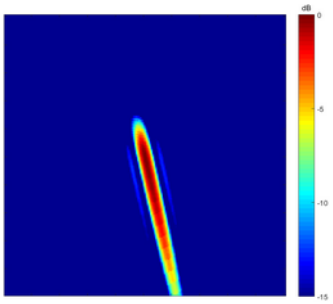

PSF 16

Galileo GSAT-0205-24 E5a at 10:30

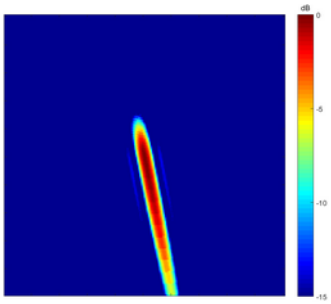

PSF 17

Galileo GSAT-0205-24 E5a at 10:45

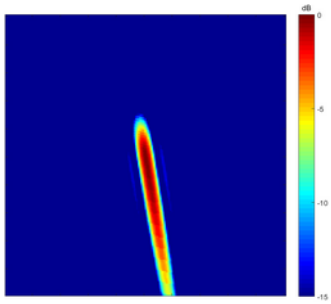

PSF 18

Galileo GSAT-0205-24 E5a at 11:00

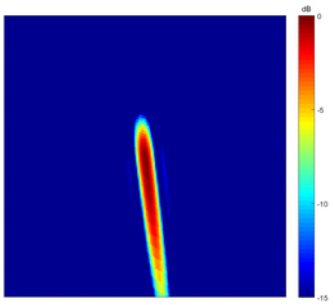

PSF 19

Galileo GSAT-0205-24 E5a at 11:15

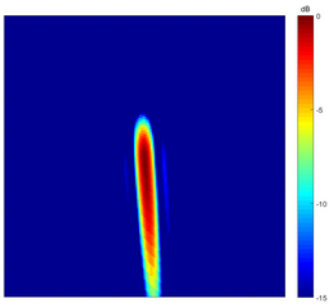

PSF 20

Galileo GSAT-0205-24 E5a at 11:30

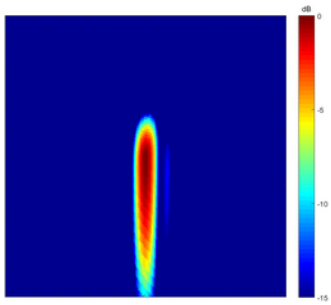

PSF 21

Galileo GSAT-0205-24 E5a at 11:45

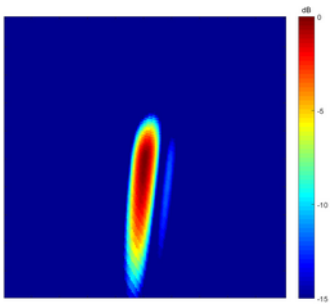

PSF 22

Galileo GSAT-0205-24 E5a at 12:00

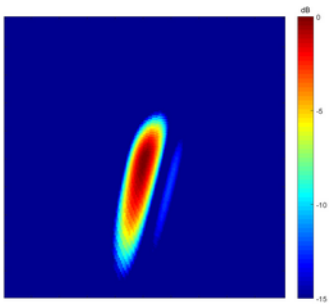

PSF 23

Galileo GSAT-0205-24 E5a at 12:15

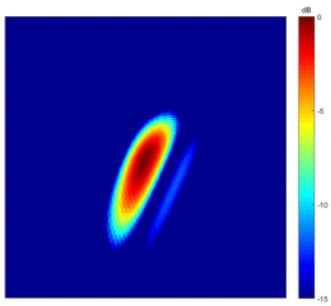

PSF 24

Galileo GSAT-0205-24 E5a at 12:30

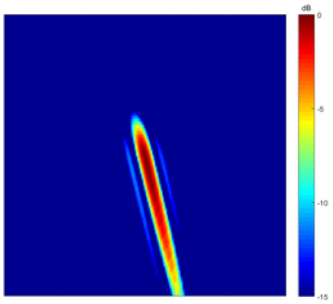

PSF 25

Galileo GSAT-0205-24 E5b at 09:45

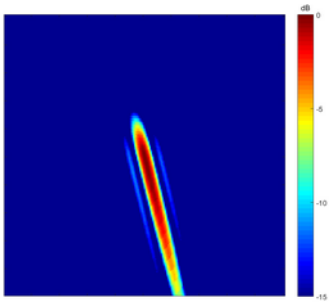

PSF 26

Galileo GSAT-0205-24 E5b at 10:00

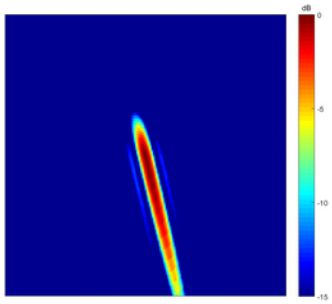

PSF 27

Galileo GSAT-0205-24 E5b at 10:15

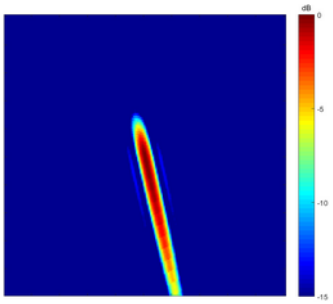

PSF 28

Galileo GSAT-0205-24 E5b at 10:30

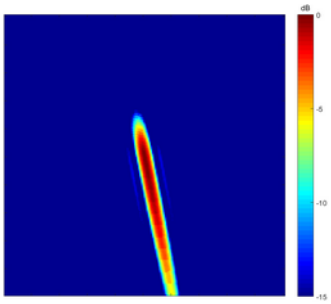

PSF 28

Galileo GSAT-0205-24 E5b at 10:45

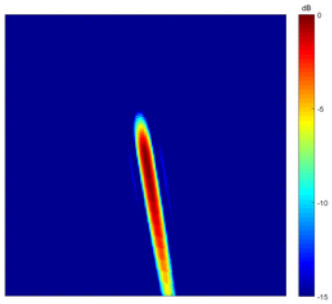

PSF 30

Galileo GSAT-0205-24 E5b at 11:00

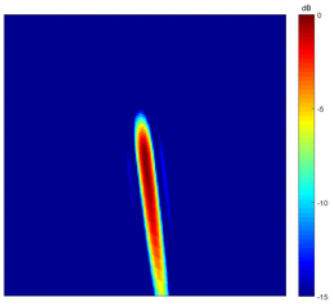

PSF 31

Galileo GSAT-0205-24 E5b at 11:15

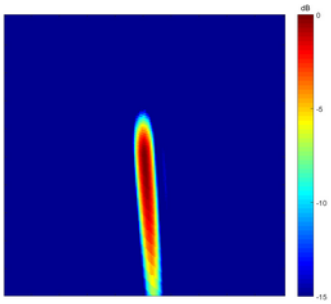

PSF 32

Galileo GSAT-0205-24 E5b at 11:30

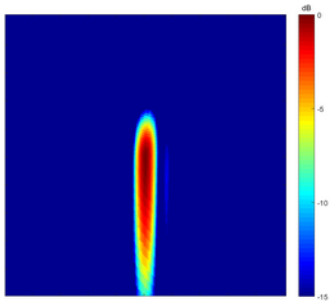

PSF 33

Galileo GSAT-0205-24 E5b at 11:45

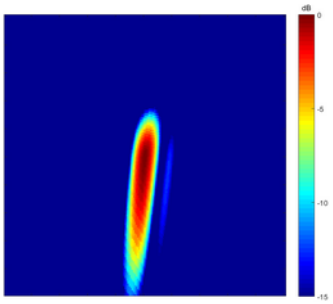

PSF 34

Galileo GSAT-0205-24 E5b at 12:00

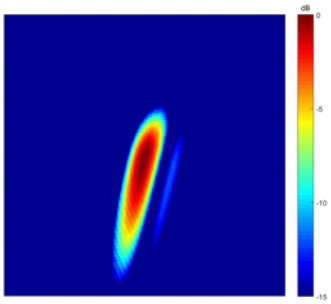

PSF 35

Galileo GSAT-0205-24 E5b at 12:15

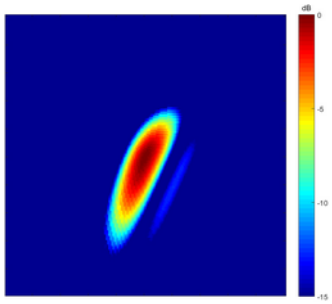

PSF 36

Galileo GSAT-0205-24 E5b at 12:30

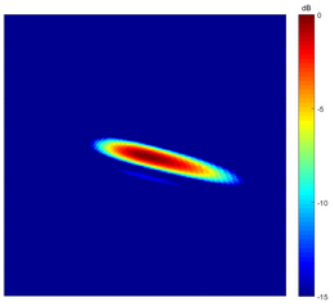

PSF 37

GSAT-0214-05 E5a at 14:57

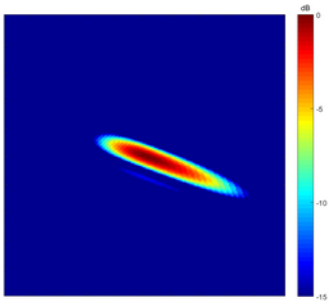

PSF 38

GSAT-0214-05 E5a at 15:07

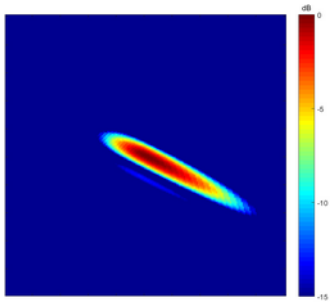

PSF 39

GSAT-0214-05 E5a at 15:16

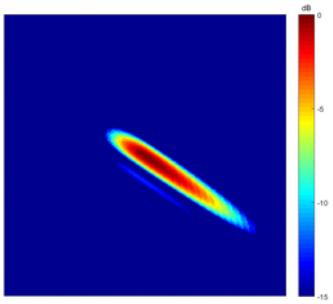

PSF 40

GSAT-0214-05 E5a at 15:26

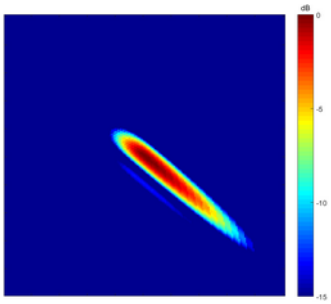

PSF 41

GSAT-0214-05 E5a at 15:37

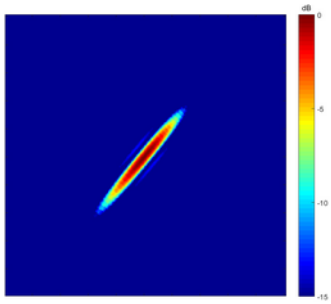

PSF 42

GPS BIIF-07-09 L5 at 14:25

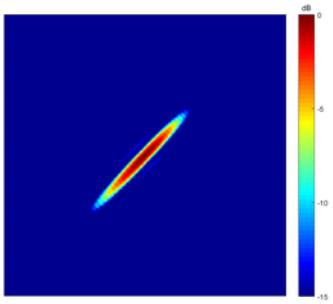

PSF 43

GPS BIIF-07-09 L5 at 14:35

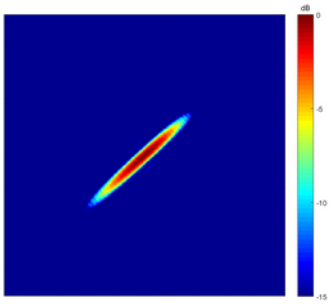

PSF 44

GPS BIIF-07-09 L5 at 14:44

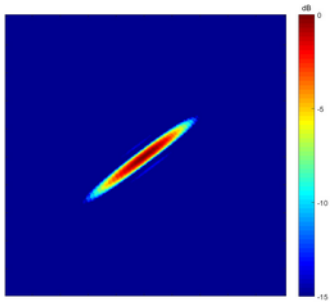

PSF 45

GPS BIIF-07-09 L5 at 14:57

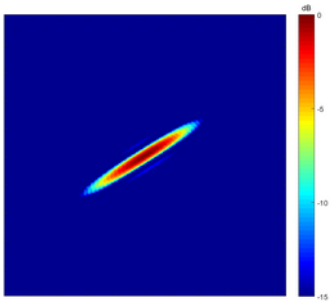

PSF 46

GPS BIIF-07-09 L5 at 15:07

Appendix B Experimental Bistatic Imagery

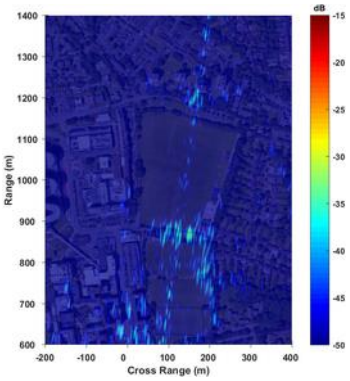

Image 1

GPS BIIF-05-30 L5 at 09:45

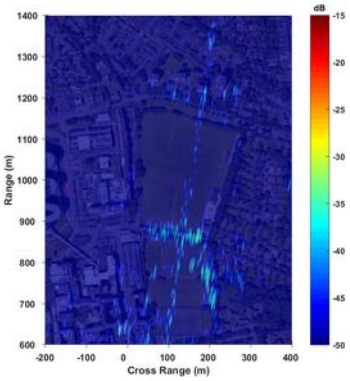

Image 2

GPS BIIF-05-30 L5 at 10:00

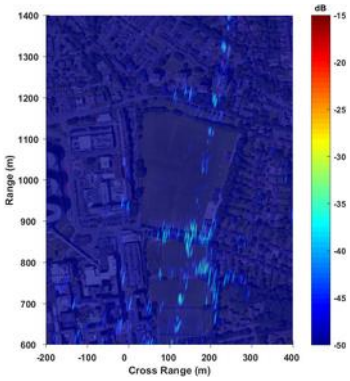

Image 3

GPS BIIF-05-30 L5 at 10:15

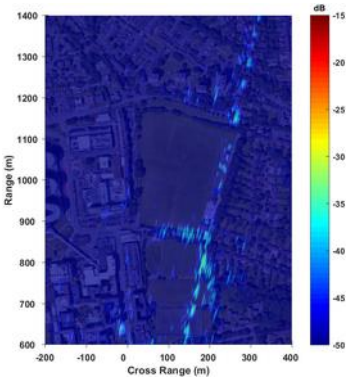

Image 4

GPS BIIF-05-30 L5 at 10:30

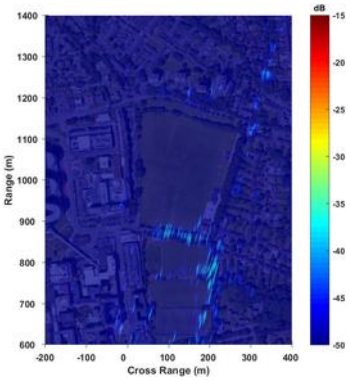

Image 5

GPS BIIF-05-30 L5 at 10:45

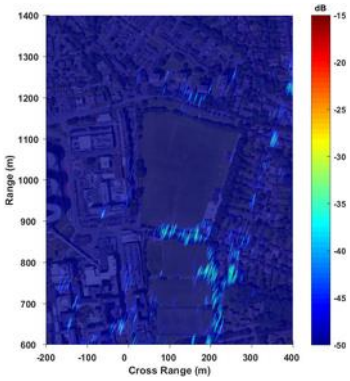

Image 6

GPS BIIF-05-30 L5 at 11:00

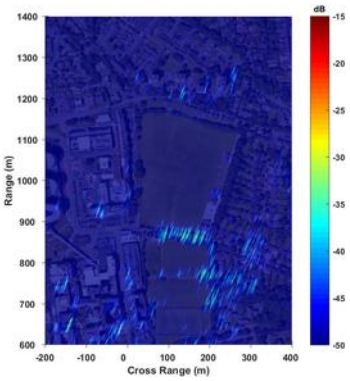

Image 7

GPS BIIF-05-30 L5 at 11:15

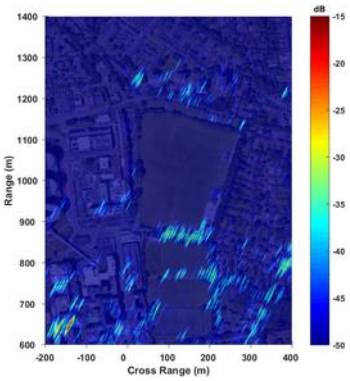

Image 8

GPS BIIF-05-30 L5 at 11:30

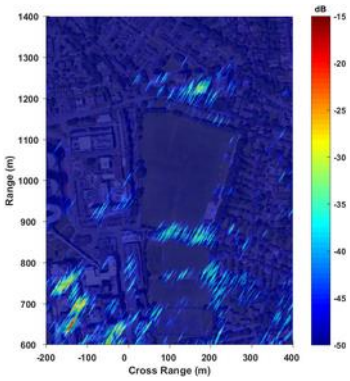

Image 9

GPS BIIF-05-30 L5 at 11:45

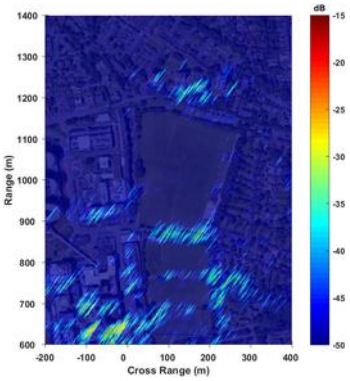

Image 10

GPS BIIF-05-30 L5 at 12:00

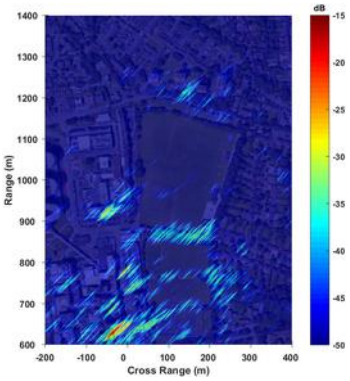

Image 11

GPS BIIF-05-30 L5 at 12:15

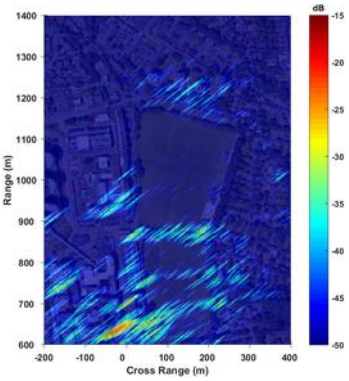

Image 12

GPS BIIF-05-30 L5 at 12:30

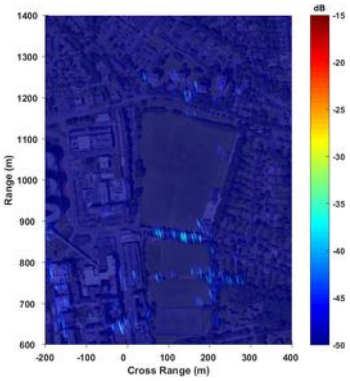

Image 13

Galileo GSAT-0205-24 E5a at 09:45

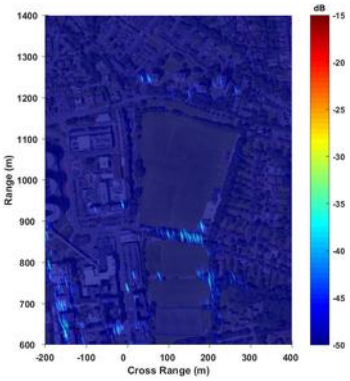

Image 14

Galileo GSAT-0205-24 E5a at 10:00

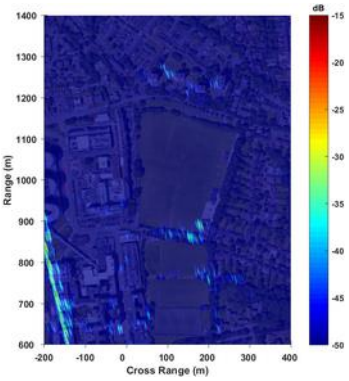

Image 15

Galileo GSAT-0205-24 E5a at 10”15

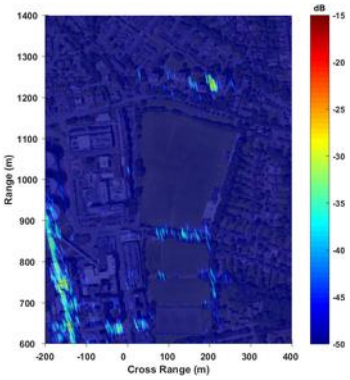

Image 16

Galileo GSAT-0205-24 E5a at 10:30

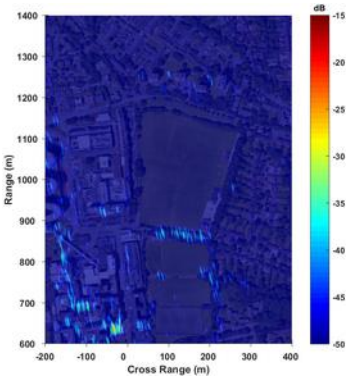

Image 17

Galileo GSAT-0205-24 E5a at 10:45

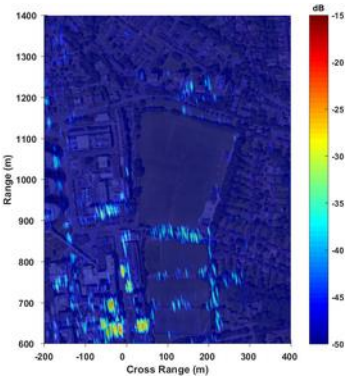

Image 18

Galileo GSAT-0205-24 E5a at 11:00

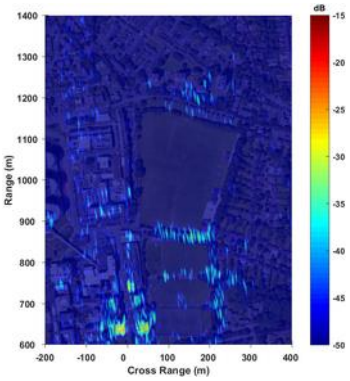

Image 19

Galileo GSAT-0205-24 E5a at 11:15

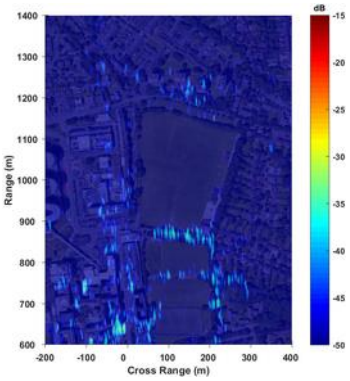

Image 20

Galileo GSAT-0205-24 E5a at 11:30

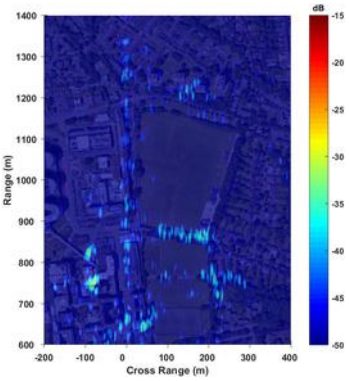

Image 21

Galileo GSAT-0205-24 E5a at 11:45

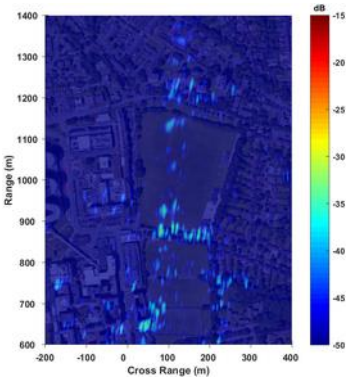

Image 22

Galileo GSAT-0205-24 E5a at 12:00

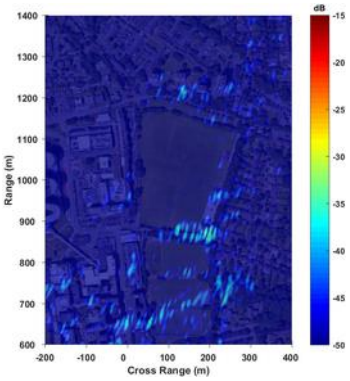

Image 23

Galileo GSAT-0205-24 E5a at 12:15

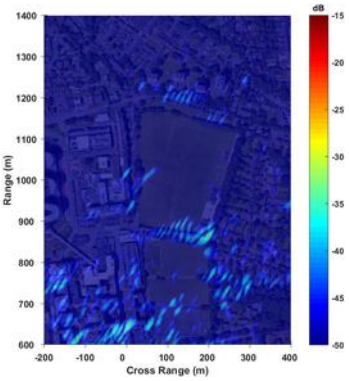

Image 24

Galileo GSAT-0205-24 E5a at 12:30

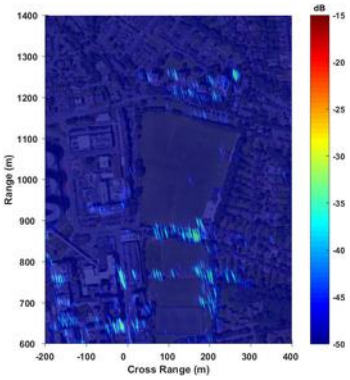

Image 25

Galileo GSAT-0205-24 E5b at 09:45

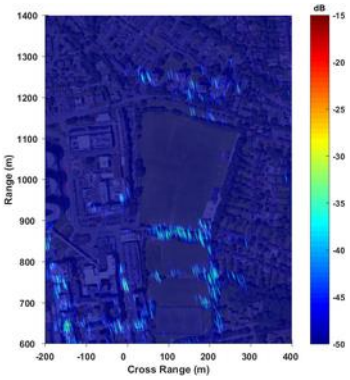

Image 26

Galileo GSAT-0205-24 E5b at 10:00

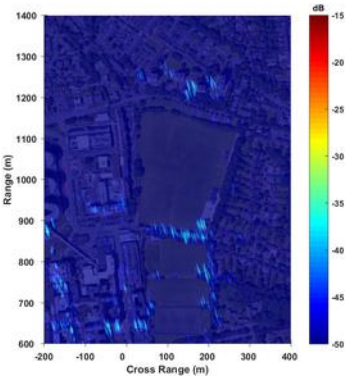

Image 27

Galileo GSAT-0205-24 E5b at 10:15

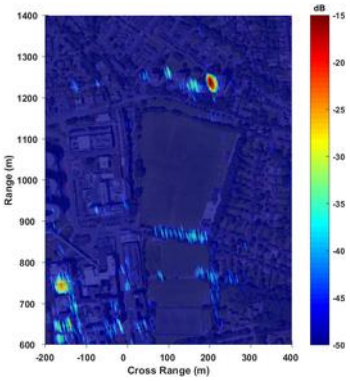

Image 28

Galileo GSAT-0205-24 E5b at 10:30

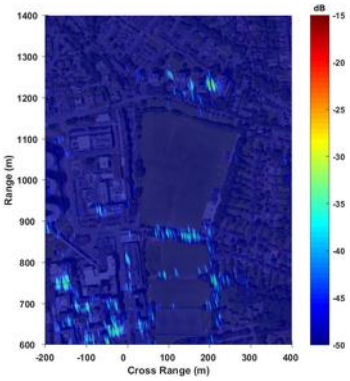

Image 29

Galileo GSAT-0205-24 E5b at 10:45

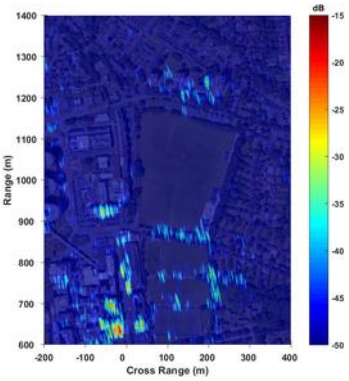

Image 30

Galileo GSAT-0205-24 E5b at 11:00

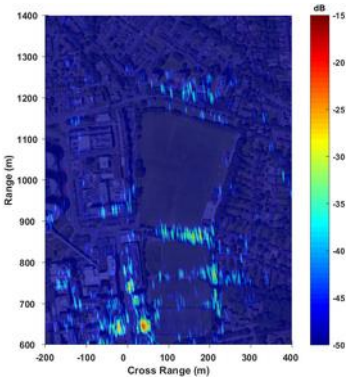

Image 31

Galileo GSAT-0205-24 E5b at 11:15

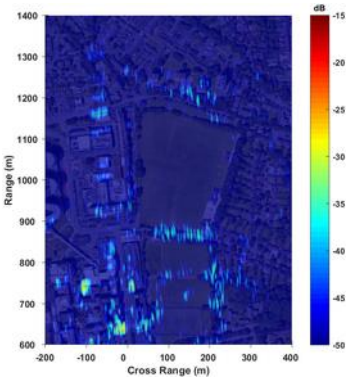

Image 32

Galileo GSAT-0205-24 E5b at 11:30

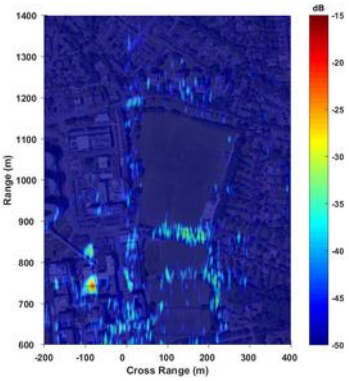

Image 33

Galileo GSAT-0205-24 E5b at 11:45

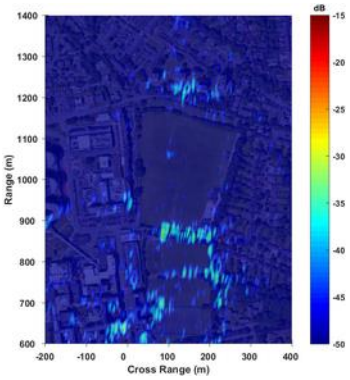

Image 34

Galileo GSAT-0205-24 E5b at 12:00

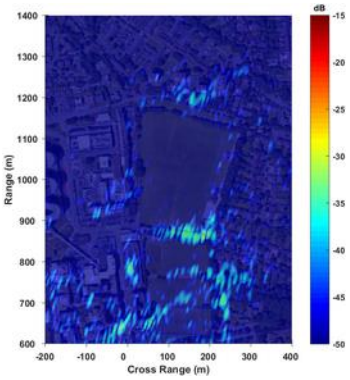

Image 35

Galileo GSAT-0205-24 E5b at 12:15

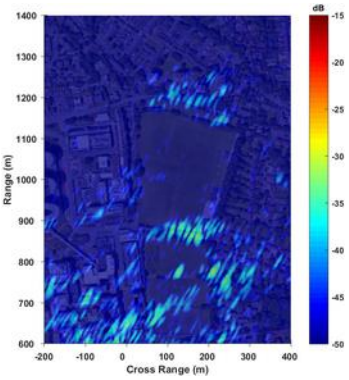

Image 36

Galileo GSAT-0205-24 E5b at 12:30

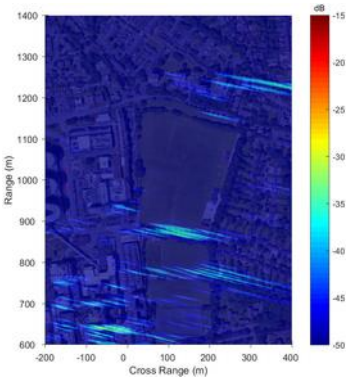

Image 37

GSAT-0214-05 E5a at 14:57

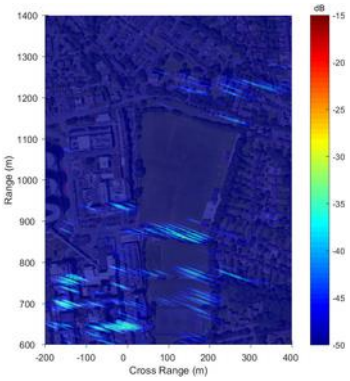

Image 38

GSAT-0214-05 E5a at 15:07

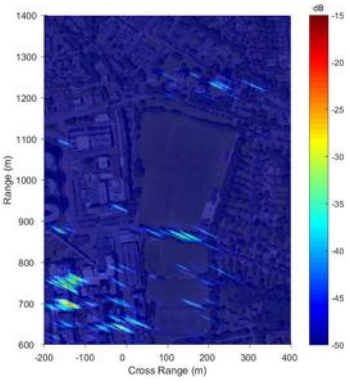

Image 39

GSAT-0214-05 E5a at 15:16

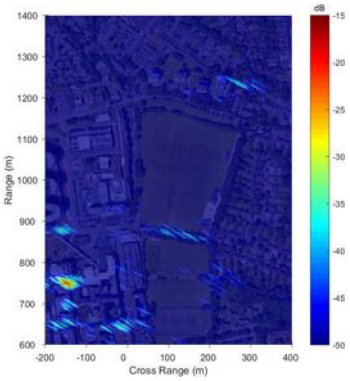

Image 40

GSAT-0214-05 E5a at 15:26

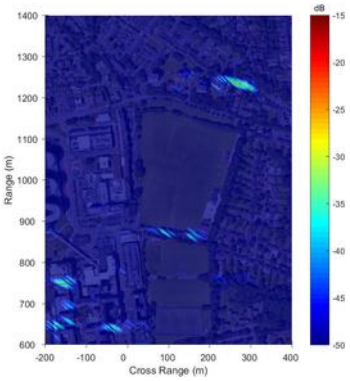

Image 41

GSAT-0214-05 E5a at 15:37

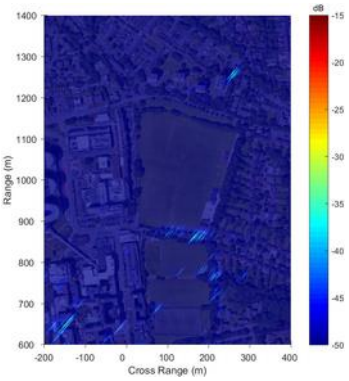

Image 42

GPS BIIF-07-09 L5 at 14:25

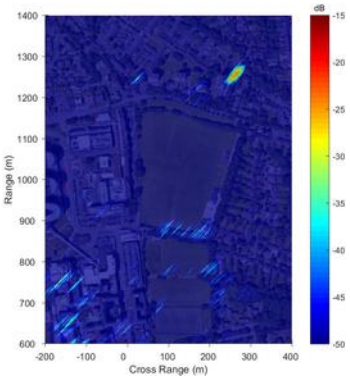

Image 43

GPS BIIF-07-09 L5 at 14:35

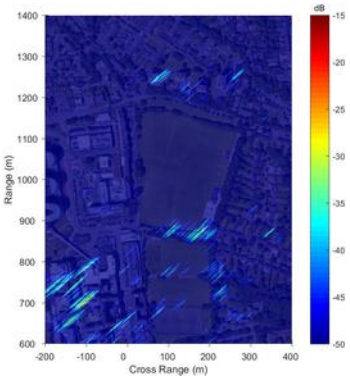

Image 44

GPS BIIF-07-09 L5 at 14:44

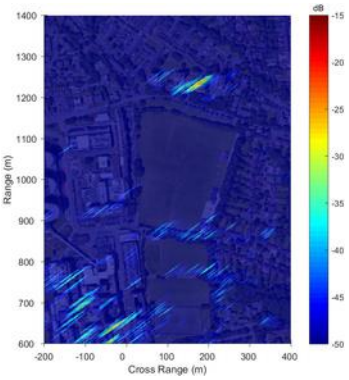

Image 45

GPS BIIF-07-09 L5 at 14:57

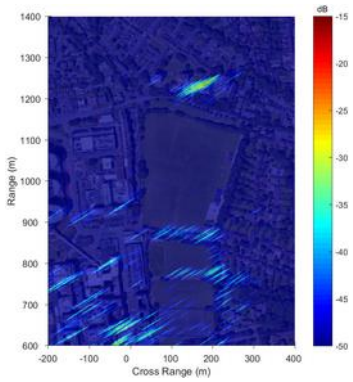

Image 46

GPS BIIF-07-09 L5 at 15:07

List of References

[1] A. Moreira *et al.*, "A tutorial on synthetic aperture radar," *IEEE Geoscience and Remote Sensing Magazine*, vol. 1, no. 1, pp. 6-43, 2013.

[2] G. H. BORN *et al.*, "Seasat Mission Overview," *Science*, vol. 204, no. 4400, pp. 1405-1406, 1979.

[3] R. L. Jordan, "The Seasat-A synthetic aperture radar system," *IEEE Journal of Oceanic Engineering*, vol. 5, no. 2, pp. 154-164, 1980.

[4] E. P. W. Attema, "The Active Microwave Instrument on-board the ERS-1 satellite," *Proceedings of the IEEE*, vol. 79, no. 6, pp. 791-799, 1991.

[5] L. C. Morena *et al.*, "An introduction to the RADARSAT-2 mission," *Canadian Journal of Remote Sensing*, vol. 30, no. 3, pp. 221-234, 2004/01/01 2004.

[6] M. Cohen *et al.*, "NovaSAR-S low cost spaceborne SAR payload design, development and deployment of a new benchmark in spaceborne radar," in *2017 IEEE Radar Conference (RadarConf)*, 2017, pp. 0903-0907.

[7] M. Rodriguez-Cassola *et al.*, "First Bistatic Spaceborne SAR Experiments With TanDEM-X," *IEEE Geoscience and Remote Sensing Letters*, vol. 9, no. 1, pp. 33-37, 2012.

[8] G. Krieger *et al.*, "MirrorSAR: A fractionated space radar for bistatic, multistatic and high-resolution wide-swath SAR imaging," in *2017 IEEE International Geoscience and Remote Sensing Symposium (IGARSS)*, 2017, pp. 149-152.

[9] Craig Underwood *et al.*, "PASSAT: passive imaging radar constellation for near-persistent earth observation," presented at the International Astronautical Congress (IAC), Astralia, 2017.

[10] M. Antoniou *et al.*, "Passive SAR satellite constellation for near-persistent earth observation: Prospects and issues," *IEEE Aerospace and Electronic Systems Magazine*, vol. 33, no. 12, pp. 4-15, 2018.

[11] M. Antoniou *et al.*, "Results of a space-surface bistatic SAR image formation algorithm," *IEEE Transactions on Geoscience and Remote Sensing*, vol. 45, no. 11, pp. 3359-3371, 2007.

[12] M. Antoniou *et al.*, "Space-surface bistatic SAR image formation algorithms," *IEEE Transactions on Geoscience and Remote Sensing*, vol. 47, no. 6, pp. 1827-1843, 2009.

[13] M. Antoniou and M. Cherniakov, "GNSS-based bistatic SAR: a signal processing view," *EURASIP Journal on Advances in Signal Processing*, vol. 2013, no. 1, p. 98, 2013.

[14] M. Cherniakov *et al.*, "Space-surface bistatic synthetic aperture radar with global navigation satellite system transmitter of opportunity-experimental results," *IET Radar, Sonar & Navigation*, vol. 1, no. 6, pp. 447-458, 2007.

[15] M. Cherniakov and T. Zeng, *Space-Surface Bistatic SAR* (Bistatic Radar). 2008.

[16] M. Antoniou *et al.*, "Experimental Demonstration of Passive BSAR Imaging Using Navigation Satellites and a Fixed Receiver," *IEEE Geoscience and Remote Sensing Letters*, vol. 9, no. 3, pp. 477-481, 2012.

[17] F. Liu *et al.*, "Point spread function analysis for BSAR with GNSS transmitters and long dwell times: theory and experimental confirmation," *IEEE Geoscience and Remote Sensing Letters,* vol. 10, no. 4, pp. 781-785, 2013.

[18] M. Antoniou *et al.*, "Passive bistatic synthetic aperture radar imaging with Galileo transmitters and a moving receiver: experimental demonstration," *IET Radar, Sonar & Navigation,* vol. 7, no. 9, pp. 985-993, 2013.

[19] M. Antoniou and M. Cherniakov, "GNSS-based passive radar," in *Novel Radar Techniques and Applications Volume 1: Real Aperture Array Radar, Imaging Radar, and Passive and Multistatic Radar*(Radar, Sonar & Navigation: Institution of Engineering and Technology, 2017, pp. 719-766.

[20] M. Cherniakov *et al.*, "Passive Space-Surface Bistatic SAR for local area monitoring: Primary feasibility study," in *2009 European Radar Conference (EuRAD)*, 2009, pp. 89-92.

[21] F. Liu *et al.*, "Coherent Change Detection Using Passive GNSS-Based BSAR: Experimental Proof of Concept," *IEEE Transactions on Geoscience and Remote Sensing,* vol. 51, no. 8, pp. 4544-4555, 2013.

[22] H. Ma *et al.*, "Passive GNSS-Based SAR Resolution Improvement Using Joint Galileo E5 Signals," *IEEE Geoscience and Remote Sensing Letters,* vol. 12, no. 8, pp. 1640-1644, 2015.

[23] H. Ma *et al.*, "Galileo-based Bistatic SAR Imaging Using Joint E5 signals: experimental proof-of-concept," in *International Conference on Radar Systems*, Belfast, UK, 2017, pp. 1-5.

[24] U. Nithirochananont *et al.*, "Passive GNSS-based multistatic SAR: first experimental results," in *2018 19th International Radar Symposium (IRS)*, 2018, pp. 1-9.

[25] U. Nithirochananont *et al.*, "Passive multi-static SAR – experimental results," *IET Radar, Sonar & Navigation,* vol. 13, no. 2, pp. 222-228, 2019.

[26] U. Nithirochananont *et al.*, "Passive coherent multistatic SAR: experimental results with a point-like target," in *2019 20th International Radar Symposium (IRS)*, 2019, pp. 1-6.

[27] U. Nithirochananont *et al.*, "Passive coherent multistatic SAR using spaceborne illuminators," *IET Radar, Sonar & Navigation,* vol. 14, no. 4, pp. 628-636, 2020.

[28] Y. Wu and D. C. Munson, *Multistatic synthetic aperture imaging of aircraft using reflected television signals* (Aerospace/Defense Sensing, Simulation, and Controls). SPIE, 2001.

[29] V. Krishnan *et al.*, "Multistatic Synthetic Aperture Radar Image Formation," *IEEE Transactions on Image Processing,* vol. 19, no. 5, pp. 1290-1306, 2010.

[30] I. Stojanovic *et al.*, "Compressed Sensing of Monostatic and Multistatic SAR," *IEEE Geoscience and Remote Sensing Letters,* vol. 10, no. 6, pp. 1444-1448, 2013.

[31] X. Mao *et al.*, "Low-complexity sparse reconstruction for high-resolution multi-static passive SAR imaging," *EURASIP Journal on Advances in Signal Processing,* vol. 2014, no. 1, p. 104, 2014.

[32] Q. Wu *et al.*, "High-Resolution Passive SAR Imaging Exploiting Structured Bayesian Compressive Sensing," *IEEE Journal of Selected Topics in Signal Processing,* vol. 9, no. 8, pp. 1484-1497, 2015.

[33] T. Kraus *et al.*, "Multistatic SAR imaging: Comparison of simulation results and experimental data," in *International Conference on Radar Systems (Radar 2017)*, 2017, pp. 1-5.

[34] T. Zeng *et al.*, "Generalized approach to resolution analysis in BSAR," *IEEE Transactions on Aerospace and Electronic Systems*, vol. 41, no. 2, pp. 461-474, 2005.
[35] F. Daout *et al.*, "Multistatic and Multiple Frequency Imaging Resolution Analysis-Application to GPS-Based Multistatic Radar," *IEEE Transactions on Aerospace and Electronic Systems*, vol. 48, no. 4, pp. 3042-3057, 2012.
[36] F. Santi *et al.*, "Point Spread Function Analysis for GNSS-Based Multistatic SAR," *IEEE Geoscience and Remote Sensing Letters*, vol. 12, no. 2, pp. 304-308, 2015.
[37] F. Santi *et al.*, "Spatial resolution improvement in GNSS-based SAR using multistatic acquisitions and feature extraction," *IEEE Transactions on Geoscience and Remote Sensing*, vol. 54, no. 10, pp. 6217-6231, 2016.
[38] K. Kulpa, "The CLEAN type algorithms for radar signal processing," in *2008 Microwaves, Radar and Remote Sensing Symposium*, 2008, pp. 152-157.
[39] T. Zeng *et al.*, "Multiangle BSAR imaging based on BeiDou-2 navigation satellite system: experiments and preliminary results," *IEEE Transactions on Geoscience and Remote Sensing*, vol. 53, no. 10, pp. 5760-5773, 2015.
[40] Z. Zeng *et al.*, "Multi-perspective GNSS-based passive BSAR: Preliminary experimental results," in *2013 14th International Radar Symposium (IRS)*, 2013, vol. 1, pp. 467-472.
[41] A. M. Chan *et al.*, "Coherent calibration techniques for multistatic SAR image formation," in *2008 European Radar Conference*, 2008, pp. 324-327.
[42] P. K. Rennich *et al.*, "Coherent multistatic SAR collections and target phenomenology," in *2008 European Radar Conference*, 2008, pp. 152-155.
[43] M. B. Rapson, "Passive multistatic radar imaging using an OFDM based signal of opportunity," Master, Graduate School of Engineering and Management, Air Force Institute of Technology, 2012.
[44] C. Yang *et al.*, "A high resolution multiple-receiver SS-BSAR system," in *2009 IET International Radar Conference*, 2009, pp. 1-5.
[45] G. Ginolhac *et al.*, "Multifrequency and multistatic inverse synthetic aperture radar, with application to FM passive radar," *EURASIP Journal on Advances in Signal Processing*, vol. 2010, no. 1, p. 497074, 2009/12/09 2009.
[46] P. v. Dorp *et al.*, "Coherent Multistatic ISAR imaging," in *IET International Conference on Radar Systems (Radar 2012)*, 2012, pp. 1-6.
[47] J. L. Garry *et al.*, "Investigations toward multistatic passive radar imaging," in *2014 IEEE Radar Conference*, 2014, pp. 0607-0612.
[48] P. Samczynski *et al.*, "SAR/ISAR imaging in passive radars," in *2016 IEEE Radar Conference (RadarConf)*, 2016, pp. 1-6.
[49] S. Tebaldini and F. Rocca, "Multistatic wavenumber tessellation: Ideas for high resolution P-band SAR missions," in *2017 IEEE International Geoscience and Remote Sensing Symposium (IGARSS)*, 2017, pp. 2412-2415.
[50] M. I. Skolnik, "Radar handbook," 3rd ed. ed. London: McGraw-Hill, 2008.
[51] D. Tzagkas, "Coherent change detection with GNSS-based SAR -Experimental study," University of Birmingham, Birmingham, 2018.
[52] M. Ritchie, "Statistical analysis of coherent monostatic and bistatic radar sea clutte," PhD, University College London, 2013.
[53] B. R. Mahafza, *Radar systems analysis and design using MATLAB*. Chapman and Hall/CRC, 2005.

[54] W. L. Melvin and James Scheer, Eds. *Principles of modern radar: advanced techniques*. Institution of Engineering and Technology, 2012.
[55] M. Antoniou, "Image formation algorithms for space-surface bistatic SAR," University of Birmingham, Birmingham, 2007.
[56] J. Kovaly *et al.*, "Preliminary Report on the Observation of Snorkels and Sea Clutter Using Coherent Airborne Radar," 1952.
[57] I. G. Cumming and F. H. J. A. H. Wong, Boston, Massachusetts, "Digital Processing of Synthetic Aperture Radar Data: Algorithms and Implementation," 2005.
[58] Q. Lin, "Spaceborne multibaseline SAR tomography for retrieving forest heights," PhD, Department of Electrical Engineering, Stanford University, 2017.
[59] Airbus. (2019, Mar. 20). *TerraSAR-X Image Product Guide: Basic and Enhanced Radar Satellite Imagery* [Online]. Available: https://spacedata.copernicus.eu/documents/12833/14537/TerraSAR-X_ProductGuide
[60] D. C. Munson *et al.*, "A tomographic formulation of spotlight-mode synthetic aperture radar," *Proceedings of the IEEE*, vol. 71, no. 8, pp. 917-925, 1983.
[61] C. V. Jakowatz *et al.*, *Spotlight-Mode Synthetic Aperture Radar: A Signal Processing Approach: A Signal Processing Approach*. Springer Science & Business Media, 2012.
[62] M. Rodriguez-Cassola *et al.*, "Bistatic spaceborne-airborne experiment TerraSAR-X/F-SAR: data processing and results," in *IGARSS 2008 - 2008 IEEE International Geoscience and Remote Sensing Symposium*, 2008, vol. 3, pp. III - 451-III - 454.
[63] M. Cherniakov and K. Kubik, "Secondary applications of wireless technology," in *2000 European Conference on Wireless Technology (ECWT)*, Paris, France, 2000, pp. 305-309.
[64] M. Cherniakov *et al.*, "Bistatic synthetic aperture radar with non-cooperative LEOS based transmitter," in *IEEE 2000 International Geoscience and Remote Sensing Symposium (IGARSS 2000)*, 2000, vol. 2, pp. 861-862 vol.2.
[65] M. Cherniakov, "Space-surface bistatic synthetic aperture radar - prospective and problems," in *RADAR 2002*, 2002, pp. 22-25.
[66] United States Government, "Global positioning system standard positioning service performance standard," 2020.
[67] Information and Analysis Center for Positioning, Navigation and Timing, "Open service performance standard (OS PS)," 2020.
[68] European Union, "Signal-in-space interface control document," 2016.
[69] China Satellite Navigation Office, "Development of the BeiDou Navigation Satellite System " 2009.
[70] M. Antoniou *et al.*, "Space-surface bistatic synthetic aperture radar with navigation satellite transmissions: a review," *Science China Information Sciences*, vol. 58, no. 6, pp. 1-20, 2015.
[71] V. C. Chen and M. Martorella, *Inverse synthetic aperture radar imaging: principles, algorithms and applications*. Institution of Engineering and Technology, 2014.
[72] X. He *et al.*, "Signal detectability in SS-BSAR with GNSS non-cooperative transmitter," *IEE Proceedings - Radar, Sonar and Navigation*, vol. 152, no. 3, pp. 124-132, 2005.
[73] J. B.-y. Tsui, "Fundamentals of global positioning system receivers : a software approach," 2nd ed. ed. Hoboken, N.J.: Hoboken, N.J. : Wiley-Interscience, 2005.

[74] Topcon. (2019, Mar. 20). *Topcon CR-G5* [Online]. Available: https://www.topconpositioning.com/sites/default/files/product_files/cr-g5_broch_7010_2087_revc_sm.pdf
[75] Cobham. (2019, Mar. 20). *Helical antenna model: AMHP13-13L/909* [Online]. Available: https://www.european-antennas.co.uk/media/2146/ds0909.pdf
[76] Ifen. (2019, Mar. 20). *SX3 GNSS software receiver* [Online]. Available: https://www.ifen.com/fileadmin/documents/pdf/SX3/Brosch%C3%BCre_SX3_Sep-2018_DinA4_digital.pdf
[77] Q. Zhang *et al.*, "Spatial decorrelation in GNSS-based SAR coherent change detection," *IEEE Transactions on Geoscience and Remote Sensing,* vol. 53, no. 1, pp. 219-228, 2015.
[78] E. Analytics. (2019, Jul. 01). *Building Heights in England* [Online]. Available: buildingheights.emu-analytics.net
[79] R. Zuo, "Bistatic synthetic aperture radar using GNSS as transmitters of opportunity," PhD, University of Birmingham, 2011.
[80] F. Santi *et al.*, "CLEAN technique for passive bistatic and multistatic SAR with GNSS transmitters," in *2015 IEEE Radar Conference (RadarCon)*, 2015, pp. 1228-1233.
[81] F. Santi *et al.*, "Passive multi-perspective GNSS-based SAR using CLEAN technique: an experimental study," in *Proceedings of EUSAR 2016: 11th European Conference on Synthetic Aperture Radar*, 2016, pp. 1-4.
[82] I. Walterscheid and A. R. Brenner, "Multistatic and multi-aspect SAR data acquisition to improve image interpretation," in *2013 IEEE International Geoscience and Remote Sensing Symposium - IGARSS*, 2013, pp. 4194-4197.
[83] W. Wang *et al.*, "Multistatic SAR information fusion based on image registration and fake color synthesis," in *IGARSS 2018 - 2018 IEEE International Geoscience and Remote Sensing Symposium*, 2018, pp. 7275-7278.
[84] J. Ender, "The meaning of k-space for classical and advanced SAR-techniques," in *International Symposium on Physics in Signal and Image Processing (PSIP 2001)*, Marseille, France, 2001, vol. 2001, pp. 23-38.
[85] Z. Tao *et al.*, "Comparison between monostatic and bistatic SAR image based on spatial spectrum analysis," in *IET International Radar Conference 2015*, 2015, pp. 1-6.
[86] V. S. Chernyak, *Fundamentals of multisite radar systems*. London: Routledge, 1998.
[87] J. L. Garry *et al.*, "Practical implementation of stripmap Doppler imaging," *IET Radar, Sonar & Navigation,* vol. 9, no. 8, pp. 974-983, 2015.